MODERATE TEMPERATURE DETECTOR DEVELOPMENT

NASA CR-160306

(NASA-CR-160306) MODERATE TEMPERATURE DETECTOR DEVELOPMENT Final Report (Honeywell, Inc.) 142 p HC A07/MF A01 CSCL 14B

N79-30533

Unclas G3/35 31833

A.K. SOOD, J.W. MARCINIEC AND M.B. REINE

FINAL TECHNICAL REPORT

Contract NAS 9-15250

National Aeronautics and Space Administration
Lyndon B. Johnson Space Center
Houston, Texas 77058

August 1979

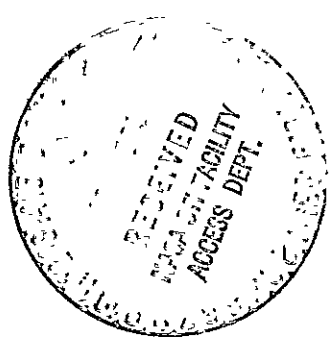

HONEYWELL
Defense Electronics Division
Electro-Optics Center
2 Forbes Road
Lexington, Massachusetts 02173

MODERATE TEMPERATURE DETECTOR DEVELOPMENT

by

A.K. SOOD, J.W. MARCINIEC AND M.B. REINE

FINAL TECHNICAL REPORT

Contract NAS 9-15250

National Aeronautics and Space Administration
Lyndon B. Johnson Space Center
Houston, Texas 77058

August 1979

HONEYWELL
Defense Electronics Division
Electro-Optics Center
2 Forbes Road
Lexington, Massachusetts 02173

TABLE OF CONTENTS

PRECEDING PAGE BLANK NOT FILMED

LIST OF ILLUSTRATIONS

LIST OF ILLUSTRATIONS (cont'd)

LIST OF ILLUSTRATIONS (cont'd)

LIST OF TABLES

FOREWORD AND ACKNOWLEDGMENTS

This is the final technical report on Contract NAS9-15250, entitled "Moderate Temperature Detector Development." The work reported herein was performed at the Honeywell Electro-Optics Center in Lexington, Massachusetts during the period from February, 1977 through October, 1978.

The NASA Technical Monitors for this program were Mr. J.E. Kessel and Mr. J.R. Woodfill.

The principal investigator for Honeywell was Dr. A.K. Sood and the Program Manager was Dr. M.B. Reine. Device processing was carried out by Charles L. Bryant and Robert Perras. Device characterization was assisted by Roland J. McDonald.

The authors acknowledge the technical contributions of Dr. T.J. Tredwell, Mr. S.P. Tobin, Mr. D.L Polla, and Dr. M. Lanir during the course of this program.

SECTION I
INTRODUCTION

1.1 BACKGROUND

Detection of infrared radiation in the 8 to 12-micrometer spectral band has found widespread application during the past two decades for a variety of space, military and industrial applications. The atmospheric transmission window at 8 to 12 micrometers combined with the occurrence at approximately 10 micrometers of the peak in the spectral power distribution for emission from a 300 K blackbody radiator, have made this band important for collection of thermal information about the earth from a satellite.

For satellite-based applications, the operating temperature of the detector is of critical importance. For multi-spectral sensors, the visible channels may be operated at ambient temperature and the channels in the 1.5 to 2.5-micrometer spectral region may be operated at 193 – 250 K. However, detectors for the 8 to 14-micrometer channel require cooling to 60–90 K. On the one hand, as the operating temperature is increased, the detector sensitivity decreases rapidly. On the other hand, severe size, power and weight constraints for space operation dictate as high an operating temperature as possible. Thus, development of infrared detectors which are capable of operating at elevated temperatures with adequate sensitivity has substantial payoff in terms of sensor weight, cost, and lifetime.

1.2 SUMMARY OF THE PREVIOUS PROGRAM

An earlier theoretical and analytical program was carried out to define the most promising technical approach for development of 8 to 12-micrometer infrared quantum detectors operating at elevated temperatures. In achieving this objective, three tasks were undertaken:

- Determine the theoretical limit to performance of both thermal and quantum detectors for 8 to 12-micrometer infrared detection.

- Identify candidate detector materials and determine material parameters.

- Determine the present status of both quantum and thermal detectors, isolate the parameters limiting performance, and assess the feasibility of achieving performance at the theoretical limit.

Details of this study have been presented in the final report for the NASA/JSC Phase I Program.[1] The fundamental conclusion reached in the analysis of signal and noise in quantum detectors was that the ultimate limit to detectivity in a quantum detector depended only on the wavelength, temperature, and material index of refraction n. This ultimate limit could be met only if radiative, rather than Auger, recombination was the dominant recombination process. Thus, in evaluating semiconductor material classes for fundamental potential to achieve the theoretical limit to D*, the following criteria should be used:

- Auger recombination should be weak or negligible relative to radiative recombination.

- If above requirement is satisfied, then the material should have the lowest possible index of refraction.

The best suited material based on these criteria is $Hg_{0.8}Cd_{0.2}Te$. For $Hg_{0.8}Cd_{0.2}Te$ Auger recombination is dominant in nondegenerate n-type and lightly doped p-type. In heavily doped p-type radiative recombination is dominant up to 190 K. Thus, p-type (Hg,Cd)Te appears to be the best candidate on a theoretical limit to D* for elevated temperature operation.

It was also determined that the best device design for (Hg,Cd)Te for elevated temperature operation is n^+ on p. The factors limiting the R_oA product are the p-side lifetime τ_e and L_e (minority carrier diffusion length) for a given base carrier concentration. Further improvement in R_oA could be realized by using the "electrically reflecting backside contact" which could be achieved by fabricating n^+–p–p^+ structures.

The n^+–p–p^+ configuration consists of a thin (less than 0.5 μm) ion implanted n^+–region on a p–layer which has a thickness on the order of or less than a minority-carrier diffusion length. On the opposite side of this p–layer is a thin ion implanted p^+–region which forms a p^+–p "high-low" junction. Nearly all absorption of the incident infrared radiation occurs within the p–layer. For wavelengths appreciably less than the cutoff wavelength, the absorption coefficient is above 1000 cm^{-1}. Hence, the p–region in n^+–p structure need not be thicker than roughly 10 micrometers to avsorb most of the radiation, as any additional thickness of the base region would contribute to noise current. So to maximize the A/N ratio for a detector, the p–region should be as thin as possible while still thick enough to absorb most of the radiation. Of course, if it is then thinner than a diffusion length, which it usually will be, the back contact is within "range" of the junction as a possible source of carriers to be extracted by the junction.

A p^+–p (or n^+–n) contact can be thought of as an electrical reflector of minority carriers. This is because there is a potential barrier to the flow of minority carriers at such a contact, and minority carriers hitting the barrier are "reflected." In contrast, a purely metallic contact, at which the quasi-fermi levels in the semiconductor come together, acts as a sink for minority carriers.

1.3 GOAL AND OBJECTIVES OF THIS PROGRAM

Based on the findings of the Phase I study of this program, the major goal of Phase II and III programs was the development of (Hg,Cd)Te detectors for 8 to 12–micrometer wavelength regions capable of achieving significantly improved sensitivity at non-cryogenic temperatures. The specific technical objectives of these two phases were:

PHASE II

- To develop an n^+–on–p (Hg,Cd)Te photodiode which will achieve improved R_oA products both at moderate (90 – 110 K) and at elevated (130 – 160 K) temperatures.

- To develop techniques for the fabrication of a reflecting back-side contact ($p–p^+$) structure to further reduce overall device noise sources at higher temperatures in the n^+–on–p device.

- To fabricate and test a ten (10) element linear array utilizing the n^+–on–p structure modified to include the reflecting backside contact. As a design goal, this array will have a D^*_λ equal to 8.0×10^9 cm $Hz^{1/2}/W$ at 11–micrometers and at a temperature of 120 K.

PHASE III

- Develop the technology for fabricating $n^+–p–p^+$ photodiodes with reflecting backside contacts with medium doped p–type $Hg_{0.8}Cd_{0.2}Te$ with hole concentration of 2.0×10^{16} cm^{-3}.

- Study and evaluate the effect of p–type material hole concentrations for enhancing sensitivity at elevated temperature using medium doped p–type $Hg_{0.8}Cd_{0.2}Te$ with hole concentration greater than 1×10^{17} cm^{-3}.

- Develop an improved device by reducing the volume of the semiconductor to utilize only the volume collecting signal (thin device of 10 to 20–micrometer thickness).

- Based on the developed techniques of above, fabricate and characterize detector for D*, R_oA product, quantum efficiency and noise versus frequency, and cutoff wavelength. The characterization shall be versus temperature for each of the detector parameters listed over the range of 77 K to 170 K or higher.

- Design Goals:

Temperature Operation	145 K
Detector Area	$0.01 \times 0.01\ cm^2$
R_oA	$2.0 \times 10^{-2}\ \Omega - cm^2$
Cutoff Wavelength	11 μm
D* (11 μm, 3 kHz)	$8.0 \times 10^9\ cm\ Hz^{1/2}/W$
Number of Elements	Single Element Detector (mounted in a Dewar)

Details of the devices delivered to NASA/JSC fabricated under Phase II and Phase III are given in Appendixes A and B respectively.

1.4 SUMMARY OF THE RESULTS OF THIS PROGRAM

Following are the accomplishments for Phases II and III of this Program:

PHASE II

- Development of the junction fabrication technology which gave rise to n^+–p junction photodiodes active up to 193 K.

- Demonstration of the diffusion limited performance in n^+–p junction photodiodes for temperature range of 90 to 145 K.

- Measurement of minority carrier lifetimes in p–type $Hg_{0.8}Cd_{0.2}Te$ from which it was concluded that the electron lifetime in p–$Hg_{0.8}Cd_{0.2}Te$ was limited by midgap Shockley-Read type centers.

- Fabrication and delivery of a ten-element array to NASA/JSC, which met the Phase I design goals for an operation at 120 K.

PHASE III

- Development of the ion-implantation technology using phosphorus and arsenic for fabrication of p^+ layers in p-$(Hg_{0.8}Cd_{0.2})Te$.

- Evaluation of the p^+-layer in p-$Hg_{0.8}Cd_{0.2}Te$ using Hall Vander Pauw technique.

- Fabrication and evaluation of n^+-p-p^+ diode structure via tapered array structure.

- Fabrication and delivery of an n^+-p-p^+ array to NASA/JSC using the technology developed in this program.

SECTION 2
ANALYSIS OF THE n^+–p–p^+ $Hg_{0.8}Cd_{0.2}Te$ JUNCTION PHOTODIODE

2.1 BACKGROUND

The performance of an infrared detector is most commonly characterized by its detectivity D^*_λ. Detectivity can be expressed in terms of other detector parameters as follows:

$$D^* = \frac{R_{\lambda i}\sqrt{A\Delta f}}{I_N} \qquad (1)$$

where $R_{\lambda i}$ = current responsivity
A = optically active area
Δf = noise bandwidth
I_N = rms noise current measured in the bandwidth Δf

The current responsivity $R_{\lambda i}$ (in A/W) for a photodiode can be written as:

$$R_{\lambda i} = \frac{\lambda}{hc}\,\eta e \qquad (2)$$

where h is Planck's constant, c is the speed of light, e is the electron charge, and is the quantum efficiency.

The quantum efficiency is defined as the ratio of the number of photogenerated electrons flowing across the junction to the number of photons (with photon energy greater than the bandgap energy) incident on the photodiode active area. Quantum efficiencies in excess of 50% are common for (Hg,Cd)Te junction photodiodes.

The rms noise current I_N in a noise equivalent bandwidth Δf for a photodiode is given by[1,2]

$$\frac{I_N^2}{\Delta f} = 4kT\,\mathrm{Re}(Y) - 2e|I| \qquad (3)$$

where Re(Y) is the real part of the diode admittance Y (over the frequency range of interest) and I is the total direct current at the diode terminals (positive for forward bias and negative for reverse bias). Both Re(Y) and I are in general functions of the applied bias voltage V. Also, Re(Y) is in general a function of frequency; over the frequency range usually used for direct (i.e., non-heterodyne) detection, this frequency dependence is negligible and Re(Y) is given by

$$\mathrm{Re}(Y) = \frac{dI}{dV} \equiv \frac{I}{R(V)} \qquad (4)$$

where I = I(V) is the total direct current through the diode.

There are several well-known mechanisms which can contribute to the total direct current I(V) through the diode:

$$I(V) = (J_d + J_{gr} + J_t)A + I_L - I_Q \qquad (5)$$

The first three terms represent diffusion current, depletion-layer generation-recombination current and interband tunneling current. Each of these three currents is written as the product of a current density (in A/cm^2) times the junction area A to emphasize the "bulk" nature of these three mechanisms. When the dimensions of the junction area A are on the order of (or smaller than) a minority carrier diffusion length, this assumption needs to be examined carefully.

The fourth term in Equation 5 represents what is commonly referred to as diode "leakage" or "shunt" current. The origin of this current is usually at the region where the junction intersects the surface. More will be said about this later.

The fifth term in Equation 5 represents photocurrent. For the simplest case of a uniform photon flux Q fully illuminating the junction area A, the photocurrent I_Q is given by:

$$I_Q = \eta e Q A \tag{6}$$

where η is the junction quantum efficiency.

An important special case of Equation 3 is for zero-bias voltage. For V=0, all currents in equation 5 are zero except the photocurrent I_Q. The noise at V=0 is then given by:[3]

$$\frac{I_N^2}{\Delta f} = \frac{4kT}{R_o} + 2\eta e^2 Q A \tag{7}$$

In order for the photodiode to operate as a background-limited infrared photodetector (BLIP), one must have the background noise much larger than the diode thermal noise. From Equation 7, one obtains the following inequality which must be satisfied for the photodiode to be BLIP:

$$R_o A \gg \frac{2kT}{\eta e^2 Q} \tag{8}$$

This inequality is one of the reasons why the R_oA-product has become a common figure-of-merit for infrared photodiodes. One wants an R_oA large enough so that Equation 8 is satisfied.

Substitution of Equations 2 and 7 into Equation 1 yields the following expression for the detectivity of a photodiode at zero-bias voltage:

$$D^*_\lambda = \frac{\lambda}{hc}\,\eta_e \frac{1}{\sqrt{\frac{4kT}{R_oA} + 2\eta e^2 Q}} \tag{9}$$

If the inequality of Equation 8 is satisfied, then the photodiode is background-limited with the following detectivity:

$$D^*_\lambda = \frac{\lambda}{hc}\sqrt{\frac{\eta}{2Q}} \tag{10}$$

If, on the other hand, the R_oA product is so low that the thermal noise is dominant, the detectivity at zero-bias voltage is given by:

$$D^*_\lambda = \frac{\lambda}{2hc}\,\eta e\sqrt{\frac{R_oA}{kT}} \tag{11}$$

The only properties of the photodiode which appear here are its quantum efficiency and R_oA product.

It is common to use the R_oA product as the primary figure-of-merit for an infrared photodiode. Clearly one wants as large an R_oA product as possible at a given temperature.

One can relate the R_oA product of a photodiode to its current-voltage characteristics by means of Equations 4 and 5:

$$\frac{1}{R(V)} = A\frac{d}{dV}\left[J_d(V) + J_{gr}(V) + J_t(V)\right] + \frac{dI_L}{dV} \tag{12}$$

In particular, the R_oA product (i.e., at zero-bias voltage) is given by:

$$\frac{1}{R_oA} = \frac{d}{dV}\left[J_d(V) + J_{gr}(V) + J_t(V)\right]\Big|_{V=0} + \frac{1}{A}\frac{dI_L}{dV}\Big|_{V=0} \tag{13}$$

This says that the R_oA product at zero-bias voltage is determined in principle by several junction current mechanisms. In practice, usually one of these mechanisms will be much larger than the others over certain ranges of temperature and for certain junction geometries and doping levels.

In this program, the emphasis is on 8 to 12-micrometer photodiodes operating at high temperatures (120 – 180 K). At these temperatures, thermally generated diffusion current is the most important junction current mechanism. Thermal generation and recombination occurs in both the n^+ and p regions of the n^+–p junction, and so diffusion current can originate from either side.

The relationship between current density and voltage for a diode through which only diffusion current flows is given by the familiar Shockley equation:[4]

$$J_d(V) = J_{sat} \left[\exp\left(\frac{eV}{kT}\right) - 1\right] \qquad (14)$$

where J_{sat}, referred to as saturation current density, is independent of voltage.

In the following sections, we consider diffusion current in the n^+–p–p^+ junction configuration shown in Figure 2–1. J_{sat} in Equation 14 can be written as

$$J_{sat} = J_{sat,\,n} + J_{sat,\,p} \qquad (15)$$

where the two terms on the right hand side represent diffusion current originating from the n–side and the p–side.

2.2 DIFFUSION CURRENT FROM THE p–SIDE

If the p–region shown in Figure 2–1 were infinitely thick (i.e., if $d \gg L_e$, where L_e is the minority carrier diffusion length in the p–region), then the diffusion current density would be simply[3]

$$J_{sat,\,p\infty} = \frac{e\, n_{po}\, D_e}{L_e} \qquad (16)$$

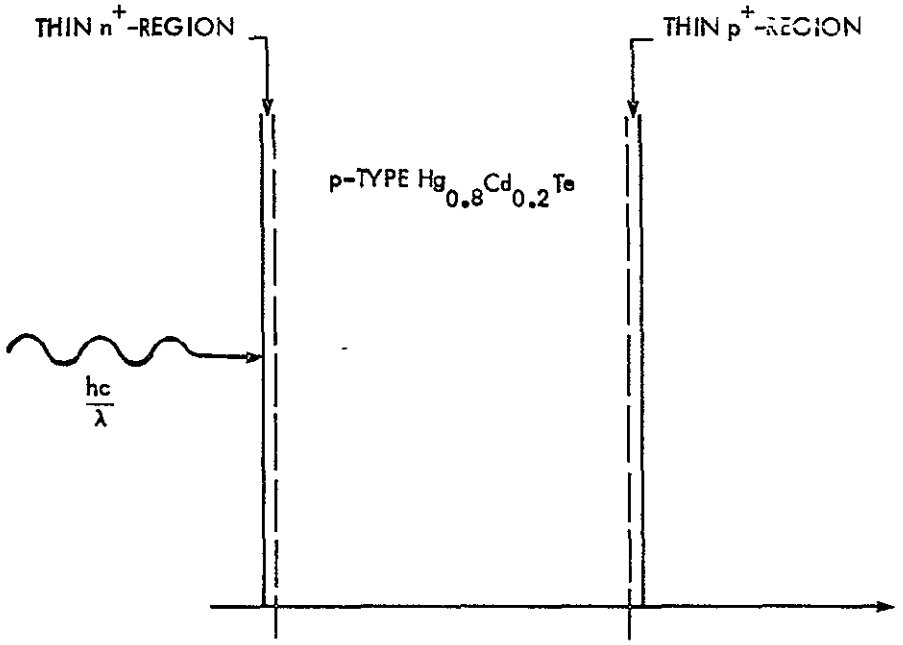

Figure 2-1 The n^+–p–p^+ Junction Configuration

If diffusion current from the n-side were negligible, then Equations 13 and 14 would give for the R_oA product

$$(R_oA)_\infty = \frac{kT}{e^2} \frac{L_e}{n_{po} D_e} \tag{17}$$

In the above equations, n_{po} is the thermal equilibrium minority carrier concentration on the p-side, and D_e is the minority carrier diffusion coefficient. L_e is related to D_e and to the minority carrier lifetime τ_e:

$$L_e^2 = D_e \tau_e \tag{18}$$

Now if the p-region thickness d is on the order of L_e, then the boundary condition at z = d is important in determining $J_{sat,\ p}$. If the p–p^+ boundary is "electrically reflecting" or "blocking," then, as Long points out, the saturation current density becomes

$$J_{sat,\ p} = J_{sat,\ p\infty} \tanh\left(\frac{d}{L_e}\right) \tag{19}$$

and the R_oA product is

$$R_oA = (R_oA)_\infty \coth\left(\frac{d}{L_e}\right) \tag{20}$$

Since, for small values of y,

$$\tanh(y) \longrightarrow y$$

$$\coth(y) \longrightarrow \frac{1}{y}$$

one can see that making d less than L_e leads to a reduction in saturation current and an increase in R_oA product, providing the p-region has an "electrically-reflecting" or "blocking" boundary at z = d.

On the other hand, if there is an ohmic contact to the p-region at z = d, the saturation current and R_oA product are given by

$$J_{sat,\,p} = J_{sat,\,p\infty} \coth\left(\frac{d}{L_e}\right) \tag{21}$$

$$R_oA = (R_oA)_\infty \tanh\left(\frac{d}{L_e}\right) \tag{22}$$

Here the saturation current density increases and the R_oA product decreases when d becomes less than L_e.

The behavior of the R_oA product as a function of p-region thickness d is shown in Figure 2-2 for both the "electronically reflecting" boundary (Equation 20) and the ohmic boundary (Equation 22).

For the electrically reflecting boundary, when $d \ll L_e$, the limiting form for R_oA obtained from Equations 17 and 20 is

$$R_oA = \frac{kT}{e^2} \frac{\tau_e}{n_{po}\, d} \tag{23}$$

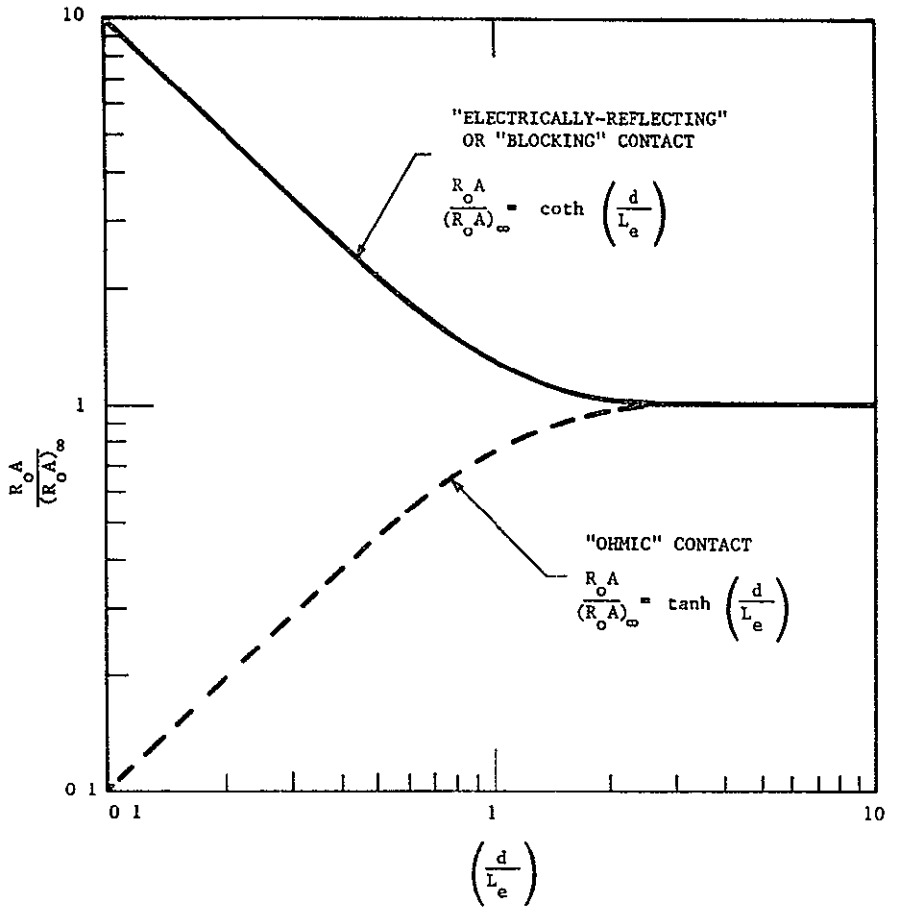

Figure 2-2 Effect of Reducing the Thickness of the p-region thickness d on the R_oA Product Resulting from Diffusion Current from the p-side.

2.3 AUGER LIFETIME IN p-TYPE $Hg_{0.8}Cd_{0.2}Te$

The electron-electron Auger lifetime in p-type $Hg_{0.8}Cd_{0.2}Te$ has been discussed in Section 3.2.2 of Reference 1. For low to moderate acceptor doping concentrations, the Auger lifetime τ_A for electron-electron collisions is

$$\tau_A = 2\,\tau_{Ai} \tag{24}$$

where τ_{Ai} is the Auger lifetime in intrinsic $Hg_{0.8}Cd_{0.2}Te$. From Equation (620.2) of Reference 5, the intrinsic Auger lifetime in seconds is

$$\tau_{Ai} = 3.8 \times 10^{-18} \frac{\varepsilon_\infty^2 \sqrt{1+\mu}\,(1+2\mu)}{m_c |F_1 F_2|^2} \left(\frac{E_g}{kT}\right)^{3/2} \exp\left[\left(\frac{1+2\mu}{1+\mu}\right)\frac{E_g}{kT}\right] \quad (25)$$

where ε_∞ is the high frequency dielectric constant, m_c is the conduction band effective mass ratio, E_g is the energy gap, and μ is the effective mass ratio:

$$\mu = \frac{m_c}{m_v} \quad (26)$$

where m_v is the valence band effective mass ratio. The quantity $|F_1 F_2|^2$ is the product of two overlap integrals of the periodic parts of Block wave functions.

In Figure 2–3 we show the calculated Auger lifetime p–type $Hg_{1-x}Cd_xTe$, of low to moderate acceptor doping, for a constant cutoff wavelength of 12 micrometers over the 77 – 200 K temperature range. The curve was calculated from Equations 24 and 25. In the calculation, the high frequency dielectric constant ε_∞ was taken as 12.8 and the heavy-hole valence band effective mass ratio was taken as 0.4. The conduction band effective mass ratio m_c was computed from Kane's relationship

$$\frac{1}{m_c} = \frac{1}{3} E_p \left[\frac{2}{E_g} + \frac{1}{E_g + \Delta}\right] \quad (27)$$

where E_p was taken as 17.9 eV and the energy separation Δ of the split-off valence band was taken as 1 eV. For a cutoff wavelength of 12 micrometers, the energy gap E_g is 0.103 eV, and Equation 27 gives a value of about 0.008 for m_c.

A value for $|F_1 F_2|^2$ was obtained by fitting Equations 25 and 27 to the data of Kinch, Brau and Simmons[3] for the Auger lifetime in n–type $Hg_{0.8}Cd_{0.2}Te$ photoconductors. Setting $|F_1 F_2|^2 = 0.06$ make Equations 25 and 27 agree well with the data in Figures 11 and 12 of Reference 6 over the 143 – 200 degree temperature range, over which the lifetime measured was the intrinsic Auger lifetime. This value of 0.06 for $|F_1 F_2|^2$ was used in calculating the curve in Figure 2–3.

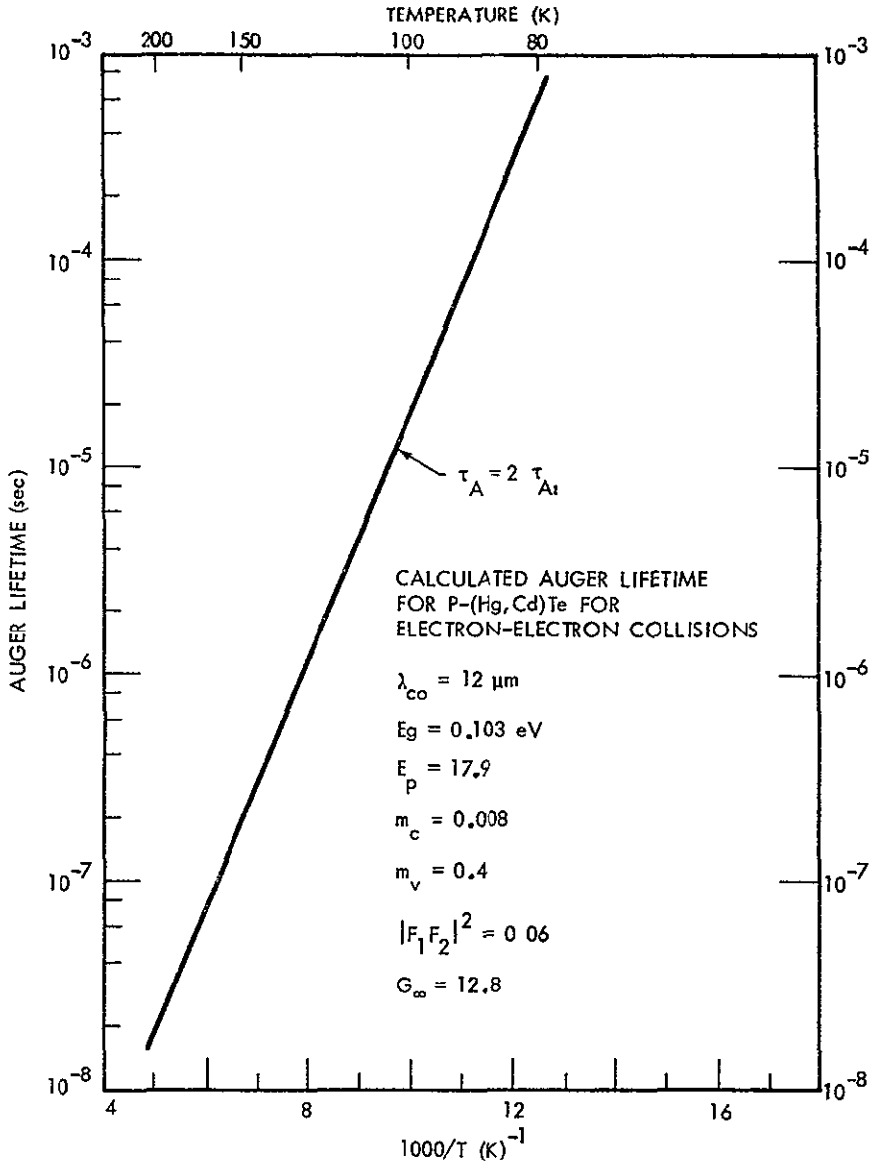

Figure 2-3 The Electron-Electron Auger Lifetime

2.4 RADIATIVE LIFETIME IN p-$Hg_{0.8}Cd_{0.2}Te$

Band to band radiative recombination process involves the recombination of an electron-hole pair by emission of a photon with approximately the gap energy, Eg. If the transition is between band extrema located at the source point in k-space, then the transition is direct radiative recombination and involves photon emission only. Indirect

radiative recombination occurs only when the band extrema are at different k's and phonon emission must occur to conserve energy. The problem of radiative recombination has been treated in general by Van Roosbroeck and Shockley[7] and its application to n-type $Hg_{0.8}Cd_{0.2}Te$ has been carried out by Kinch et. al.

In applying the analysis of Kinch, et. al.,[6] to p-$(Hg_{0.8}Cd_{0.2})Te$ and considering small departures from equilibrium, radiative lifetime can be written as

$$\tau_{rad} = \left[B\,(n_o + p_o + \Delta n)\right]^{-1} \tag{28}$$

where

$$B = \frac{8\pi\,\varepsilon_\infty}{n_i^2\,h^2\,c^2} \int_o^\infty \frac{(h\nu)\,h^2\,\nu^2\,d(h\nu)}{\exp(h\nu/kT) - 1} \tag{29}$$

Expression (28) can be further simplified for small departures from thermal equilibrium in case of p-$Hg_{0.8}Cd_{0.2}Te$, for $(n_o + p_o) \gg n$, we have

$$\tau_{rad} = \frac{1}{B(n_o + p_o)} \tag{30}$$

The coefficient B has been evaluated by Hall[8] for simple parabolic bands:

$$B = 5.8 \times 10^{-13}\sqrt{\varepsilon_\infty}\left(\frac{1}{m_c + m_r}\right)^{3/2}\left(1 + \frac{1}{m_\nu}\,\frac{1}{m_c}\right)\left(\frac{300}{T}\right)^{3/2} \cdot E_g^2 \tag{31}$$

Radiative lifetimes for p-$Hg_{0.8}Cd_{0.2}Te$ for a series of carrier concentrations ranging between $1.0 \times 10^{16} - 2.0 \times 10^{17}\ cm^{-3}$ have been calculated and the results are presented in Figure 2-4.

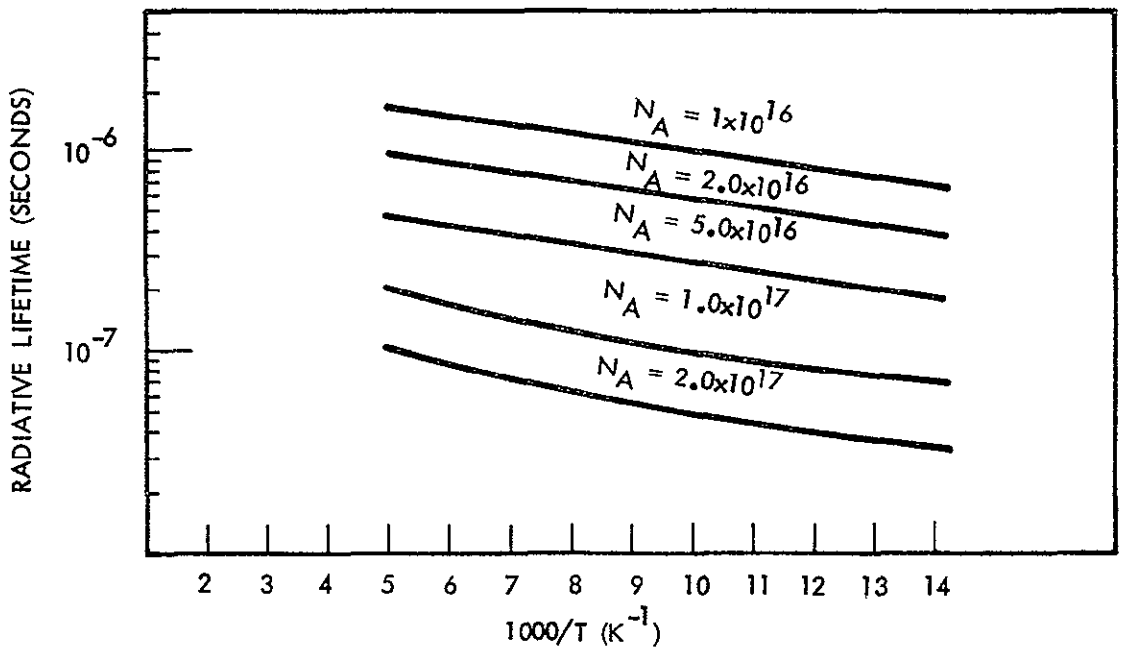

Figure 2-4 Radiative Lifetime in p-$Hg_{0.8}Cd_{0.2}Te$ as a Function of Various Acceptor Concentrations between 70 and 200 K

SECTION 3
JUNCTION DEVELOPMENT IN p-$Hg_{0.8}Cd_{0.2}Te$

In a theoretical study of Detection of Long Wavelength Infrared Radiation at Moderate Temperatures[1], it was determined that (Hg,Cd)Te offers the best possible material choice from basic considerations. It was also determined that the best device design for (Hg,Cd)Te for elevated temperature operation is n^+ on p. The factor limiting R_oA is the p-side electron lifetime τ_e among other parameters. For minority carrier lifetimes limiting radiative recombination and minority carrier diffusion lengths in excess of 50 micrometers further improvement in performance at high temperatures can be made using the electrically reflecting contact (n^+-p-p^+).

This concept has been discussed in detail in the NASA/JSC Phase I study[1] and elsewhere.[2,3] In this section we will discuss the fabrication of n^+ and p^+ regions in p-$Hg_{0.8}Cd_{0.2}Te$ via ion-implantation techniques.

3.1 n^+ IMPLANT DEVELOPMENT

3.1.1 Fabrication of n^+ Layer Using Ion Implantation

The n^+ layers on $Hg_{0.8}Cd_{0.2}Te$ were fabricated using ion implantation techniques. Ion implantation offers an added advantage over diffusion of impurities for fabrication of n^+ layer; namely the amount of impurity and its depth can be precisely controlled. The wafer does not see any high temperature processing except the moderate temperature treatment required for eliminating damage induced in lattice during ion implantation.

In the course of junction fabrication, boron, chlorine and silicon were used as implant species for n^+layer. These impurities were selected based on work carried out on diffusion of impurities in $Hg_{0.6}Cd_{0.4}Te$.[9,10]

These conclusions can be summarized as follows:

- The electrical activity of impurities is as expected from the substitution of various groups on the respective metal and Te sublattices. Impurities substituted on the metal sublattice are generally rapid diffusers while those on Te sublattice are quite slow. For the metal sublattice, the donor impurities appear to diffuse more slowly than the acceptors.

- Cu, Ag, Au and Li comprise the fast diffusing acceptors; Ga and In are fast diffusing donors.

- Al and Si are donors; high temperatures are necessary to affect diffusion.

- Sn and Pb are inactive when diffused at temperatures $\sim 300^{o}C$. Pb makes ohmic contacts to n- and p-type $Hg_{0.6}Cd_{0.4}Te$.

- P, As and Sb are slowly diffusing acceptors; Br and I are slowly diffusing donors.

- Cr is either a slowly diffusing donor or inactive.

- Ni is inactive and makes ohmic contacts to p-type $Hg_{0.8}Cd_{0.2}Te$.

Based on this work, various impurities were selected for fabricating n^{+} layer. Silicon was selected as an implant species, as it has been shown to be a slow diffusing donor. Chlorine was selected on the criterion that bromine and iodine are both slow diffusing donors. However, bromine and iodine are heavier than chlorine, and implantation of these species would create a large damage in p-$Hg_{0.8}Cd_{0.2}Te$ lattice. Chlorine being in the same column would also act as a donor impurity, but being a lighter element than bromine or iodine, would not leave as much damage.

Boron being an extremely light element should give rise to a minimal amount of damage. This impurity was selected on that criterion. However, no data was available on its behavior and diffusion coefficient in $Hg_{0.8}Cd_{0.2}Te$.

Implant depth and their profiles were calculated for each element in p–$Hg_{0.8}Cd_{0.2}Te$. Since ZnS layer was sputtered prior to ion-implantation, the depth profiles of boron in ZnS were also calculated. A model similar to that outlined by Verbracken and his coworkers[11] was used to calculate implantation profiles for ZnS/$Hg_{0.8}Cd_{0.2}Te$ system. Details of these calculations have been presented elsewhere.[12,13]

Junctions in p–$Hg_{0.8}Cd_{0.2}Te$ were fabricated using boron species with a series of accelerating voltages. For the most part accelerating voltages for boron implantation were kept between 40 to 100 KeV and the implant dose used was varied between 1×10^{14} to 1×10^{15} ions/cm^2 by adjusting the beam current.[12]

3.1.2 Post-Implant Damage Anneal

As discussed in the last section, boron, chlorine and silicon ions were used for fabricating n^+ layers in p–$Hg_{0.8}Cd_{0.2}Te$. Junction depth and profile was adjusted by controlling beam current and accelerating voltage of the ion beam. When ions with high energy are bombarded on the lattice, a considerable amount of damage is induced in the lattice of p–$Hg_{0.8}Cd_{0.2}Te$. This excess damage will mask activity of the implanted species.

In order to eliminate damage induced in the lattice due to ion implantations, post implant anneals were carried out to anneal out residual damage, thereby minimizing any masking effects due to this lattice damage.

Post-implant anneals were carried out in reducing atmosphere of forming gas in a clean quartz tube furnace. Temperatures for post-implant anneal were varied between 125 and 300°C and time was varied between 1/2 to 3 hours. It was determined that best results of implant activation were obtained for temperatures between 140 to 175°C and anneal times between 1 to 3 hours. Anneal schedules were varied from run to run depending on dosage of the implant.[12]

Results obtained on activation of boron, chlorine and silicon can be summarized as follows:

a) Silicon implantation in p-$Hg_{0.8}Cd_{0.2}Te$ wafers did not show any activation for various post-implant anneal time temperature schedules. During these annealing schedules, temperature was varied from 125 to 300°C and time was varied from 1/2 to 3 hours.

Similarly p-type wafers with various hole concentrations in range of 2.0×10^{16} to 1.0×10^{17} cm^{-3} were used for implanting silicon ions to examine the effects of carrier concentration of p-type wafer on activation of implanted species for a given dose (greater than hole concentration). Results showed that no activation was observed for any sample in this range of carrier concentration.

Our experiments showed that silicon which acts as a donor-like species in $Hg_{0.6}Cd_{0.4}Te$ does not show any activation (donor-like behavior) in p-$Hg_{0.8}Cd_{0.2}Te$. It is quite conceivable that damage induced in lattice during implantation may be masking activation due to implanted silicon ions; however, after carrying out post-implant anneals, it should be possible to observe some conversion to n-type. In all the wafers examined, no sample showed conversion to n-type for the range of carrier concentration discussed.

b) Chlorine implantation of p-$Hg_{0.8}Cd_{0.2}Te$ was also carried out for wafers with hole concentration in the range of 2×10^{16} to 1.0×10^{17} cm^{-3}. Junction depths were varied from 0.5 to 1.0 micrometer by adjusting the beam energy. Results showed that chlorine formed n^+ layer only on wafers with carrier concentrations below 5.0×10^{16} cm^{-3}. Wafers with hole concentration in excess of 5.0×10^{16} cm^{-3}, did not show adequate conversion to n-type. During the course of this program, photodiodes were fabricated with chlorine implantation and results will be presented in the next section.

c) Boron implantation was found to yield uniform surface conversion to n-type. Fabrication of n^+ layers was also carried out on wafers with hole concentrating ranging from 2.0×10^{16} to 1.0×10^{17}. Activation of boron was found to be excellent. In this program, photodiodes were fabricated with junction depths varying from 0.5 to 1.0 micrometers. Ion dose was adjusted such that after post implant anneals, donor concentrations of 1.0×10^{18} cm^{-3} was obtained.

3.2 n^+–p JUNCTION THICK DIODE FABRICATION

Fabrication of n^+–p junction photodiodes was carried out by implanting a donor type species to form n^+ layers in p–$Hg_{0.8}Cd_{0.2}Te$ wafers. As discussed in the earlier section, boron and chlorine ions were found to be quite suitable for junction fabrication. Most of the results reported in this report on n^+–p junction photodiodes were obtained by boron ion-implantation. The overall processing for n^+–on p photodiodes has been subdivided into three categories, namely:

- Processing steps
- Ion-implantation
- Post-implant anneals

3.2.1 Processing Steps

$Hg_{0.8}Cd_{0.2}Te$ wafers cut from the crystal with a wire saw were then mechanically tapped and polished to remove all the saw damage. The wafer was then mechanically polished until a mirror-like finish was obtained, after which a chemical polish was given by etching a few micrometers of material to eliminate any traces of leftover damage during mechanical polishing. It is extremely critical to remove all the saw damage or any other stresses induced during the surface preparation. Failure to do so can result in propagation of this damage deeper into bulk upon various heat treatments carried out during device fabrication. The wafer was thoroughly washed to remove any chemical residues on the surface and a passivation layer was sputtered to protect the surface.

After (Hg,Cd)Te surface was passivated, junction areas were defined by photolithography and the rest of the area was covered with a thick photoresist. Ion implantation of desired species was carried out, details of which are given in the next section. The wafers were then subjected to post-implant anneals. It was determined that the post-implant anneal temperature and time play a very crucial role in determining the activity of the implanted species. As activation is masked by the damage created in the lattice during ion implantation, schematics of various processing steps carried out for photodiodes are shown in Figure 3-1.

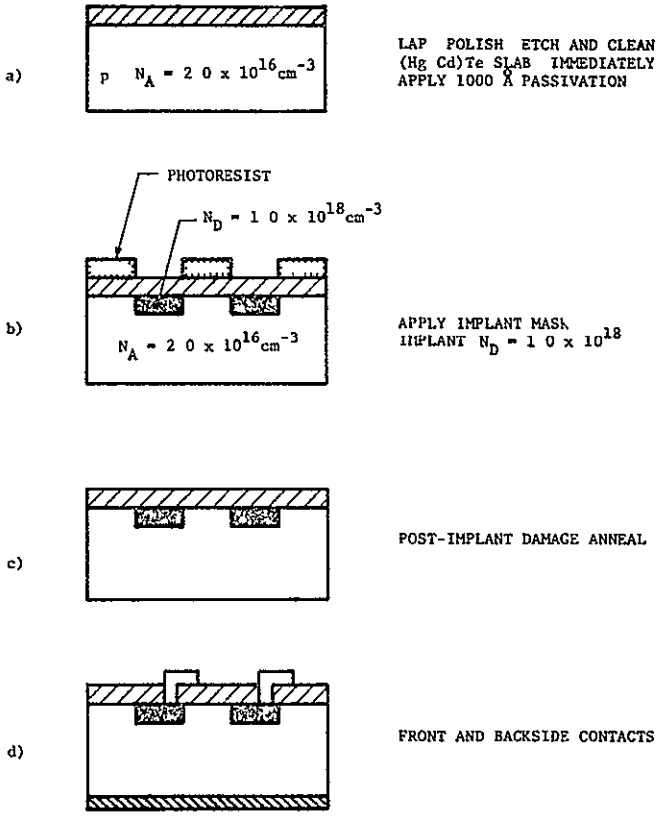

Figure 3-1 Schematics of Ion-Implanted n^+-on-p (Hg,Cd)Te Photodiodes

Front and back side contacts were fabricated subsequent to post-implant anneals. Contact areas were defined by photolithography and evaporated indium was used for front side contact. Both on-area and off-area bonds were used for front side contact. Back side contacts were made with a thin layer of gold. Other metals such as copper and nickel were investigated for p-side contact. Devices were then diced from the wafer and mounted in a 40-pin flat pack.

3.3 ARRAY CHARACTERIZATION

Detailed characterizations of the n^+–p junction photodiode arrays, fabricated using the double boron implantation process[12] during the phase II program, were carried out using the following measurement techniques;

- Current-voltage characteristics
- Spectral response measurements
- Zero bias impedance measurements
- Quantum efficiency
- Detectivity
- Measurement of minority carrier lifetimes.

In addition to above measurements, detailed characterization of the current limiting mechanism in these devices between 77 and 200 K was also carried out and finally a comparison was made between the measured detector performance with theoretical calculations based on a model for diffusion limited device performance.

3.3.1 Current-Voltage Characteristics

Figure [illegible] current-voltage characteristics of a n^+-p [illegible] devices from [illegible] diffusion [illegible] the device performance dominated by [illegible] breakdown mechanism. Similarly, Figure 3–3 shows the current-voltage characteristics for an element in the array 20574/SSI–CA, demonstrating that at high temperatures (i.e., 145 and 193 K), the diode shows diffusion limited performance and at 80 K the performance shows deviations from the diffusion current limits and is being dominated by some leakage mechanism. During the course of this program, arrays were also fabricated where the typical performance was similar to that shown in Figure 3–4. This detector element clearly shows the reverse and zero bias characteristics to be bulk diffusion current limited.

ORIGINAL PAGE IS
OF POOR QUALITY

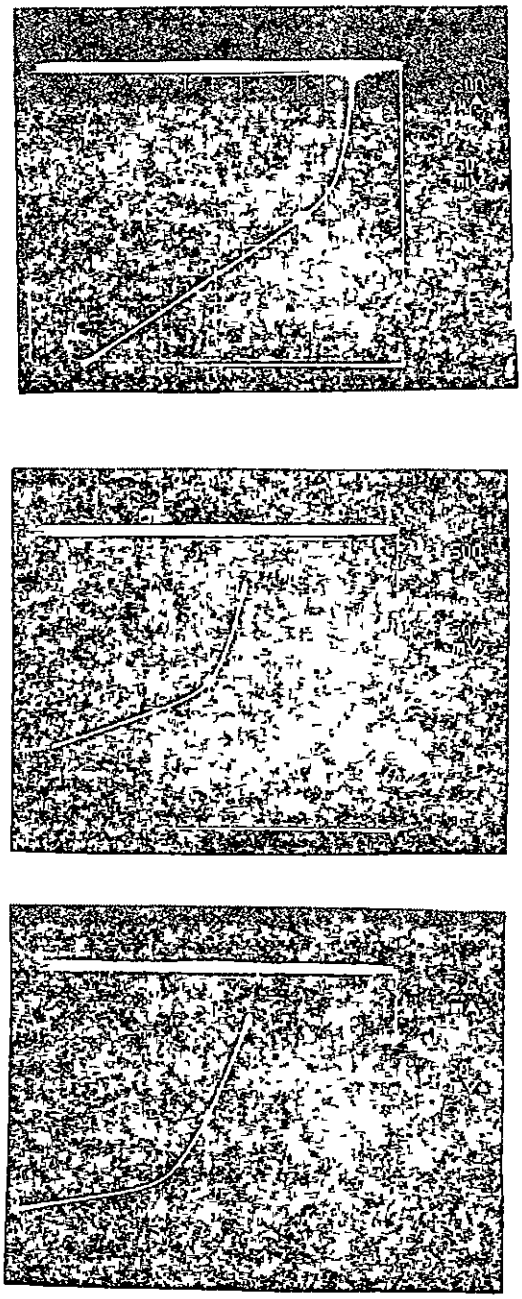

Figure 3-2 Current-Voltage Characteristics for a Detector Element (#5) on a n^+–p Junction Photodiode Array at 80, 145 and 195 K. This device is Active up to 195 K. However, the Reverse Bias Characteristics Show a Large Leakage Current and Deviation from the Diffusion Limited Performance even at High Temperatures.

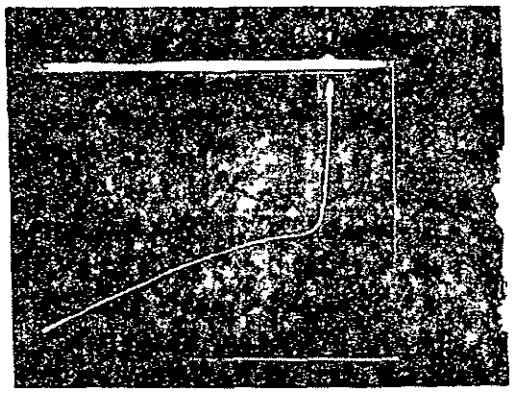

DEVICE NO
20574/S51-Ca/ELEMENT NO 3
T = 80K, $R_o = 2.5X10^4$ OHMS
$A_j = 10X10$ MIL^2 $A_{opt} = 1.09X10^{-3}$ cm^2
$R_oA_{opt} = 27.2\ \Omega$-cm^2
λ_{co} | 80K = 9.75 µm
$\eta = 0.70$

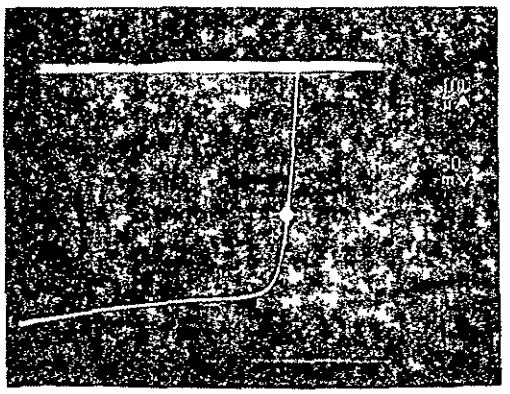

$R_o = 69\ \Omega$
$R_oA_{opt} = 7.5X10^{-2}\ \Omega$-cm^2
T = 145K
λ_{co} | 145K = 8.7 µm

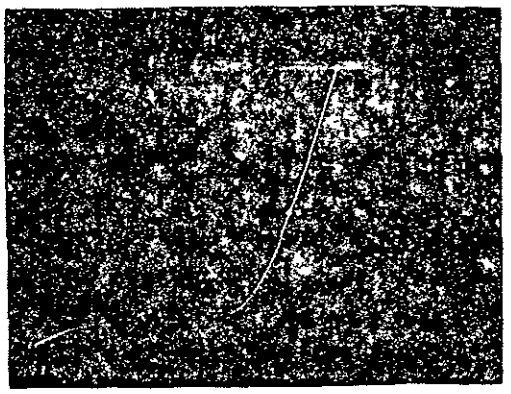

T = 193K
λ_{co} | 193K = 8.0 µm

ORIGINAL PAGE IS
OF POOR QUALITY

Figure 3-3 Current-Voltage Characteristics for a n^+–p Junction Photodiode Array (20574/S51-Ca/Element #3) at 80, 145 and 193 K. Similar to the Device Shown in Figure 3-2, this Device is active up to 195 K, and the Reverse Characteristics Show Diffusion Limited Performance at Small Reverse Bias Voltages.

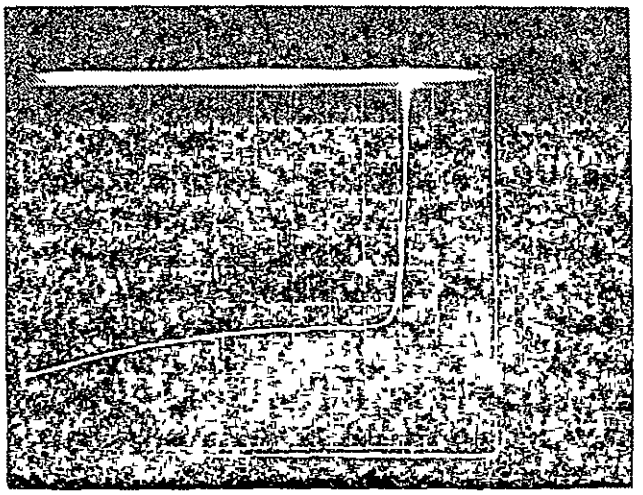

DEVICE NO
20574/S51/
ELEMENT # 21
T 80K
R_oA_J - 30 Ω-cm^2
λ_{co} | 80K 9 32 μm
BORON-DOUBLE IMPLANT
η = 80%

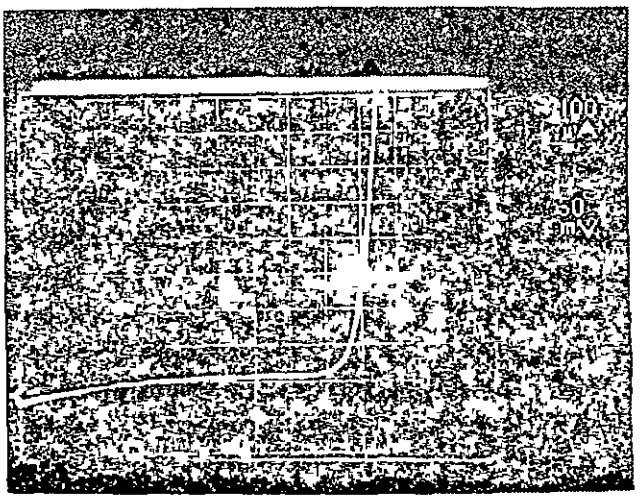

T - 145K
λ_{co} | 145K = 8.4 μm
R_oA_J 145K = 0 1Ω-cm^2

Figure 3-4 Current-Voltage Characteristics for a Detector Array (20574/S51/Element #21) Demonstrative Diffusion Limited Performance at 80 and 145 K.

For the most part, it was observed that these diodes were bulk diffusion limited for temperatures above 100 K (see Appendix A). Determination of the active area of these photodiodes was carried out by spot scan measurements. Figure 3–5 presents the spot scan measurements on a detector element (junction area = 5 x 5 mil^2) at 80, 145 and 193 K. This data clearly demonstrates that these photodiodes are active up to 195 K. Similarly, Figures 3–6 shows a spot scan measurement on an element of a detector array with junction area of 10 x 10 mil^2 at 80 K. Decrease in activity in the central region of the scan is due to the shadowing caused by the on-area bond wire. This scan shows that the charge collection region is greater than 10 x 10 mil^2 and the additional collection is from a diffusion length around the junction periphery.

3.3.2 Spectral Response Measurements

Measurement of the spectral response as a function of temperature was carried out on most of the arrays fabricated during this program. Typical measurements were done at 80, 145 and 193 K. This data for a n^+–p junction photodiode is presented in Figures 3–7 through 3–9. Measured shift in the 50% cutoff point of the spectral response as a function of temperature were in agreement with those predicited theoretically.[14] As an illustration, the spectral response curves presented in Figures 3–7 through 3–9 show that the cutoff wavelength in $(Hg_{0.8}Cd_{0.2})Te$ shifts by a micron when the device is cooled from 145 K down to 77 K.

3.3.3 Measurements of R_oA as a Function of Temperature

Zero bias impedance (R_o) was measured as a function of temperature on a series of photodiodes to determine the dominant current mechanism. It was observed that R_oA in these photodiodes, for temperatures greater than 100 K, was dominated by the diffusion current limited mechanisms. Detailed measurements of R_oA as a function of temperature on an array delivered to NASA/JSC was carried out and the results are presented in the Appendix A. Measured values of R_oA on the delivered array are also shown in Table 3–1 at three different temperatures.

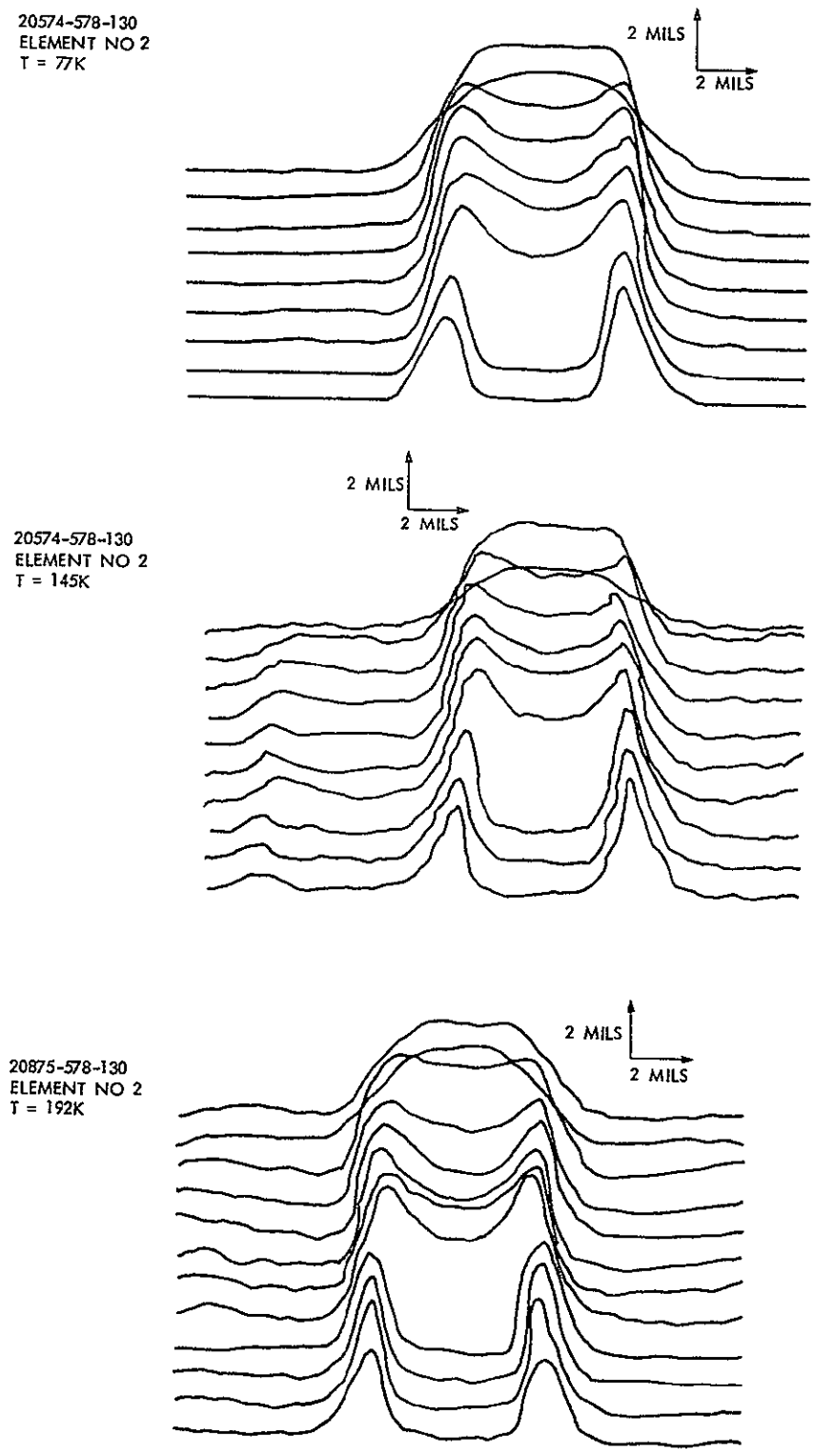

Figure 3-5 Spot Scan Measurements of a n^+–p Photodiode (5 x 5 mil^2 Active Area) at 77 and 193 K.

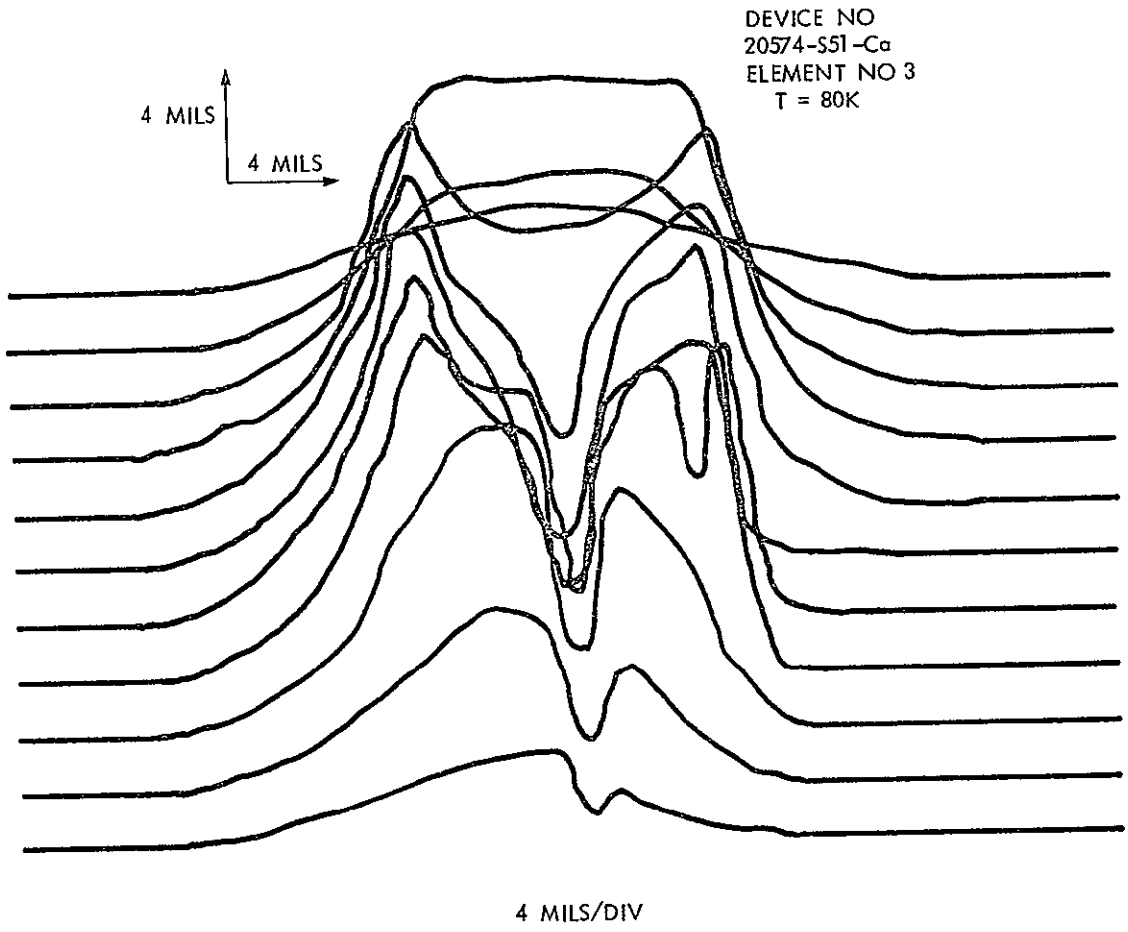

Figure 3-6 Spot Scan Measurements of a Detector Element at 80 K (Junction area = 10 x 10 mil^2)

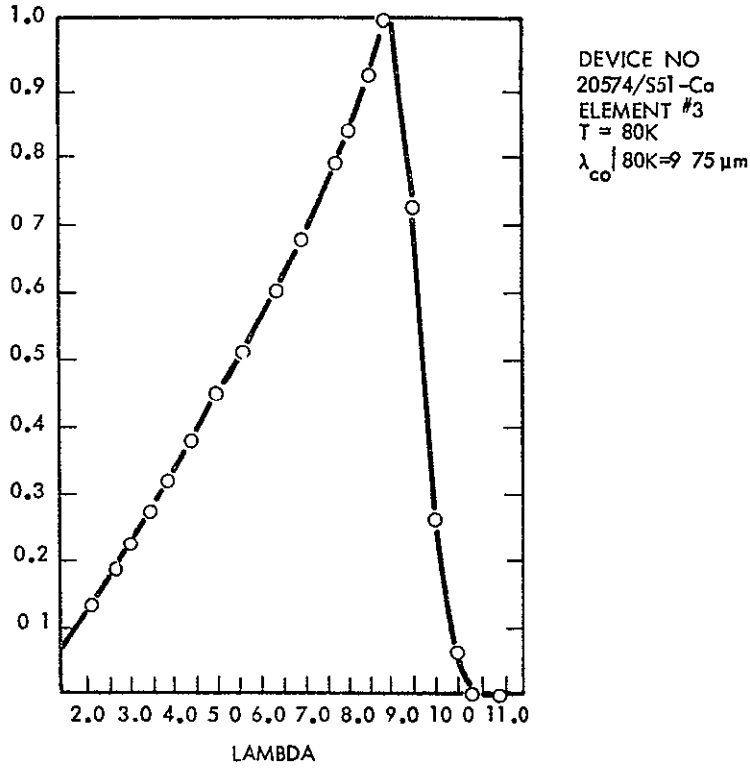

Figure 3-7 Spectral Response for the n^+–p Junction Shown in Figure 3-3 Photodiode at 80 K.

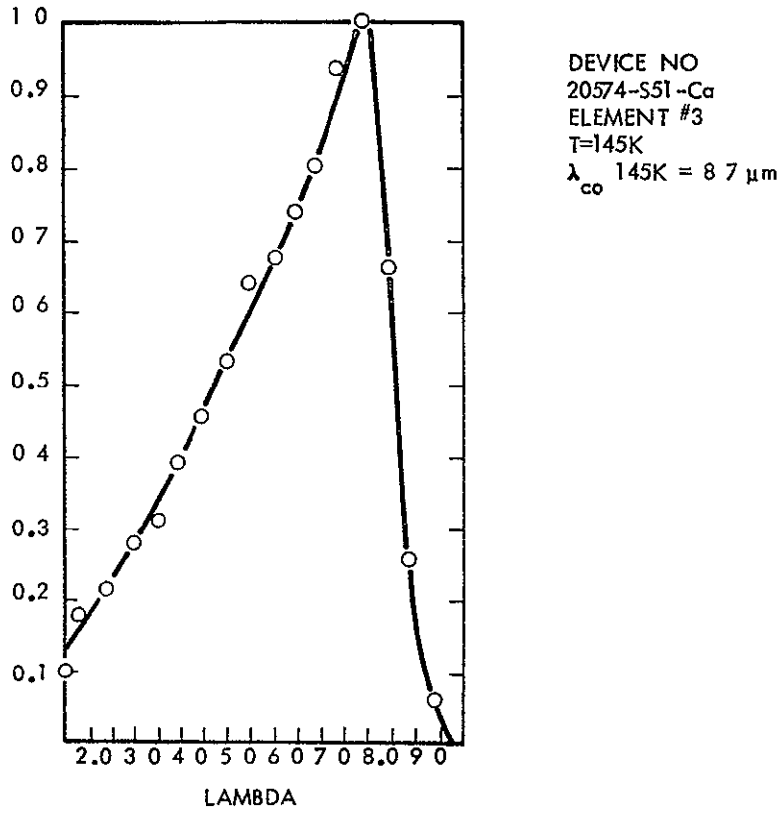

Figure 3-8 Spectral Response for the Same Element as in Figure 3-3 at 145 K

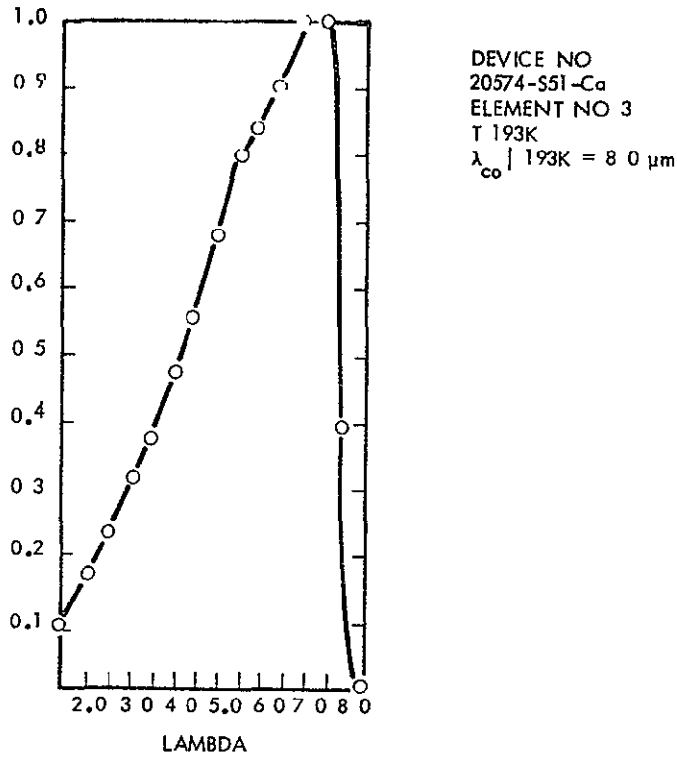

Figure 3-9 Spectral Response for the Detector Element Shown in Figure 3-3 at 193 K

Table 3-1 MEASUREMENTS OF R_oA FOR A TEN ELEMENT ARRAY AT 81, 150 AND 198 K RESPECTIVELY

DEVICE NO · 20474/S129/Ba

$A_J = 6.45 \times 10^{-4}$ cm^2, $A_{opt} = 1.09 \times 10^{-3}$ cm^2,

ELEMENT NO	λ_{co}|80 K	R_oA_{opt}|81 K	R_oA_{opt}|150 K	R_oA_{opt}|198 K
#1	11.9 µm	1.5 ohm-cm^2	1.10×10^{-2} ohm-cm^2	6.90 x 10-3 ohm-cm^2
#2	11.8	2.7	1.03×10^{-2}	4.54×10^{-3}
#3	11.8	3.1	1.24×10^{-2}	7.20×10^{-3}
#4	11.6	3.1	1.05×10^{-2}	5.20×10^{-3}
#5	11.5	3.5	1.01×10^{-2}	4.54×10^{-3}
#6	11.3	4.3	1.30×10^{-2}	6.20×10^{-3}
#7	10.9	2.4	1.50×10^{-2}	5.45×10^{-3}
#9	11.7	3.1	9.4×10^{-3}	3.9×10^{-3}
#10	11.85	2.0	8.5×10^{-3}	4.01×10^{-3}
#11	12.0	1.7	9.1×10^{-3}	4.54×10^{-3}

3.3.4 Quantum Efficiency

Quantum efficiencies were measured routinely on these detector arrays and the value of η was found to vary between 50 to 80%. Measured values of η on a series of detector arrays are summarized in Table 3–2.

Table 3-2 SUMMARY OF THE DETECTOR ARRAY PERFORMANCE AT 145 K

DEVICE NO	λ_{co} | 145 K	R_oA_J | 145 K	R_oA_{opt} 145 K	η	D^*_λ (2π, 1 kHz, 145 K) Calculated	D^*_λ (2π, 1 kHz, 145 K) Measured
20474-S129-Ac Element No 5	8 0 µm	0 055 Ω-cm^2	0 093 Ω-cm^2	0 45	$9\,9 \times 10^{-9}$	$1\,0 \times 10^{9}$ cm √Hz/W
Element No 23	7 5	0 110	0 186	0 56	$1\,6 \times 10^{10}$	$2\,1 \times 10^{9}$
20474-S129-Ad Element No 6	7 8	0 05	0 084	0 50	$1\,0 \times 10^{10}$	$1\,1 \times 10^{9}$
Element No 14	8.2	0 05	0 084	0 53	$1\,1 \times 10^{10}$	$1\,2 \times 10^{9}$
20474-S129-Bc Element No 2	10 9	0 005	0 008	0 68	$6\,0 \times 10^{9}$	$2\,3 \times 10^{8}$
Element No 5	10 4	0 005	0 008	0 71	$5\,9 \times 10^{9}$	$7\,5 \times 10^{8}$
Element No 11	10 7	0 005	0 008	0 70	$6\,0 \times 10^{9}$	$4\,0 \times 10^{8}$
20474-S129-Bd Element No 4	10 0	0 009	0 015	0 67	$7\,4 \times 10^{9}$	$9\,2 \times 10^{8}$
Element No 6	10 1	0 008	0 013	0 58	$6\,0 \times 10^{9}$	$8\,2 \times 10^{8}$
Element No 7	10 3	0 01	0 017	0 58	$7\,0 \times 10^{9}$	$5\,0 \times 10^{8}$
20574-S53-B Element No 6	7 5	0 03	0 051	0 65	$9\,9 \times 10^{9}$	$9\,0 \times 10^{8}$
Element No 9	7 4	0 035	0 059	0 53	$8\,6 \times 10^{9}$	$7\,0 \times 10^{8}$
20574-S81-A Element No 3	8 0	0 06	0 101	0 52	$1\,2 \times 10^{10}$	$5\,0 \times 10^{9}$
Element No 4	7 8	0 08	0 135	0 50	$1\,3 \times 10^{10}$	$8\,5 \times 10^{9}$
Element No 8	7 8	0 08	0 135	0 50	$1\,3 \times 10^{10}$	$9\,0 \times 10^{9}$
20574-S81-Ba Element No 3	8 0	0 075	0 126	0 57	$1\,5 \times 10^{10}$	$8\,0 \times 10^{9}$
Element No 9	7 7	0 075	0 127	0 62	$1\,5 \times 10^{10}$	$1\,1 \times 10^{10}$
20574-S81-Bb Element No 8	8 0	0 05	0 084	0 62	$1\,3 \times 10^{10}$	$9\,2 \times 10^{9}$
Element No 9	7 8	0 06	0 101	0 61	$1\,4 \times 10^{10}$	$1\,1 \times 10^{9}$
Element No 15	8 24	0 041	0 069	0 66	$1\,3 \times 10^{10}$	$6\,0 \times 10^{9}$
20574-S81-Cb Element No 4	9 0	0 023	0 039	0 60	$9\,6 \times 10^{9}$	$4\,4 \times 10^{9}$
Element No 12	9 3	0 016	0 027	0 58	$8\,0 \times 10^{9}$	$2\,9 \times 10^{9}$
Element No 13	9 2	0 018	0 030	0 63	$9\,0 \times 10^{9}$	$2\,1 \times 10^{9}$
20574-S81-Db Element No 2	8 7	0 029	0 049	0 58	$1\,0 \times 10^{10}$	$5\,4 \times 10^{9}$
Element No 8	8 8	0 028	0 047	0 61	$1\,0 \times 10^{10}$	$4\,8 \times 10^{9}$
Element No 10	8 8	0 025	0 042	0 60	$9\,7 \times 10^{9}$	$5\,3 \times 10^{9}$

$A_J = 6\,45 \times 10^{-4}$ cm^2

$A_{opt} = 1\,09 \times 10^{-3}$ cm^2

3.3.5 Detectivities

Detectivity measurements were performed on a series of detector arrays at 80, 120 and 145 K. Table 3–2 summarizes the measured detectivities on a number of detector arrays at 145 K. Similar measurements on arrays delivered to NASA/JSC are summarized in Appendix A and B respecitvely. These measurements were performed with a 180^{o} FOV and at a frequency of 1 kHz. Measured values were observed to be lower than those calculated using R_oA of the photodiodes. This discrepency can be explained on the basis of excess 1/f noise at 1 kHz, which would reduce the measured signal to noise ratio.

3.3.6 Measurement of Minority Carrier Lifetime

3.3.6.1 Introduction

One of the most important parameters determining the ultimate performance of a photodiode is bulk minority carrier lifetime. In the past a number of indirect techniques have been utilized for minority carrier lifetime determination, such as modeling of the zero bias impedance data to the appropriate current limiting mechanism. This task has been carried out over the temperature range of 77 to 200 K. In carrying out such analysis, one has to assume values for n_i, N_A, τ_e, and μ_e over the given temperature range. All the above parameters have a strong temperature dependence. In carrying out these calculations, a value of minority carrier lifetime is assumed such that a good fit between theory and experimental data is obtained.

In this section Reverse Recovery Technique[15] is described and its application to minority carrier lifetime determination in (Hg,Cd)Te is discussed.

3.3.6.2 Reverse Recovery Technique

A conceptual model of the measurement circuit is shown in Figure 3–10. For the case of an n^+–on–p diode, a forward current, I_F, composed primarily of electrons is injected into the p–side. The transient response determined the lifetime of the electrons on the p–side. This represents the bulk minority carrier lifetime of the diode.

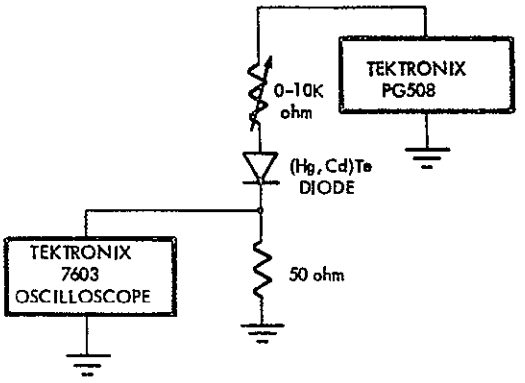

Figure 3-10 Reverse Recovery Circuit

By applying a sudden reverse bias, a transient curve consisting of two phases can be observed. The first phase is one of constant reverse current, I_R, and lasts for a storage time, t_s. During this time the junction voltage remains positive; the current is supported by the previously injected minority carriers. The reverse current is limited to a constant value of I_R by the applied reverse bias V_R and series resistance of the circuit. After a time t_s, the electron density at the junction is near zero. The subsequent exponential decay phase of current, determined by diffusion and recombination on the p–side, establishes the normal reverse current I_{sat}, as shown in Figure 3–11. The minority carrier lifetime can be calculated by either of these reverse current phases. However, the constant current phase lends itself to an easier calculation, is less susceptible to trapping effects than the decay phase, and the time period is easier to accurately determine.

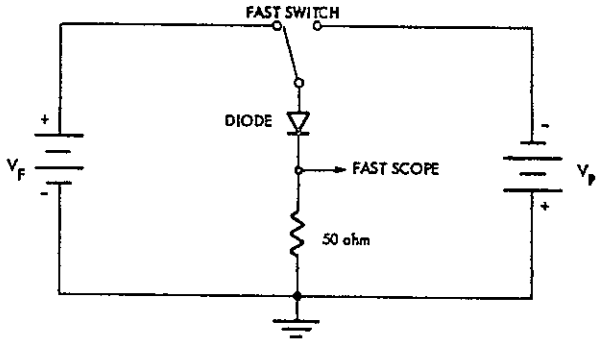

Figure 3-11a Schematic Diagram of Reverse Recovery Circuit

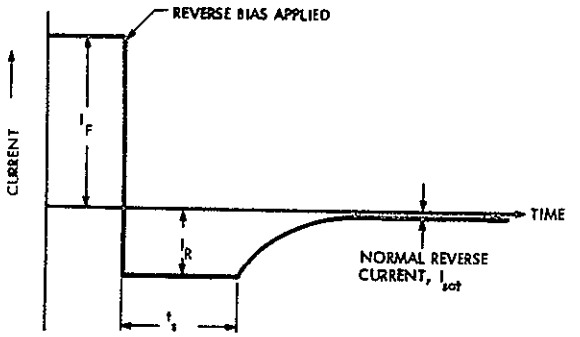

Figure 3-11b Current vs Time Measured in Reverse Recovery

Experimentally, the reverse recovery measurement system is quite simple. The forward and reverse voltages are supplied by a Tektronix 508 Pulse Generator with forward-to-reverse transition time of less than 5 nanoseconds. The positive and negative voltage levels can be individually controlled to vary the ratio of I_F/I_R.

Because the conventional reverse recovery circuits of the literature prove unacceptable in the detection of the short lifetimes in (Hg,Cd)Te, it was necessary to specifically address the problem of circuit noise. One of the distinguishing features employed was the use of no external capacitor in the circuit and only two resistors. Hence, the inductive effect of a large external capacitor was eliminated in this high frequency application. A 10 K ohm variable resistor is used in series with the diode to provide stability and minimize noise. Actual waveform measurements are taken across a 50-ohm resistor that is matched to the input impedance of the oscilloscope. Coaxial leads emanating from a shielded box are used to minimize the noise in the diode under test. The scope is a Tektronix 7603 with a 100-MHz bandwidth. Storage times down to about 20 nanoseconds have been reliably measured on this system. In operation, forward injection I_F, is held at a constant value while I_R takes a range of values. This is because the amount of injected charge, determined by I_F, can affect the lifetime (e.g., by filling of traps).

Variable temperature measurements were facilitated through the use of a 24-pin stainless steel variable temperature dewar. A Lake Shore Cryotronics DT-500 temperature sensor accurate to within 0.2 K was used to monitor the temperature of the diode array. A 30-volt variable voltage source was connected to the heater. A circuit box employing feedback techniques was successfully used to maintain a constant temperature

across the diode array as well as provide direct temperature readout on a digital voltmeter. A diagram of the circuit used is shown in Figure 3-11a.

There are many methods described in the literature for extracting minority carrier lifetime from the measured reverse recovery parameters (t_s, I_F, I_R) defined in Figure 3-11b. Several of them treat special cases, such as an abrupt junction with infinite base width, and come up with easily evaluated expressions for lifetime. Others provide a more general treatment, but the mathematics becomes prohibitively complicated. The methods most applicable for our purposes are as follows:

(1) From Kingston[16], Lax and Neustadter[17], and others. For the case of an abrupt junction, with a very thick base region ($W >> L_e$), both papers derive the following expression:

$$\text{erf} \sqrt{\frac{t_s}{\tau_e}} = \frac{1}{1 + I_R/I_F} \tag{32}$$

This method requires only a single reverse recovery curve to determine the lifetime.

(2) Kuno[15] does not assume an abrupt junction, nor does he assume a specific base width (thickness of the lightly doped side of the junction).

His expression is:

$$t_s = \tau_e \ln (1 + I_F/I_R) + \tau_e \ln (1 + \tau_R/\tau_e) \tag{33}$$

Here τ_R is a parameter defined by the relation $Q(\tau_s) = I_R \tau_R$, where $Q(\tau_s)$ is the charge remaining in the base region at the end of the constant-current phase. τ_R has no physical significance as a lifetime, and is <u>assumed</u> by Kuno to be a constant. Kuno's method is to plot t_s versus $\ln (1 + I_F/I_R)$; the slope is then τ_e. This requires a series of reverse recovery measurement to be made, over a range of I_F/I_R ratios.

(3) Moll, Krakauer, and Shen[18] (for narrow base graded junctions), Moll and Hamilton[19] (for p-i-n junctions), both derive the approximation:

$$t_s = \tau_e \ln (1 + I_F/I_R) \qquad (34)$$

The assumption used in that the field associated with the graded junction sweeps out all the injected carriers by the end of the storage period. This is equivalent to $Q(\tau_s) = 0$ in Kuno's formulation; in that case, equation (33) reduces to (34). Methods listed in (16,17) require just one reverse recovery measurement to determine the lifetime.

Each of the above methods involve some questionable assumptions. Method (1), for instance, is for the case of an ideal abrupt junction. Method (1) also assumes a lightly doped region of thickness W, such that $W \gg L_e$, the minority carrier diffusion length. While this assumption is reasonable for diodes fabricated on thick wafers, however, it does not hold for thin photodiode structure.

Method (2) depends on the assumption that τ_R, a defined quantity, is a constant independent of I_F/I_R. Any variation of τ_R with I_F/I_R will change the slope of a "Kuno Plot," and hence the calculated lifetime. Kuno gives no physical explanation for the linear relationship between $Q(\tau_s)$ and I_R, but rather points to experimental fits of t_s vs ln $(1 + I_F/I_R)$, which <u>do</u> follow Equation (33). Our data, also, have given consistently good linear fits, well within experimental errors as shown in Figure 3-12.

3.3.6.3 Experimental Results

Devices selected for evaluation were those which had good zero bias impedance and showed good reverse bias characteristics between 77 and 145 K. This generally required that the reverse breakdown voltage of the device under investigation was greater than applied reverse bias during the measurement. This was ensured by selecting photodiodes with reverse breakdown voltages in excess of 0.8 volt. Representative current-voltage characteristics for a typical test device are shown in Figure 3-4.

LIFETIME MEASUREMENT BY REVERSE RECOVERY

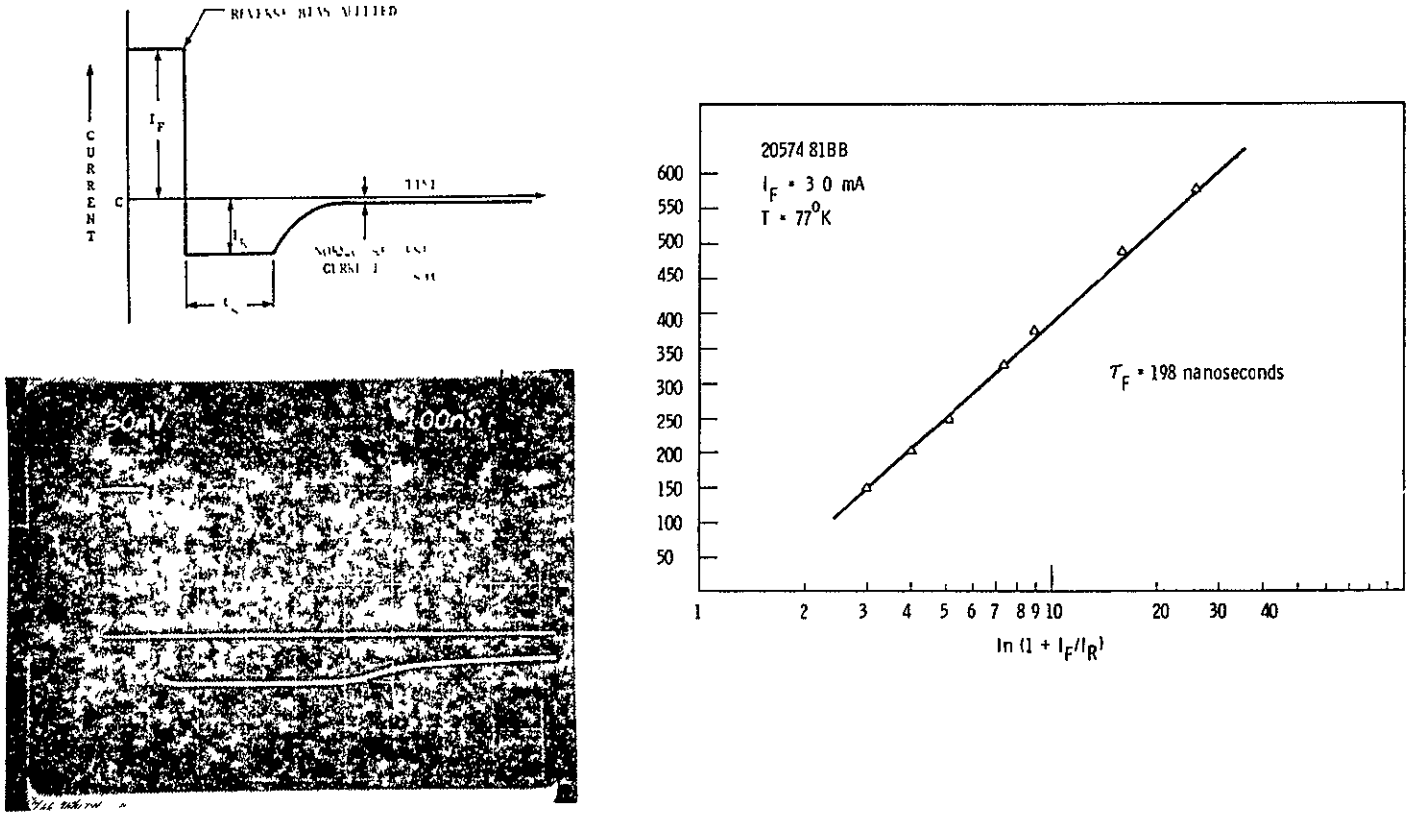

Figure 3-12 Illustration of the Reverse Recovery Technique and the Experimental Results on a 8 to 14 μm n^+–p Photodiode

Minority carrier lifetime measurements were carried out on several junction photodiodes fabricated on wafers from a crystal with an acceptor concentration in the range of $1.0 - 4.0 \times 10^{16}$ cm^{-3}. Hole concentration of this crystal was adjusted by non-stoichiometry. Similar measurement attempts were also made on photodiode arrays fabricated on wafers from another crystal with carrier concentration in range of $2.0 - 4.0 \times 10^{17}$ cm^{-3}. Due to poor reverse bias characteristics in arrays fabricated from crystal (N_A $1.0 - 4.0 \times 10^{16}$ cm^{-3}. Figure 3-13 presents a typical dependence of minority carrier lifetime on temperature between 77 and 145 K. Measured values of electron lifetime as a function of temperature show a good theoretical agreement with a Shockley-Read type recombination center assuming a trap energy of $E_T = 0.056$ eV. For comparison theoretical calculations for band to band radiative recombination (for $x = 0.234$) are also presented[6]. The results show that measured minority carrier lifetimes are a factor of 2-3 below the radiative limit. Measurements carried out on other devices followed a similar type of temperature dependence with trap energy in the range of $E_T = 0.05 \pm 0.01$ eV. It is evident from Figure 3-14, that minority carrier lifetime in p-$Hg_{0.8}Cd_{0.2}Te$ follows radiative recombination process more closely than the Auger recombination process, which dominates the recombination mechanism in n-type $Hg_{0.8}Cd_{0.2}Te$[6].

Values for minority carrier mobility in p-$Hg_{0.8}Cd_{0.2}Te$ were computed using the following relationship:

$$R_o A_j = \sqrt{q/kT} \quad N_A/n_i^2 \sqrt{\frac{\tau_e}{\mu_e}} \qquad (35)$$

For an n^+-p junction photodiode array (Device #20574-581-DB, $x = 0.219$, $_{co}$ 80 K = 10.0 μm minority carrier mobility was computed using the above relationship. $R_o A_j$, τ_e, and N_A were measured experimentally and knowing $_i$, the intrinsic carrier concentration electron mobility was computed. Results are presented in Figure 3-15, where for comparison theoretical electron mobility [20] in n-type $Hg_{0.8}Cd_{0.2}Te$ is also plotted. Between the temperature range of interest, i.e., 77 and 145 K, electron mobility for n-type $Hg_{0.8}Cd_{0.2}Te$ shows a slight temperature dependence and at 77 K the value is estimated to be 1.0 to 2.0×10^5 cm^2/volt - s. Computed values of electron mobility in p-type $Hg_{0.8}Cd_{0.2}Te$ were found to be a factor of 3-5 lower than the corresponding electron mobility in n-type $Hg_{0.8}Cd_{0.2}Te$. Lack of temperature dependence in computed

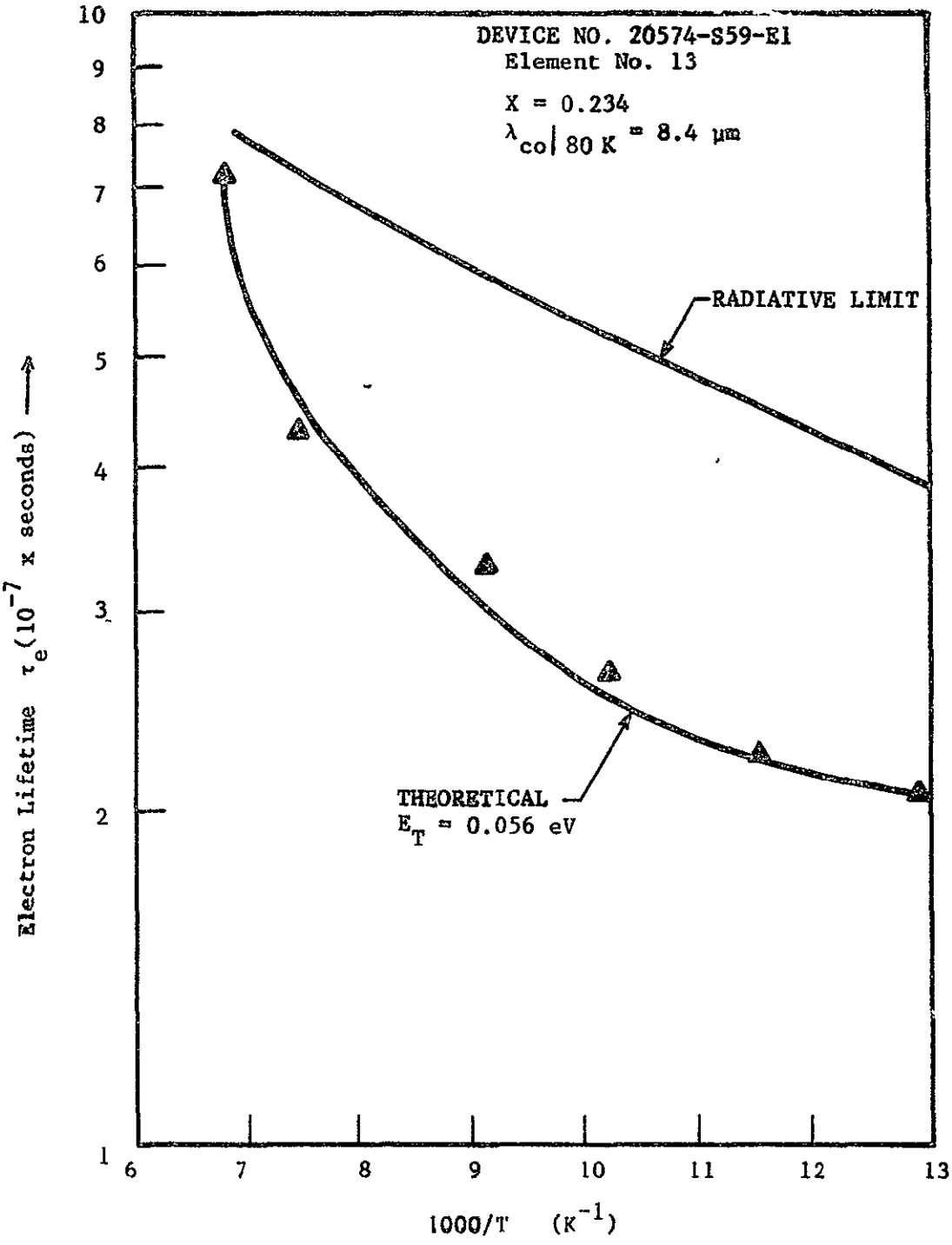

Figure 3-13 Variation of Lifetime as a Function of Temperature on a n^+–p Photodiode. Experimental Results Agree Well with a Shockley-Read Center 0.056 eV above the Valence Band. Radiative Limited Lifetime Calculated Theoretically is also shown.

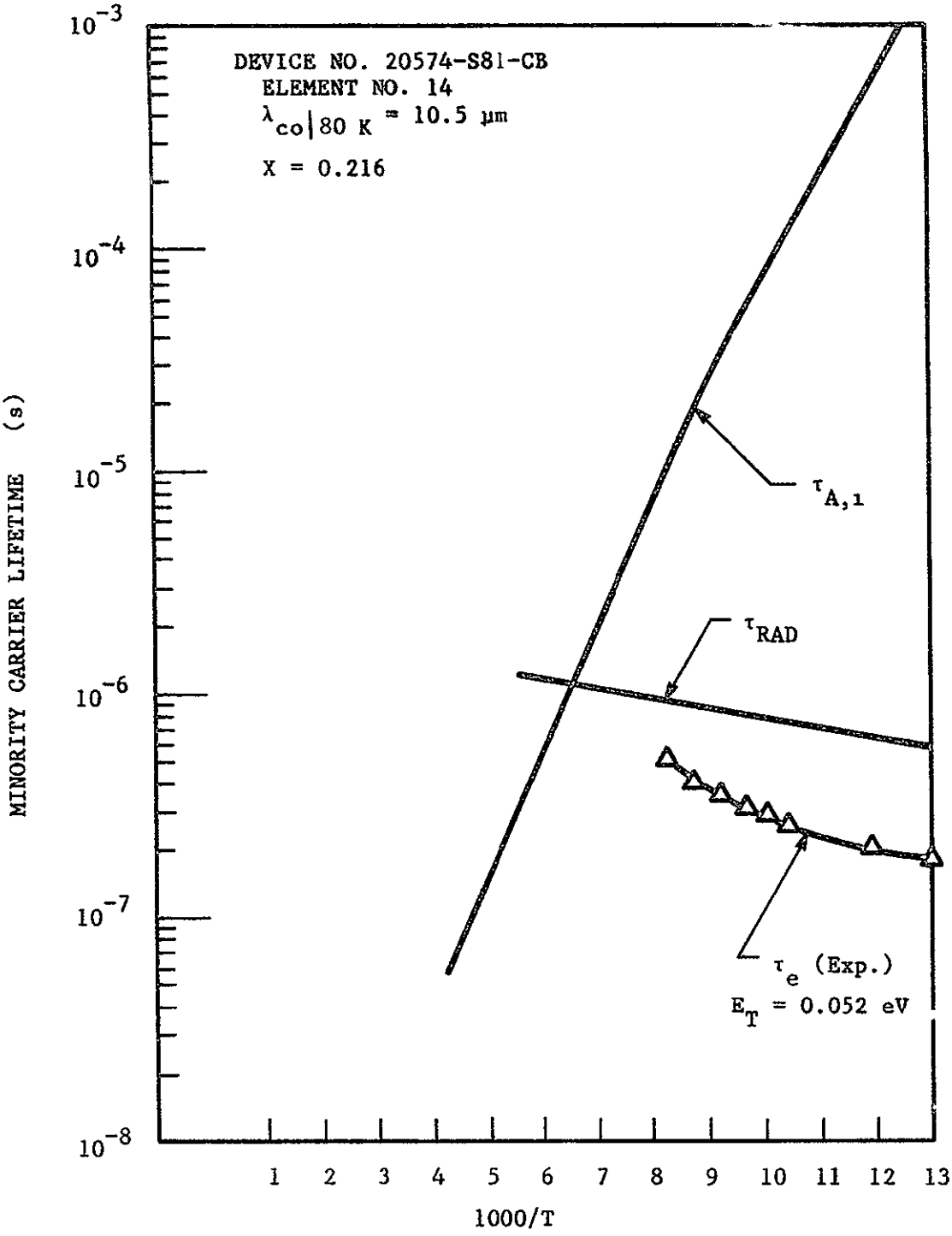

Figure 3-14 Temperature Dependence of Intrinsic Auger Lifetime, Radiative Recombination Lifetime and Experimental Shockley-Read Lifetime Measured on $Hg_{1-x}Cd_xTe$ (x = 0.216).

mobility can be attributed to be due to scattering dominated either by ionized impurities or other structural defects. Further verification of this result would require direct measurement of electron mobility by an alternate technique.

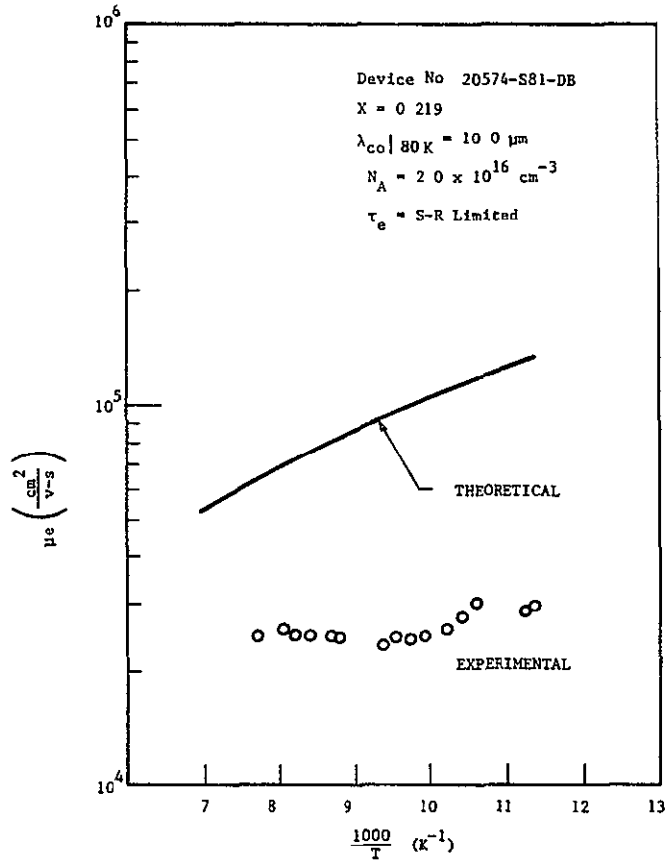

Figure 3-15 Comparison of the Electron Mobility Computed from Modeling Experimental R_oA Product with Measured Minority Carrier Lifetime and the Theoretical Calculated Electron Mobility from the Literature

3.3.7 Comparison of Theory with Experiment

Table 3-2 presents in detail measurements carried out at 145 K on arrays fabricated during this program. Measured quantum efficiency and detectivity at 145 K for these devices are compared with theoretical calculations using the following relationship:

$$D^* = \frac{\lambda q \eta}{hc} \quad \frac{R_oA}{4kT} \qquad (36)$$

This relationship assumes that there is no 1/f noise component contributing to diode noise. Measured values for detectivity for these devices were found to be lower than those calculated using the above relation. This discrepancy is attributed partially to be due to excess 1/f noise at 1 kHz. Also errors in noise measurements at 145 K is believed to be partially responsible for the discrepancies in measured and calculated values.

Similarly comparison was made for the measured R_oA_j (A_j = Junction Area) at 145 K with theoretically calculated performance. Results are shown in Figure 3–16. Calculations of R_oA_j as a function of wavelength at 145 K were carried out using the relationship for a diffusion limited photodiode:

$$(R_oA)^{-1} = \sqrt{\frac{q}{kT}} \cdot \quad q \left[\frac{n_i^2}{N_A} \quad \frac{\mu e}{\tau_e} + \frac{n_i^2}{N_D} \quad \frac{\mu_h}{\tau_h} \right] \qquad (37)$$

where N_A was assumed to be 2×10^{16} cm^{-3}, τ_e was assumed to be radiative limited and mobility was assumed to be 2×10^{-4} $cm^2/volts-s$ (see Section 3.3.6). Agreement of the experimental data with theoretical calculations is excellent. Calculated curve has been drawn for the radiative limited lifetime, where as the minority carrier lifetimes in these devices were a factor of 2–4 below the radiative recombination limit. This would mean that the experimentally measured R_oA_j will be lower by a factor of 2–3 below the theoretical calcualtions. Further improvements in minority carrier lifetime would yield photodiodes, which will match the theoretically predicted performances.

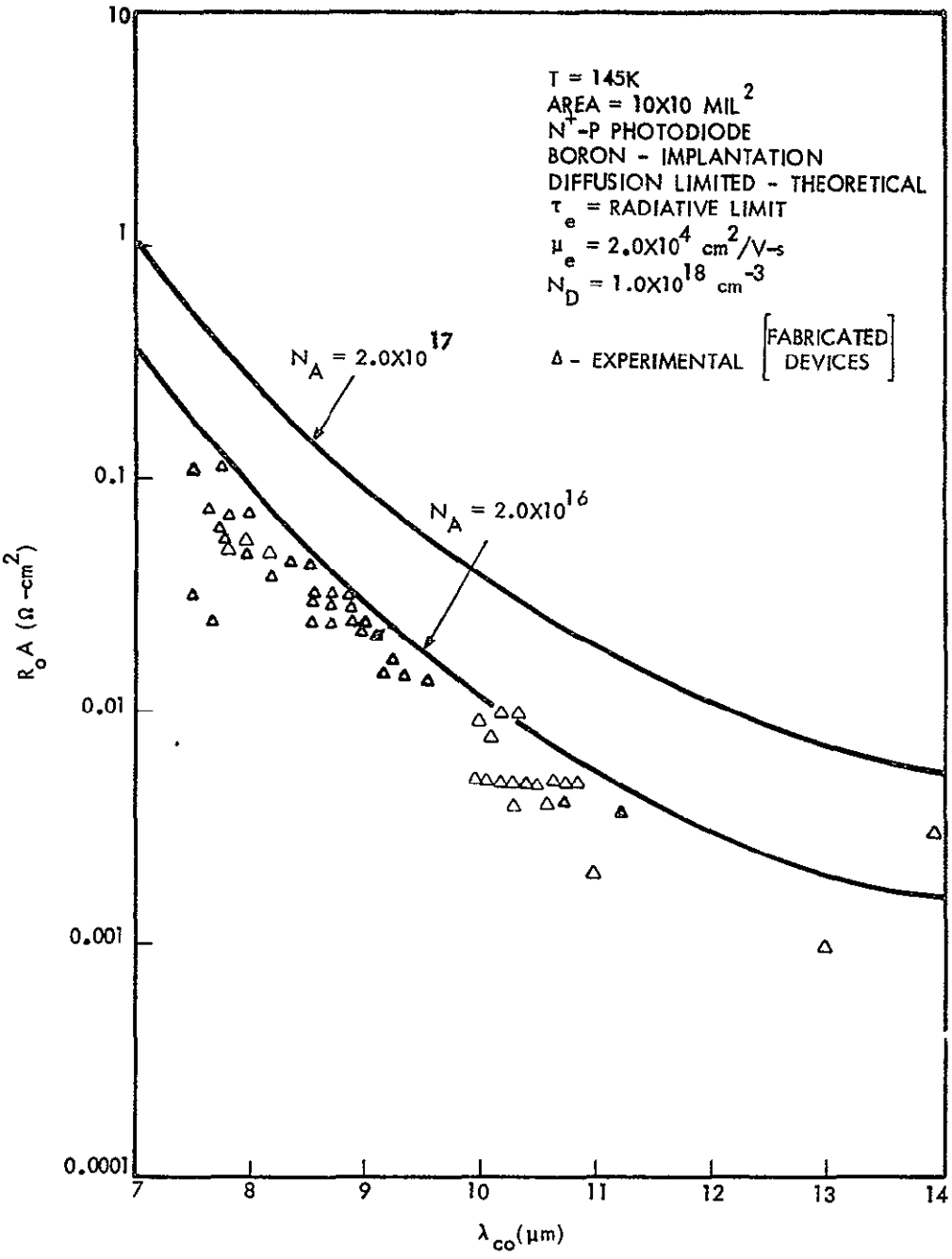

Figure 3-16 Comparison of Theoretically Calculated R_oA with Measured R_oA at 45 K as a function of Cutoff Wavelength for a series of Detector Arrays

SECTION 4
p^+–p ION IMPLANTATION DEVELOPMENT

The approach chosen to form the p–p^+ "electrically-reflecting" or "blocking" backside contact during this program was ion implantation of an acceptor impurity.

There have been many reports in the literature of ion implantation used to form n–type regions in p–type $Hg_{1-x}Cd_xTe$. As discussed in Section 3 of this report, during this program both boron and chlorine were implanted into p–type $Hg_{0.8}Cd_{0.2}Te$ to form n^+–on–p junction photodiodes.

In contrast, there have been no reports in the literature of successful ion implantation of slow diffusing acceptor impurities in $Hg_{1-x}Cd_xTe$. Igras et al[21] recently reported implantation of phosphorus, nitrogen and gold into n–type (Hg,Cd)Te at doses of $1 \times 10^{13} - 1 \times 10^{15}$ ions/cm^2 and energies of 30 – 140 keV with no post-implantation work damage anneal; no formation of a p–type layer was observed. However, Koehler[22] has shown that via implantation of gold in n–$Hg_{1-x}Cd_xTe$, it is possible to form a p^+–n junction structure; Gold being a fast diffuser in $Hg_{0.8}Cd_{0.2}Te$[9,10] was ruled out for fabrication of p–p^+ junction.

A wide variety of atomic species are available for use as acceptors in $Hg_{1-x}Cd_xTe$. Many of these are eliminated from use in a p^+–p backside reflecting contact due either to the species having a large diffusion coefficient or large atomic mass. Gold, with a large diffusion coefficient, is an acceptor in $Hg_{1-x}Cd_xTe$, but would rapidly diffuse through the thin (10–15 μm) bulk region of a device with a backside reflecting contact. Antimony is an acceptor with a small diffusion coefficient, but its large mass would result in an inordinate amount of damage to the thin bulk region upon ion-implanting.

The atomic species chosen for the backside reflecting contact dopants in this program were phosphorus and arsenic. Both are slowly diffusing acceptors in $Hg_{1-x}Cd_xTe$. Their masses were expected to be low enough such that the damage caused by their implantation should be able to be annealed out.

4.1 IMPLANT PROFILE CALCULATIONS

To determine the concentration of the implanted ions as a function of distance into the p-type $Hg_{0.8}Cd_{0.2}Te$, the implant profiles in $Hg_{0.8}Cd_{0.2}Te$ for phosphorus, arsenic, and antimony were calculated using the LSS theory.[23] These profiles are shown in Figures 4-1 through 4-3.

4.2 IMPLANT EXPERIMENTS

Phosphorus was implanted at an energy of 150 KeV and a fluence of 1×10^{15} cm^{-2}. Arsenic was implanted at an energy of 200 KeV and a fluence of 1×10^{15} cm^{-2}.

p-type $Hg_{1-x}Cd_xTe$ material was selected with a nominal alloy composition around x = 0.21. The dominant acceptors in the material used were probably stoichiometric defects (metal vacancies) at concentrations of about $1-5 \times 10^{17}$ cm^{-3} (crystal 11276) and $2-4 \times 10^{16}$ cm^{-3} (crystal 20574).

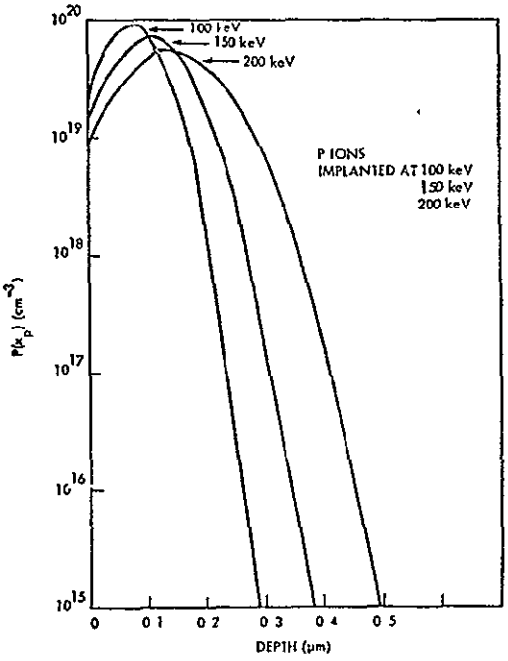

Figure 4-1 Calculated Ion-Implantation Profiles of Phosphorous in $Hg_{0.8}Cd_{0.2}Te$ for a Dose of 1×10^{15} ions/cm^2 at Three Different Energies

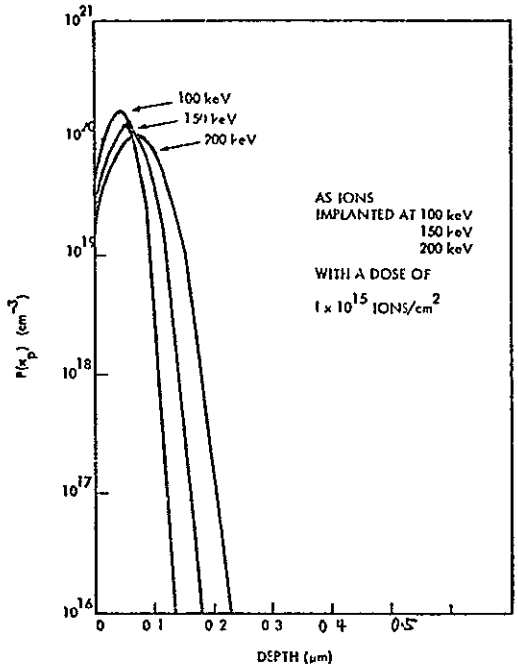

Figure 4-2 Calculated Ion-Implantation Profiles of Arsenic in $Hg_{0.8}Cd_{0.2}Te$ for a Dose of 1×10^{15} ions/cm^2 at Three Different Energies Using LSS Theory

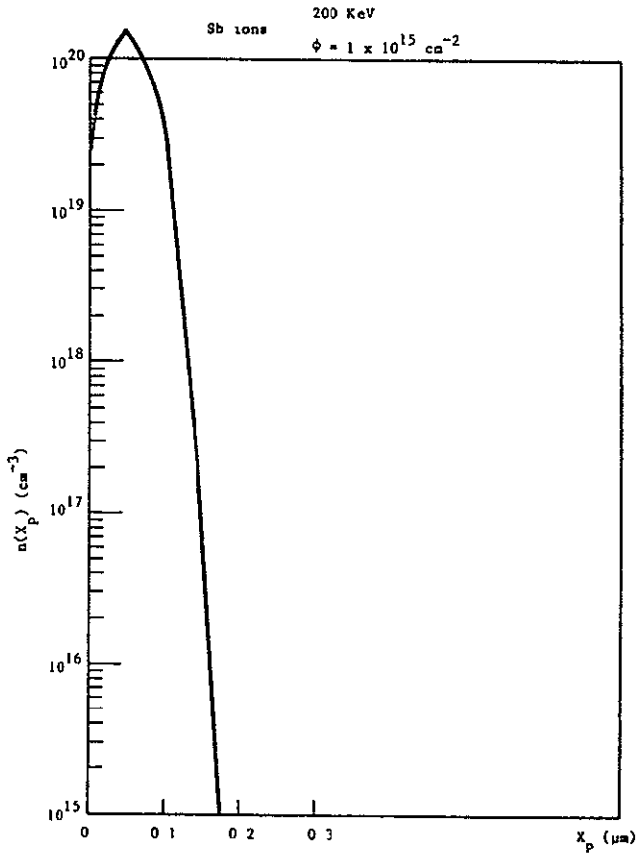

Figure 4-3 Antimony Ion Concentration as a Function of Distance into the $Hg_{1-x}Cd_xTe$ Substrate for Ions Implanted at 200 K, Dose = 1×10^{15} ions/cm^2 LSS Theory

All phosphorus and arsenic implants were done with about 1000 Å of ZnS on the (Hg,Cd)Te surface. The ZnS layer would tend to reduce the depth of the calculated implant profiles shown in Figures 4-1 to 4-3 somewhat.

Two sample configurations were used in the p^+-implantation: Hall samples and tapered arrays. After the p^+-implant, the ZnS layer was removed.

4.3 EVALUATION OF IMPLANT ACTIVATION

In order to evaluate the electrical activation of the implanted ions as a function of anneal schedule, witness samples were included with many of the implant runs. These witness implants were through a photoresist mask containing patterns for carrying out van der Pauw Hall effect measurements (Figure 4-4). The witness material was p-$Hg_{1-x}Cd_xTe$, resulting in p^+-p van der Pauw Hall structures.

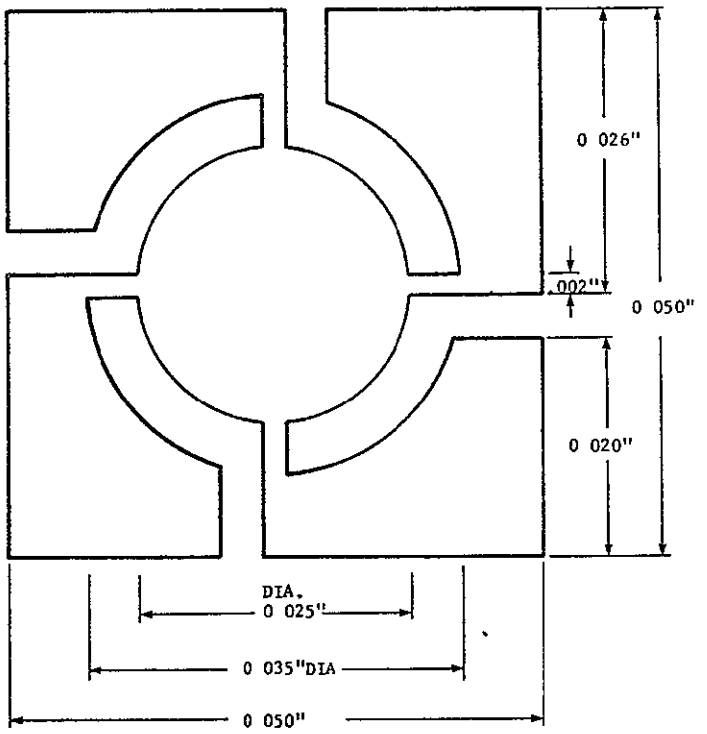

Figure 4-4 Van der Pauw Hall Pattern

Contact to the van der Pauw samples was made with Pb–Ni electrodes. These were utilized since the standard p–contact, gold, is an acceptor in p–$Hg_{1-x}Cd_xTe$. Its acceptor behavior and high diffusion coefficient in $Hg_{1-x}Cd_xTe$ could easily cause erroneous results from the Hall measurements, due to doping of the thin implanted layer. The Pb–Ni electrodes (95% Pb, 5% Ni) are very stable, and each constituent is neutral and a slow diffuser in $Hg_{1-x}Cd_xTe$.

4.3.1 Phosphorus

The devices which were implanted with phosphorus p^+ layers showed the best performance, and the observed increase of the zero bias impedance (R_o) with decreasing device thickness occurred on a phosphorus-implanted sample.

Evaluation of the van der Pauw Hall data must be done with caution. The shallow penetration depth of the implanted ions (~0.3 μm) results in an implanted layer which could easily have a higher resistance than the bulk material. Mixed conduction effects can manifest themselves. The effect of surface states on such a thin layer, especially, if the layer is highly damaged from implantation, can also lead to ambiguous results. Sample Hall data for the phosphosus implanted samples are shown in Table 4–1. Due to a lack of knowledge of the exact implantation depth, the values of hole concentration are order-of-magnitude, rather than exact.

Table 4–1 **HALL DATA (TAKEN AT 77 K) ON SAMPLES OF p–TYPE $Hg_{0.8}CD_{0.2}Te$ IMPLANTED WITH PHOSPHORUS (150 KeV, 1×10^{15} cm^{-2}) AND ANNEALED AFTER IMPLANT FOR 2 HOURS AT VARIOUS TEMPERATURES**

Sample No.	Anneal Temp. (°C)	Anneal Time (Hrs.)	Hole Concentration (cm^{-3})	Hall Mobility ($cm^2/V-s$)
11276 S104.5 A	150	2	4×10^{20}	2×10^2
11276 S103 A1	150	2	1×10^{21}	1×10^2
11276 S104.5 C	175	2	1×10^{21}	1×10^2
11276 S104.5 D	200	2	1×10^{21}	1×10^2
11276 S103 A2	200	2	1×10^{20}	2×10^2

4.3.2 Arsenic

The arsenic ions were implanted at an energy E = 200 KeV with a fluence = 1×10^{15} cm^{-2}. Under these conditions, according to the LSS theory, the ions penetrated approximately 0.2 micrometer into the $Hg_{1-x}CD_xTe$ sample. Witness samples to be used for Hall measurements were annealed according to the schedules shown in Table 4–2. If the ions penetrated 0.2 micrometer into the substrate, and were 100 percent electrically active, a hole concentration $p = 5 \times 10^{19}$ cm^{-3} would be expected. Comparing this value with the experimental values in Table 4–2 indicates that there is an additional source of holes in those samples which received an implant, which is not accounted for by the implanted ions. As the anneal temperatures are increased, the measured carrier concentration decreases. This can be explained by implant-induced lattice damage behaving as a source of holes. As this damage is annealed out, the effect of these damage sites is removed, revealing the behavior of the implanted species.

Table 4–2 **HALL DATA (TAKEN AT 77 K) ON SAMPLES OF p–TYPE $Hg_{0.8}Cd_{0.2}Te$ IMPLANTED WITH ARSENIC (200 KeV, 1×10^{15} cm^{-2}) AND ANNEALED AFTER IMPLANT**

Sample No.	Anneal Temp. (°C)	Anneal Time (Hrs.)	Hole Concentration (cm^{-3})	Hall Mobility ($cm^2/V-s$)
11276 S63 A	No Implant	–	8×10^{17}	3×10^{2}
11276 S63 E	No Anneal	–	2×10^{22}	3×10^{1}
11276 S63 B	150	2	4×10^{21}	2×10^{2}
11276 S63 C	175	2	2×10^{21}	2×10^{2}
11276 S63 D	200	2	2×10^{21}	2×10^{2}

Due to the large mass of the arsenic ions, and the resultant implantation-induced lattice damage, phosphorus was chosen as the p^+ dopant for the p^+–p backside reflecting contact.

SECTION 5
n^+–p–p^+ JUNCTION PHOTODIODE EXPERIMENTS

During the latter part of this program, experiments with n^+–p–p^+ $Hg_{0.8}Cd_{0.2}Te$ junction photodiodes were performed. The purpose of these experiments was to demonstrate experimentally that diffusion current actually could be reduced by reducing the p–region thickness to values less than a diffusion length and then terminating the p–region with a p–p^+ boundary. The experiment involved a specially designed array of n^+–p junctions formed on p–type base material with a tapered thickness. The opposite side of the tapered p–type strip was ion implanted with phosphorus to form a p–p^+ boundary.

Such an array configuration would provide ideally a set of n^+–p–p^+ photodiodes in which only the thickness d of the p–type base region varied in a known manner from element to element. By plotting the diffusion current (or equivalently) the R_oA product in a diffusion-dominated temperature range) versus the p–region thickness, one would be able to determine whether diffusion current varied with p–region thickness and infer some information about the effective recombination velocity of the phosphorus-implanted p–p^+ boundary.

For these experimental n^+–p–p^+ tapered arrays, p–type $Hg_{0.8}Cd_{0.2}Te$ starting material was chosen in which minority-carrier diffusion lengths in the range of 25–50μm had been observed. The tapered array configuration, described in the following section, provided p–region thicknesses ranging from 5 μm to about 40 μm. Hence it was expected that effects due to the p–p^+ boundary being within a minority carrier diffusion length of the n^+–p junction should be evident. If the diffusion-limited R_oA product <u>increased</u> with decreasing p–region thickness d, this would indicate that the p–p^+ boundary was indeed acting as a blocking contact. If, on the other hand, the diffusion-limited R_oA product <u>decreased</u> with decreasing d, this would indicate that the p–p^+ boundary is acting more like an ohmic contact.

Several attempts were made to fabricate tapered n^+–p–p^+ $Hg_{0.8}Cd_{0.2}Te$ arrays for this experiment. Various fabrication process problems were encountered in each case, resulting in tapered arrays with large amounts of excess junction current and, in some instances, with actual inversion of the p–type surface. In most of the arrays fabricated, too few of the elements exhibited diffusion current over a wide enough temperature range to enable any conclusions about the variation of diffusion current with p–region thickness to be drawn.

Some of the major fabrication and process problems with the n^+–p–p^+ tapered array encountered in this program were recently solved on another program at Honeywell. The results on improved tapered arrays will be published [24]. In this section, some data on one of the tapered arrays fabricated on this program are presented and discussed.

5.1 TAPERED n^+–p–p^+ ARRAY DESIGN AND FABRICATION

The configuration of the tapered n^+–p–p^+ $Hg_{0.8}Cd_{0.2}Te$ array is shown in Figure 5–1.

The fabrication steps were as follows. A wafer of p–type $Hg_{0.8}Cd_{0.2}Te$ was lapped and polished to remove all diamond saw induced damage, and then chemically polished to remove any damage which might be left over from the lapping procedure. Following these steps, the sample was rinsed well in order to remove any chemical residue, and then the surface was passivated.

The sample was given an ion implantation of phosphorus to form the p^+ layer. The passivation was then removed and an electrode was evaporated over the entire back surface to form the common p–side electrical contact. In order to produce the taper, the sample was epoxied, backside down, to a substrate which had been lapped to a taper of $\sim 1/2^o$. The entire wafer-substrate combination was then lapped, thus giving a taper of $\sim 1/2^o$ to the $Hg_{1-x}Cd_xTe$ wafer. Photolithography was used to define 3×5 mil^2 diode areas, and boron ions were implanted through this photoresist mask to form the n^+–regions. The post-implant anneal was then carried out according to various schedules of time and

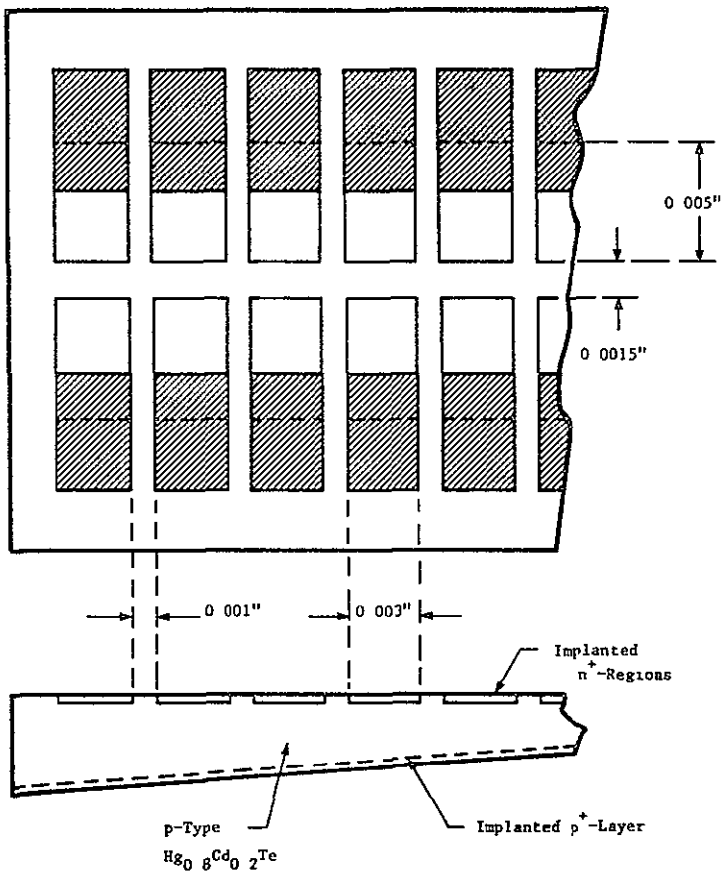

Figure 5-1 Configuration of the Tapered n^+–p–p^+ $Hg_{0.8}Cd_{0.2}Te$ Array. The implanted n^+–regions were each 0.003" x 0.005". The shaded Areas are Evaporated Metal Contact Pads.

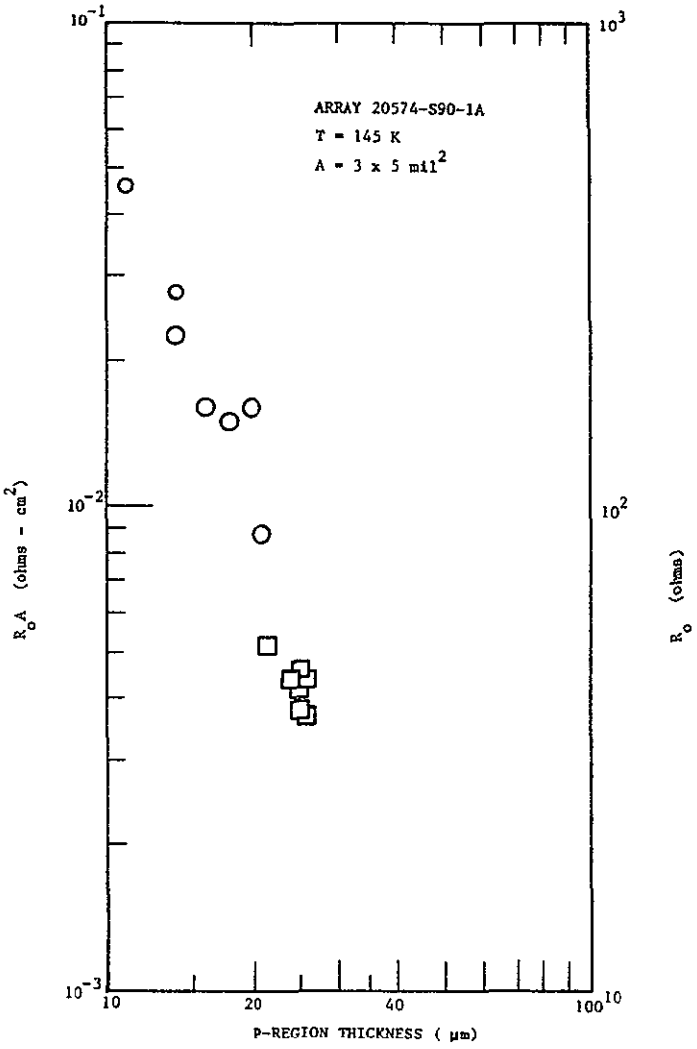

Figure 5-1 Data for the R_oA Products at 145 K Plotted Versus p-region
b Thickness for Tapered array 2-574-S90-1A. These data I
Also appear in Table 5.1. The open circles represent the
First seven elements in Table 5-1. The open squares
Represent the second seven elements which were in a
Region of the Array Suspected of Surface Inversion.

temperature. n^+–side electrodes were defined photolithographically, and gold leads were bonded to the devices. The thickness of each device to be tested was then measured, and the arrays were then mounted into 40 pin flat packs.

Boron implantation was used to form the n^+–regions. The implant energy was 100 KeV and the fluence was 1×10^{15} ions/cm^2. Phosphorus implantation was used to form the p^+–layer. The energy was 150 KeV and the fluence was 1×10^{15} cm^{-2}. For array 20574-S90-1A, which is the array discussed in the rest of this section, the work damage anneal was performed after both implants were done. The anneal was at a temperature of 150° C for 2 hours.

5.2 DATA FOR TAPERED n^+–p–p^+ ARRAY 20574-S90-1A

Table 5–1 summarizes data for selected elements of array 20574-S90-1A. This array contained about 120 elements, of which only 40 were actually contacted. Measured R_oA at 145 K on these elements are also plotted as a function of p–region thickness in Figure XX. Surface inversion of the p–type material over certain regions of this array occurred, and there probably was some residual damage at the p–type surface. The data in Table 5–1 are listed in order of increasing p–region thickness and fall into two groups. Elements 16 through 21 were at the thin end of the array and seem to be less affected by surface damage. Elements 15, 30, 11, 13, 24, 26 and 28 were in a region of the array which showed pronounced surface inversion (as seen in spot scans) and evidence of surface damage (as shown by the low R_o values at 145 K). The measured R_o values for these elements are quite low, both at 145 K and 77 K.

The differences between the two groups of elements listed in Table 5–1 can be seen from a comparison of the behavior of the R_oA_j products as functions of temperature. Data for R_oA_j versus temperature for Elements 16, 18, 20 and 30 are shown in Figures 5–2 through 5–5.

The R_oA curves in Figures 5–2 through 5–5 all show roughly two types of behavior. At lower temperatures, R_oA is weakly dependent on temperature. At higher temperatures, R_oA depends exponentially on temperature.

Table 5-1 DATA FOR SELECTED ELEMENTS FROM TAPERED ARRAY 20574-S90-1A

ELEMENT NUMBER	P-REGION THICKNESS	ZERO-BIAS RESISTANCE R_o (ohms)		R_oA_J PRODUCT (ohms-cm^2) $A_J = 0.97 \times 10^{-4}$ cm^2		CUTOFF WAVELENGTH T = 77 K (μm)
		T = 145 K	T = 77 K	T = 145 K	T = 77 K	
19	11	470	2940	0 046	0 29	*
18	14	222	653	0 022	0 063	*
20	14	286	5210	0 028	0.51	8 0
17	16	160	513	0.016	0 050	8.2
21	18	150	3180	0.015	0 31	*
16	20	164	2200	0 016	0 21	*
22	21	91	1520	0.0088	0 15	8.4
15**	21.5	54	357	0.0052	0 035	8 6
30**	24	45	111	0.0044	0 011	*
11**	25	47	200	0.0046	0.019	8 7
13**	25	46	137	0.0045	0 013	8 6
24**	25	39	167	0 0038	0 016	8.6
26**	25	43	109	0.0042	0.011	8 6
28**	25	39	88	0.0038	0 0085	8.7

* Not Measured

**These elements are from regions of the array which showed inversion of the p-type front surface

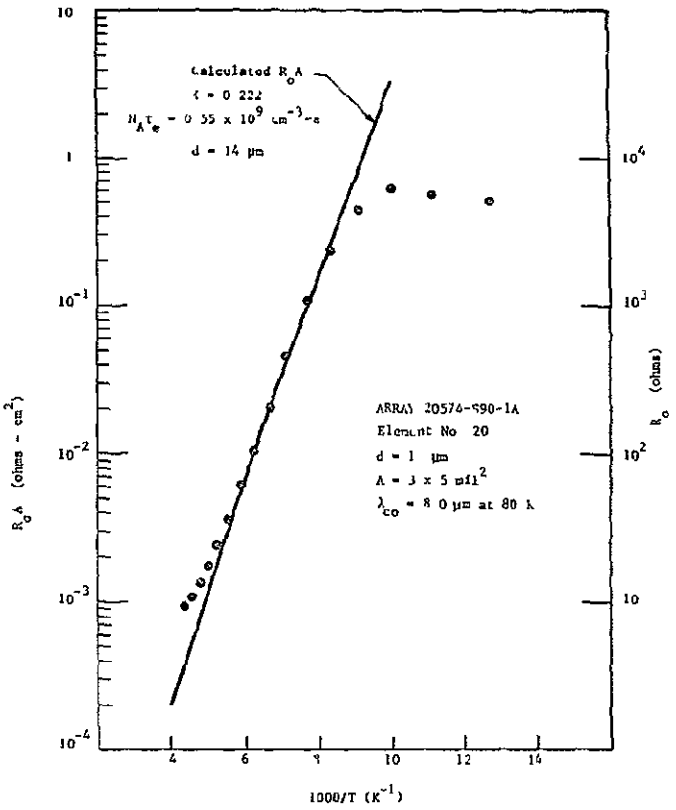

Figure 5-2 R_oA As A Function of Temperature for Element #16 on the Tapered Array (d_o = 20μm)$_{10}$

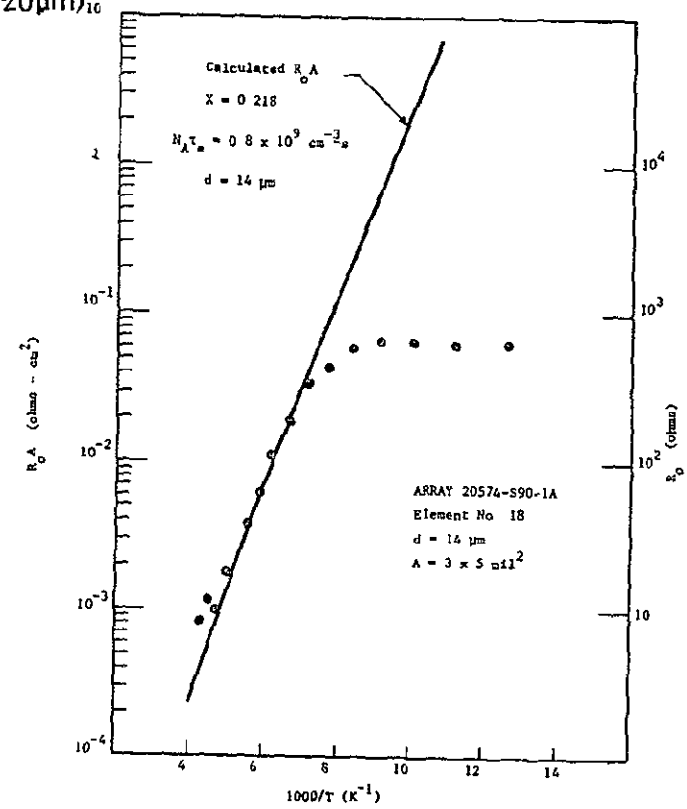

Figure 5-3 R_oA as a Function of Temperature for Element No. 18 on the Tapered Array (d_o = 14μm)

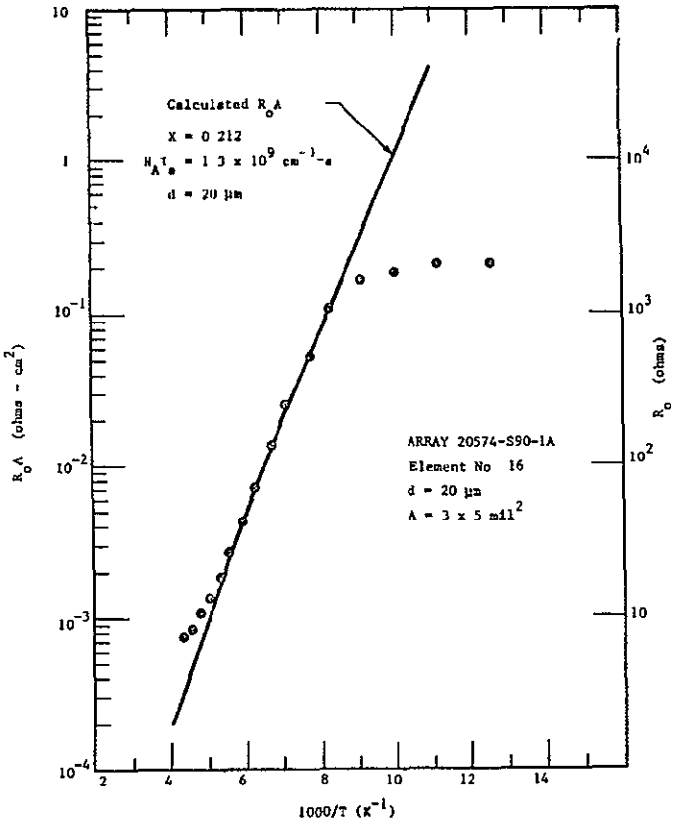

Figure 5-4 R_oA as a Function of Temperature for Element #20 on the Tapered Array (d = 14µm)

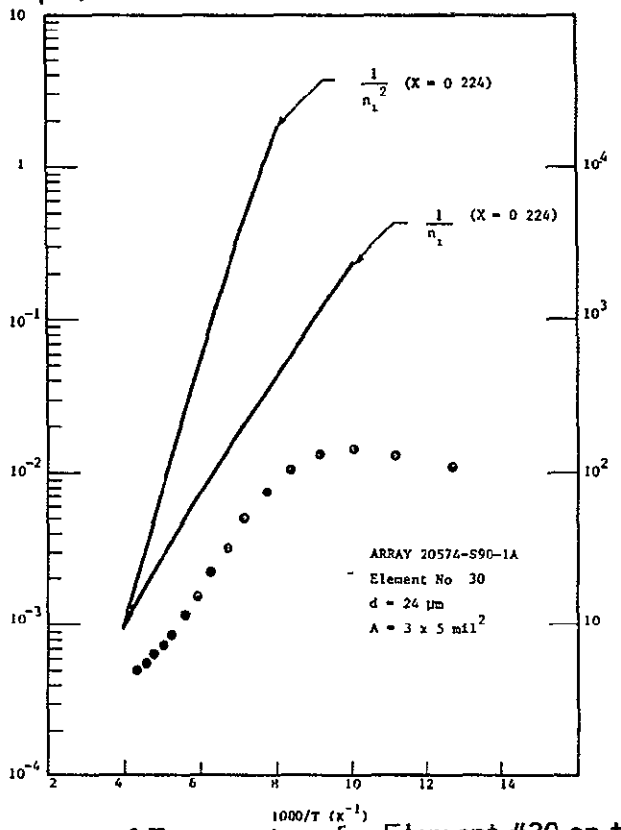

Figure 5-5 R_oA as a Function of Temperature for Element #30 on the Tapered Array Showing Temperature Dependence Proportional to $1/n_i$

In the region of temperature for which R_oA varies exponentially with temperature, the dominant junction current mechanism for Elements 20, 18 and 16 appears to be diffusion current, and for Element 30 it appears to be depletion-layer g–r current. The solid lines in Figures 5–2 through 5–4 are plots of

$$R_oA = \frac{kT}{e^2} \frac{N_A}{n_i^2} \frac{\tau_e}{d} \qquad (36)$$

which was derived in Section 2.2 for the case $d \ll L_e$.

Most of the temperature dependence in this expression comes from the n_i^{-2} term. Values of $Hg_{1-x}Cd_xTe$ alloy composition were chosen in each of Figures 5–2 through 5–4 to give a good fit to the slope of the exponentially varying part of the data. The thickness d used was the actual p-region thickness of each element. The following values of the product $N_A \tau_e$ were chosen to give the best fit of Equation 36 to the data in the exponentially varying range:

Element	$N_A \tau_e$
20	0.55×10^9 cm^{-3} s
18	0.80×10^9
16	1.3×10^9

These values are consistent with an acceptor concentration on the order of 1×10^{16} cm^{-3} and a minority carrier lifetime of about 100 ns.

The I–V curves for Elements 16, 18, 19 and 20 at 145 K are shown in Figures 5–7 and 5–8.

Element 30, located in a region of the array which showed pronounced surface inversion, exhibited no sign of diffusion current. The two solid lines in Figure 5–5 are proportional to n_i^{-1} and n_i^{-2} for an alloy composition of $x = 0.224$. The better fit is to n_i^{-1}, which indicates depletion layer generation-recombination current is dominant above about 110 K.

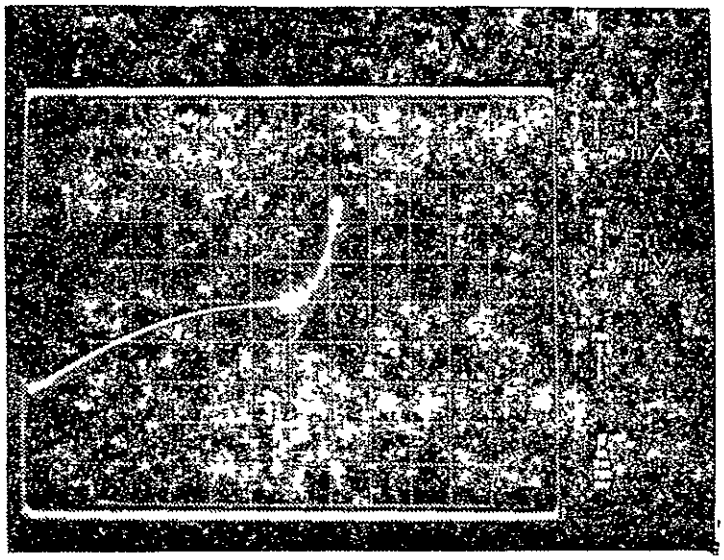

ELEMENT NO. 16

T = 145K

$A_j = 3 \times 5\ mil^2$

d = 20 μm

$R_o = 164$ ohms

$R_o A_j = 0.016$ ohm-cm^2

ORIGINAL PAGE IS
OF POOR QUALITY

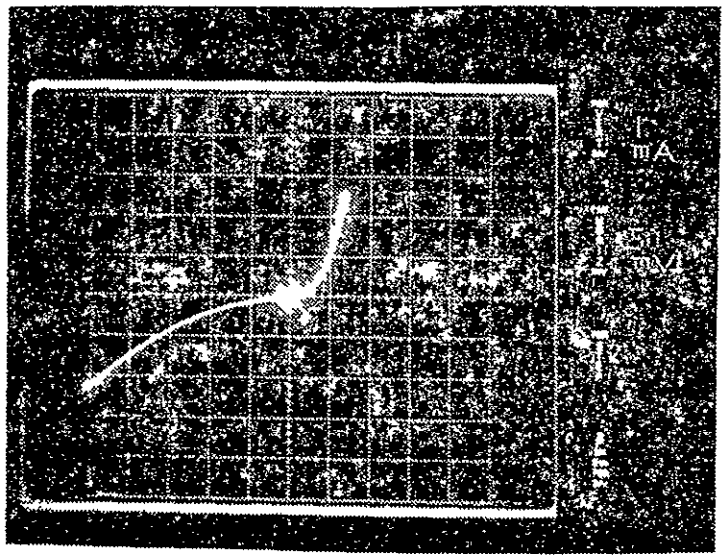

ELEMENT NO. 18

T = 145K

$A_j = 3 \times 5\ mil^2$

d = 14 μm

$R_o = 222$ ohms

$R_o A_j = 0.022$ ohm-cm^2

Figure 5-6 Current-Voltage Characteristics for Two Elements from a Tapered Array Structure (Device # 20574-S190-1A) at 145 K

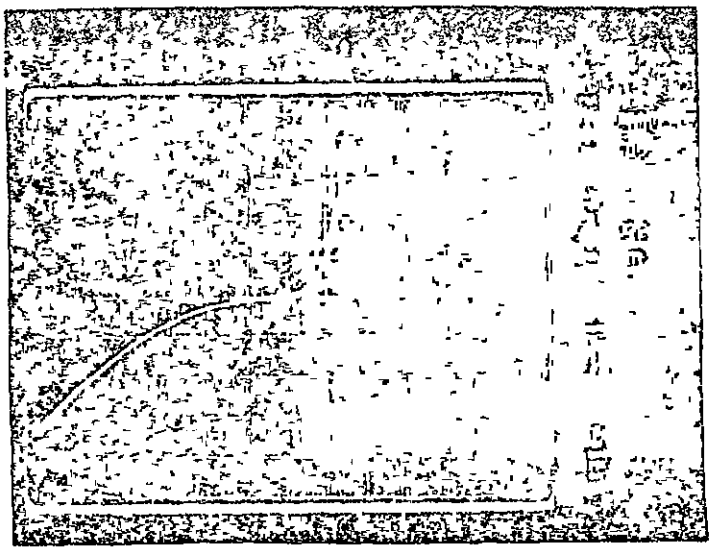

ELEMENT NO. 19

T = 145K

$A_j = 3 \times 5\ mil^2$

d = 11 μm

$R_o = 470$

$R_o A_j = 0.046\ ohm\text{-}cm^2$

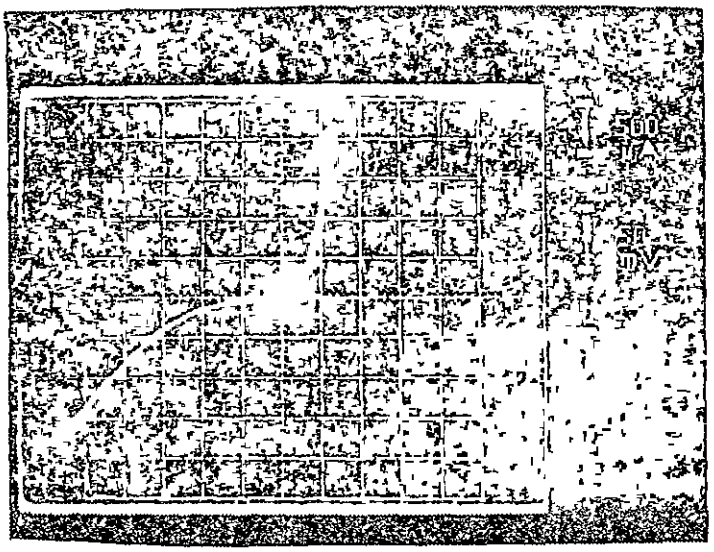

ELEMENT NO. 20

T = 145K

$A_j = 3 \times 5\ mil^2$

d = 14 μm

$R_o = 286$ ohms

$R_o A_j = 0.028\ ohm\text{-}cm^2$

Figure 5-7 Current-Voltage Characteristics for Two Elements from a Tapered Array Structure (Device 20574-S90-1A) at 145 K

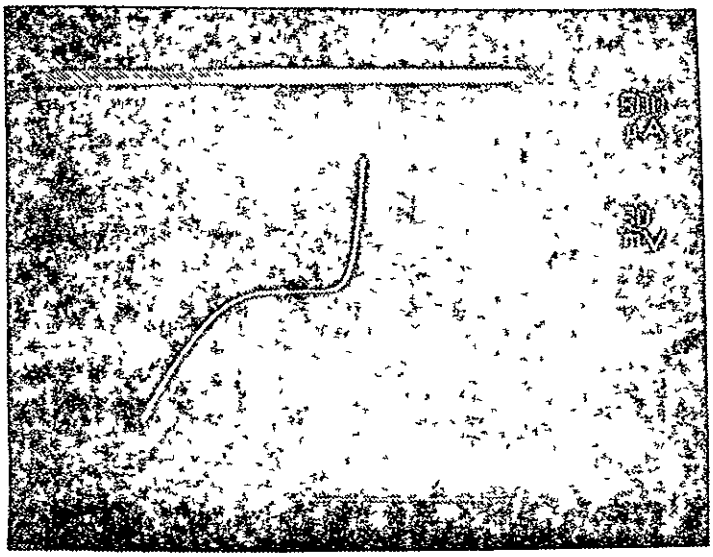

ELEMENT NUMBER 18

T = 77 K

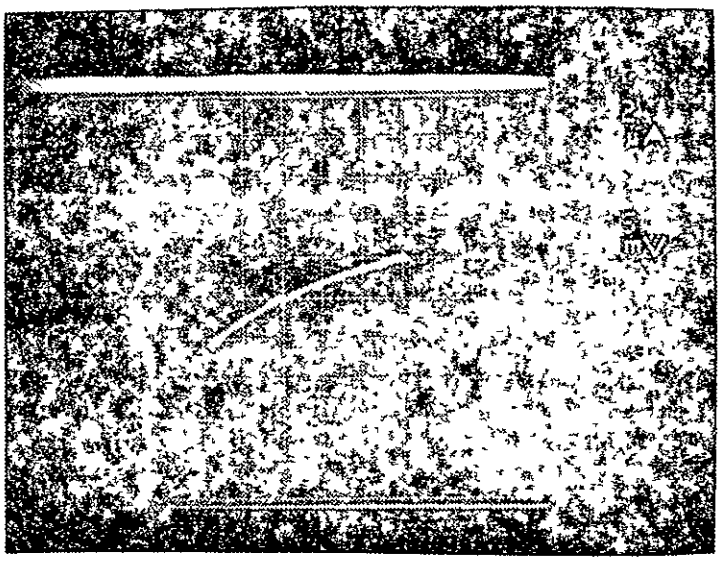

ELEMENT NUMBER 18

T = 77 K

RIGINAL PAGE IS
OF POOR QUALITY

Figure 5-8 I-V Characteristic at 77 K for Element 20 of Array 20574-S90-1A

An "excess" or "leakage" current mechanism shows up in all four elements at low temperatures. It is responsible for the slowly varying R_oA products at temperatures below about 110 – 120 K. The data in Table 5–1 show that the leakage current mechanism appears to be stronger in elements in the damaged region of the array, as indicated by the lower R_oA products at 77 K in these elements.

The "excess" or "leakage" current for Elements 18 and 20 at 77 K is shown in the I–V curves of Figures 5–9 and 5–10. Here it can be seen that the second derivative of current with respect to bias voltage is negative near zero bias voltages. This is in marked contrast to the case for diffusion current, for which the second derivative of current with respect to voltage is positive near zero bias voltage.

Another characteristic associated with the leakage current is an actual decrease in R_oA with decreasing temperature. This can be seen for Elements 18, 20 and 30 in Figures 5–3, 5–4 and 5–5 for temperatures below about 100 K.

A systematic increase in cutoff wavelength (measured at 77 K) with increasing p–region thickness can be seen in the data of Table 5–1. Cutoff wavelength is defined (and measured) as that wavelength at which the spectral responsivity has fallen to 50% of its peak value. This systematic increase is not seen in all tapered arrays studied, and is possibly due to a small gradient in alloy composition.

In summary, the data plotted in Figure 5–1 do show that R_oA at 145 K increases with decreasing p–region thickness. The dependence on p–region thickness d is stronger than expected, being more like d^{-2} or d^{-3} rather than the d^{-1} dependence predicted by Equation 23 of Section 2.2. However, the highest thin-diode R_oA at 145 K (0.046 ohm–cm^2 for Element (9) with $\lambda_{co} \cong 8.0$ μm is still no better than the R_oA products at 145 K for photodiodes with very thick p–regions shown in Figure 5–1 (0.07 ohm–cm^2 for $\lambda_{co} = 8.0$ μm). More investigation of the n^+–p–p^+ photodiode configuration is required to show that it can provide R_oA products higher than those achievable with conventional n^+–p structures.

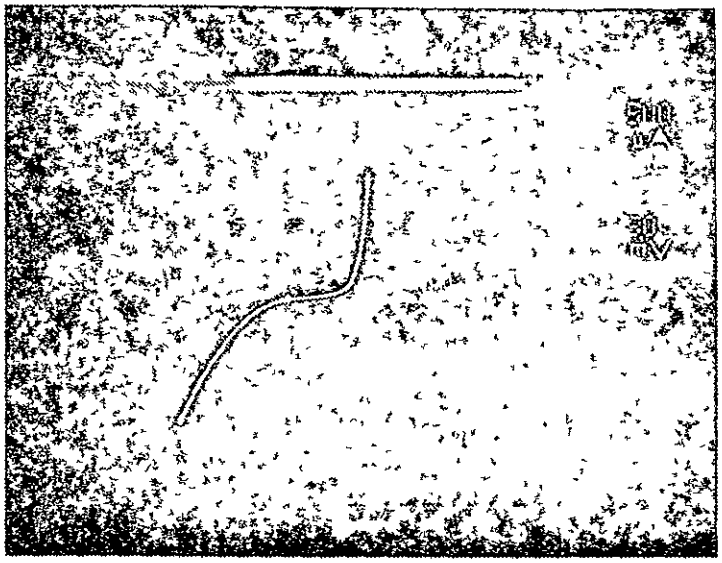

ELEMENT NUMBER 20

T = 77 K

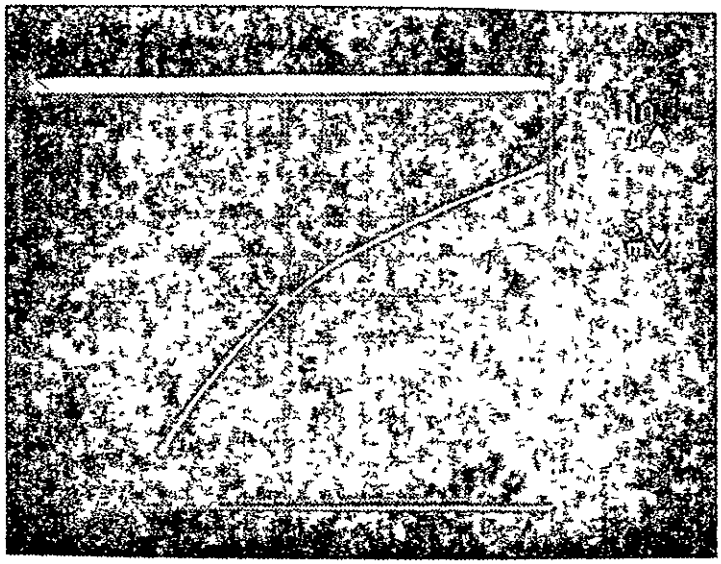

ELEMENT NUMBER 20

T = 77 K

Figure 5-9 I-V Characteristic at 77 K for Element 20 of Array 20574-S90-1A

SECTION 6
SUMMARY AND CONCLUSIONS

Major conclusions arrived at the completion of this program can be summarized as follows:

PHASE I:

a. Investigation of various dopant species such as boron, chlorine, and silicon for fabrication of n^+–p junction structure in p-type $Hg_{0.8}Cd_{0.2}Te$. Results showed that boron and chlorine were suitable implantation species for fabricating n^+ layer in p–$Hg_{0.8}Cd_{0.2}Te$. Boron was selected as the implantation species for array fabrication and activity of boron was found to be strongly dependent on the post-implant anneal time/temperature schedule.

b. Minority carrier lifetime in p–$Hg_{0.8}Cd_{0.2}Te$ was measured using the reverse recovery technique. Electron lifetime in p–$Hg_{0.8}Cd_{0.2}Te$ was found to be limited by mid-gap Shockley-Read type recombination centers. Measured lifetimes were found to be a factor of 3–4 below the band to band radiative recombination limit.

c. Photodiode arrays fabricated during this program were found to be active up to 193 K and R_oA product in these photodiodes was diffusion limited at temperatures above 100 K. Arrays were fabricated meeting the design objectives for an operating temperature of 120 K.

PHASE II:

a. In Phase II of this program, fabrication and characterization of the thin electrically reflecting junction devices (n^+–p–p^+) was carried out. P–p^+ junction was fabricated

using phosphorus implantation in p-$Hg_{0.8}Cd_{0.2}Te$. Activity of the implanted phosphorus was found to be strongly dependent on the anneal time/temperature schedule.

b. Using a n^+-p-p^+ tapered array structure, it was demonstrated that significant increase in R_oA can be accomplished by using a thin electrically reflecting junction. Further work is needed to optimize this structure.

SECTION 7
RECOMMENDATIONS

Further improvements in n^+–p–p^+ $Hg_{0.8}Cd_{0.2}Te$ device structure for high temperature detection applications (i.e. T > 145 K) would require more thorough investigations in the following areas.

a. $Hg_{0.8}Cd_{0.2}Te$ MATERIAL DEVELOPMENT

Work carried out on the device development for n^+–p–p^+ junction photodiode structure has shown that the factor limiting R_oA is the p-side electron lifetime T_e. The p-side lifetimes presently observed are considerably shorter than the radiative limit, and is due to Shockley-Read centers. If the lifetime can be improved to the radiative limit, then considerable improvement in R_oA can be achieved. Finally, if lifetimes near the radiative limit can be obtained, then the electron diffusion length on the p-side is quite long and use of the reflecting backside contact can considerably improve R_oA.

More developmental efforts are needed to determine the nature and origin of Shockley-Read centers in p-$Hg_{0.8}Cd_{0.2}Te$. Techniques such as Deep Level Transient Spectroscopy (DLTS) need to be looked at in determining more accurately the trap concentration, position of these traps in the fundamental absorption gap and their capture cross-section respectively. Understanding of these recombination centers can lead to determining ways and means to either reduce or neutralize the effects of these centers, thereby minority carrier can be improved further for achieving radiative recombination limit.

b. n^+–p–p^+ $Hg_{0.8}Cd_{0.2}Te$ DEVICE OPTIMIZATION

It has been demonstrated experimentally for the first time, using a n^+–p–p^+ tapered array structure, that for high temperature detector operation, reduction of the diffusion current can effectively be achieved (and hence improvement in R_oA) via

reducing thickness of the p–region. Having demonstrated the concept, further work is needed for optimizing the device structure via better understanding of the fabrication procedures using the ion-implantation technology. More work also needs to be done in determination of the residual damage after ion-implantation of n^+–p and p^+–p junctions respectively.

SECTION 8

REFERENCES

1. "Detection of Long Wavelength Infrared at Moderate Temperatures," Final Technical Report, NASA Johnson Space Center Contract NAS9-14180, Mod. 5S, April, 1977.

2. D. Long, T.J. Tredwell and J.R. Woodfill, "Detectivity vs Temperature in Infrared Photon Detectors," Proceedings of the Joint Meeting of the IRIS Specialty Groups on Infrared Detectors and Imaging - Volume 1,13-15 June, 1978, pp. 387-400.

3. D. Long, "Photovoltaic and Photoconductive Infrared Detectors," in Topics in Applied Physics, Volume 19: Optical and Infrared Detectors, pp. 101-147 (Springer-Verlag, Berlin Heidelberg, 1977); the p^+-p backside contact is discussed on pp. 110-112.

4. W. Shockley, "The Theory of P-n Junctions in Semiconductors and p-p Junction Transistors," Bell System Tech. Journal 28, 101 (1949).

5. J.S. Blakemore, "Semiconductor Statistics," Pergamon Press, 1962.

6. M.A. Kinch, M.J. Brau and A. Simmons, "Recombination Mechanisms in 8-14 μm HgCdTe," J. Appl. Phys. 44, 1649 (1973).

7. W. Van Roosbroeck and W. Shockley, "Photon-Radiative Recombination of Electrons and Holes in Germanium," Phys. Rev. 94, 1558 (1954).

8. R.N. Hall, "Recombination Processes in Semiconductors," Proc. Inst. Elec. Engg. B. Suppl. 106, 923 (1959).

9. J.L. Schmit and E.S. Johnson, "Exploratory Development on $Hg_{1-x}Cd_xTe$ Improvement, Phase II," Report AFML-TR-77-21, Air Force Materials Laboratory Final Technical Contract F33615-74-C-5041.

10. E.S. Johnson and J.L. Schmit, "Doping Properties of Selected Impurities in $Hg_{1-x}Cd_xTe$," Jour. Elec. Mat. 6, 25 (1977).

11. C.G. Verbracken, W.M.C. Sansen and R.J. Van Overstraeten, "Impurity profile Determination and D.C. Modeling of the JIGFET," IEEE Trans. of Electron Devices. Vol ED-24, No. 6 723 (1977).

12. A.K. Sood and T.J. Trdwell, "8–14 micrometer Photovoltaic Detectors," Final Technical Report, U.S. Army NVL Contract DAAK70-76-C-0273, March 1979.

13. A.K. Sood and T.J. Tredwell, "High Performance 8–14 m (Hg,Cd)Te Junction Photodiodes for Infrared Imaging Applications, "IEEE International Electron Devices Meeting, Dec. 4–6, 1978, Washington, D.C.

14. J.L. Schmit and E.L. Stelzer, "Temperature and Alloy Compositional Dependence of the Energy Gap of (Hg,Cd)Te," J. Appl. Phys. 40, 4865 (1969).

15. H.J. Kuno, "Analysis and Characterization of p–n Junction Diode Switching," IEEE Trans. of Elect. Dev., ED-11, 8 (1964).

16. R.H. Kinnston, "Switching Time in Junction Diodes and Junction Transistors," Proc. IRE, 42, 829–834, (1954).

17. B. Lax and S.F. Neustader, "Transient Response of a p–n Junction," J. Appl. Phys. 25, 1148 (1954).

18. J.L. Moll, S. Krakauer and R. Shea, "p–n Junction Charge Storage Diodes," Proc. IRE 50 43 (1962).

19. J.L. Moll and S.A. Hamilton, Life Time in p–i–n Diodes," Proc. IEEE 57, 1250 (1969).

20. W. Scott, "Electron Mobility in $Hg_{1-x}Cd_xTe$," J. Appl. Phys. 43, 1055 (1972).

21. E. Igras, J. Piotrowski, I. Zimnoch-Higersberger, "Investigation of Ion Implanted Graded Gap (Hg,Cd)Te Photodiodes," Electron Technology 10, 63 (1977).

22. T. Koehler, "Ion-Implantation of Gold in Mercury Cadmium Telluride," U.S. Patent #4, 003, 759, Jan. 18, 1977.

23. J.F. Gibbons, W.S. Johnson and S.W. Mylerolc, "Projected Range Statistics in Semiconductors and Related Materials," 2nd Edition, JohnWilley and Sons Inc. (1975).

24. A.K. Sood, J.W. Marcinec and M.B. Reine, "8–12 μm $(Hg_{0.8},Cd_{0.2})Te$ Photodiode Arrays for Focal Plane Applications," Final Report, NRL Contract #N00173–78-C–0145 (1979) to be published.

APPENDIX A
TEST RESULTS FOR ARRAY DELIVERED UNDER – PHASE II

1.0 INTRODUCTION

This appendix summarizes the detector performance on the array delivered to NASA/JSC after completion of the phase II of this program. Detailed measurements of R_oA, spectral response, η and D* on ten of the elements were carried out at 77 K and R_oA measurements as a function of temperature were performed on a few elements to determine the dominant current mechanism, which was found to be bulk diffusion limited between 200 to 77 K. This array also met the performance design goals of phase II of this program.

2 0 MEASUREMENT CONDITIONS

2 1 Physical Parameters

Blackbody Temperature (T_{BB})	500 K
Blackbody Aperture (d_A)	0.215 cm
Background Temperature (T_A)	300 K
Stefan-Boltzmann Constant (σ)	$5\ 67X10^{-12}$ W/cm^2 $^oK^4$
Detector to Orifice Distance (d)	15 cm
Chopping Frequency	3000 Hz
Sine to RMS Conversion Factor (C)	0 353
Noise Bandwidth (Δf)	10 Hz
Emissivity, ε Blackbody, Chopper	1 0

2 2 Flux Density (H_{BB}) at Detector

$$H_{BB} = \varepsilon\ \sigma\ (T_{BB}^4 - T_A^4)\ \frac{d_A^2}{4d^2}\ C\ (W/cm^2)$$

$$H_{BB} = (5\ 6X10^{-6})\ W/cm^2$$

2 3 Blackbody Responsivity (R_{BB})

$$R_{BB} = \frac{i_{sig}}{H_{BB} A_d}\ (amp/watt)$$

2 4 Spectral Responsivity ($R\lambda c$)

$$R_{\lambda c} = g\ \ R_{BB}\ (amp/watt)$$

λc = cutoff wavelength

g = spectral conversion factor

2.5 Quantum Efficiency at λ Cutoff

$$\eta\ (\lambda_c) = R_{\lambda_c} \quad (\frac{hc}{q_{\lambda_c}})$$

2.6 Detectivity ($D^*_{\lambda c}$)

$$D^*_{\lambda c} = \frac{R_{\lambda c}\ A_d}{\sqrt{\overline{i_n^2}}}$$

3 0 SUMMARY OF DETECTORS' PERFORMANCE

Element Number	λ_{co} (μm) (77K)	$D^*_{\lambda c}$ (cm $\sqrt{Hz}$/W) Measured (77K)	R_o (Ω) (77K)	$D^*_{\lambda c}$ (cm $\sqrt{Hz}$/W) Calculated from R_o (77K)
1	11 9	$1\ 9X10^{10}$	$1\ 0X10^{3}$	$1.6X10^{11}$
2	11 8	$1\ 9X10^{10}$	$1.7X10^{3}$	$2\ 1X10^{11}$
3	11 8	$2\ 0X10^{10}$	$1.9X10^{3}$	$2\ 3X10^{11}$
4	11 6	$2\ 0X10^{10}$	$1\ 9X10^{3}$	$2.2X10^{11}$
5	11 5	$2\ 0X10^{10}$	$2.0X10^{3}$	$2.3X10^{11}$
6	11 3	$1\ 9X10^{10}$	$2.3X10^{3}$	$2\ 4X10^{11}$
7	10.9	$1.7X10^{10}$	$1.7X10^{3}$	$1.9X10^{11}$
8	(11.5)*	$2\ 1X10^{10}$	$2\ 1X10^{3}$	$2.3X10^{11}$
9	11.7	$1.9X10^{10}$	$1\ 9X10^{3}$	$2.1X10^{11}$
10	11 9	$1\ 9X10^{10}$	$1\ 3X10^{3}$	$1\ 8X10^{11}$
11	12 0	$1\ 9X10^{10}$	$0.96X10^{3}$	$1\ 5X10^{11}$

TABLE I

$D^*_{\lambda c}$ FOR 20474 S-129 Ba, ELEMENTS 1 THROUGH 11 THE CALCULATED VALUES ASSUME A QUANTUM EFFICIENCY η=0 8 DETECTOR TEMPERATURE = 77K
D* MEASURED AT 3KHz CHOPPING FREQUENCY

* Assumed λ_c

Element Number	λ_c (um) (145K)	R_o (Ω) (145K)	Area (cm^2)	$D^*_{\lambda c}$ (cm $\sqrt{Hz}$/W) Calculated from R_o (145K)
1	10 0	12.2	$1.8X10^{-3}$	$8.0X10^{9}$
2	9 9	11 1	$1 9X10^{-3}$	$7 8X10^{9}$
3	9.9	11 4	$1 9X10^{-3}$	$7 9X10^{9}$
4	9 8	12 2	$1.9X10^{-3}$	$8.1X10^{9}$
5	9 7	15 6	$2 0X10^{-3}$	$9.3X10^{9}$
6	9 6	17 2	$2.0X10^{-3}$	$9.6X10^{9}$
7	9 3	13.5	$1.8X10^{-3}$	$7.8X10^{9}$
8	(9.7)*	15 6	$1.9X10^{-3}$	$9.0X10^{9}$
9	9 8	13.0	$1.9X10^{-3}$	$8.3X10^{9}$
10	10 0	13 9	$1 9X10^{-3}$	$8 8X10^{9}$
11	10 0	13.2	$1.8X10^{-3}$	$8 3X10^{9}$

TABLE III

$D^*_{\lambda c}$ FOR 20474 S-129 Ba, ELEMENTS 1 THROUGH 11, CALCULATED FROM R_o VALUES, ASSUMING A QUANTUM EFFICIENCY η=0 6 DETECTOR TEMPERATURE = 145K

* Assumed λ_c

Element Number	λ_{co} (um) (120K)	R_o (Ω) (120K)	Area (cm^2)	$D^*_{\lambda c}$ (cm $\sqrt{Hz}$/W) Calculated from R_o (120K)
6	10.1	37	$2.0X10^{-3}$	$1\ 6X10^{10}$
7	9 8	49	$1\ 8X10^{-3}$	$1\ 7X10^{10}$
11	10 7	21	$1.8X10^{-3}$	$1\ 2X10^{10}$

TABLE II

$D^*_{\lambda c}$ FOR 20474 S-129 Ba, ELEMENTS 6, 7, AND 11, CALCULATED FROM R_o VALUES, ASSUMING A QUANTUM EFFICIENCY η=0 6 DETECTOR TEMPERATURE = 120K

4 0 DETECTOR TEST RESULTS

4.1 Spectral Cutoff Data

Contained in this section are the curves of the relative photo-response versus wavelength of elements 20474 S-129 Ba - 3, 7, 9

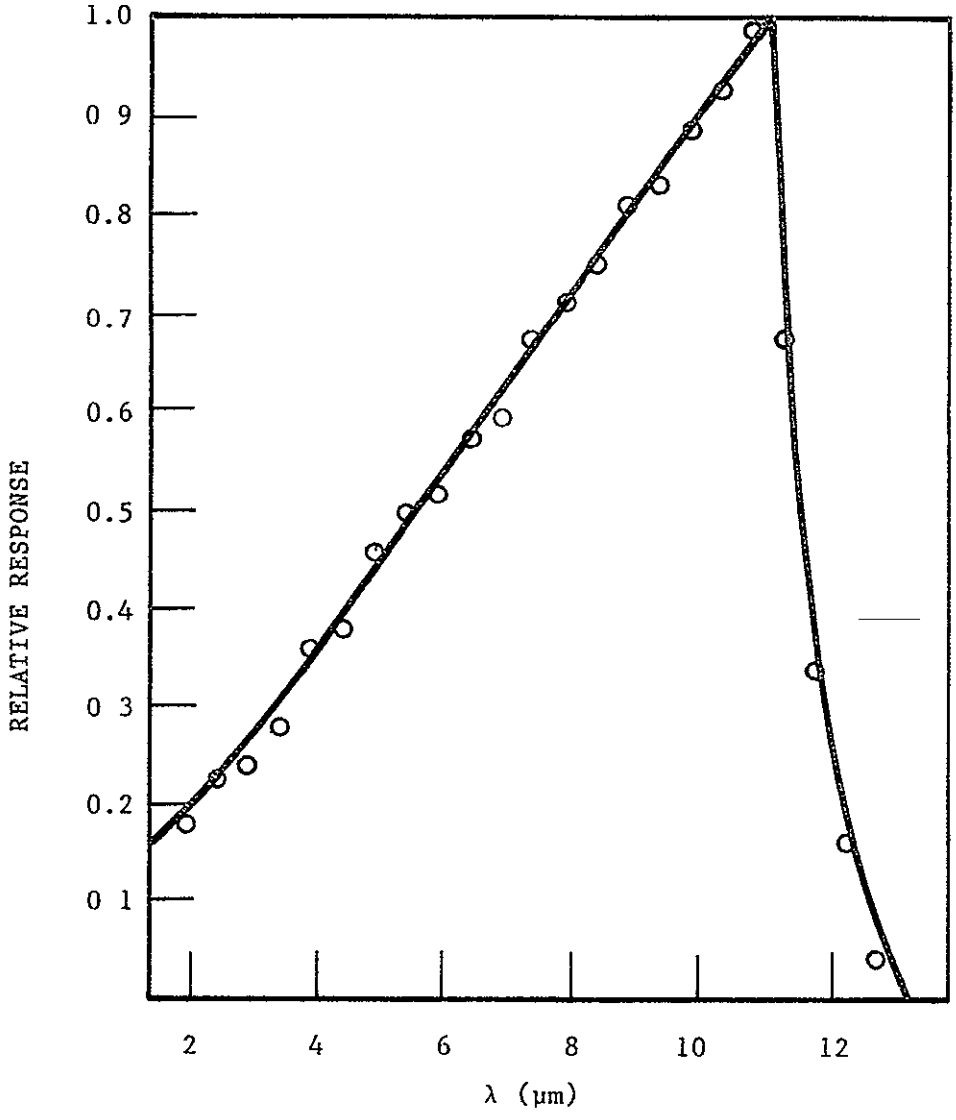

FIGURE 2 RELATIVE SPECTRAL RESPONSE FOR 20474 S-129 Ba, ELEMENT #3 DETECTOR TEMPERATURE = 77K

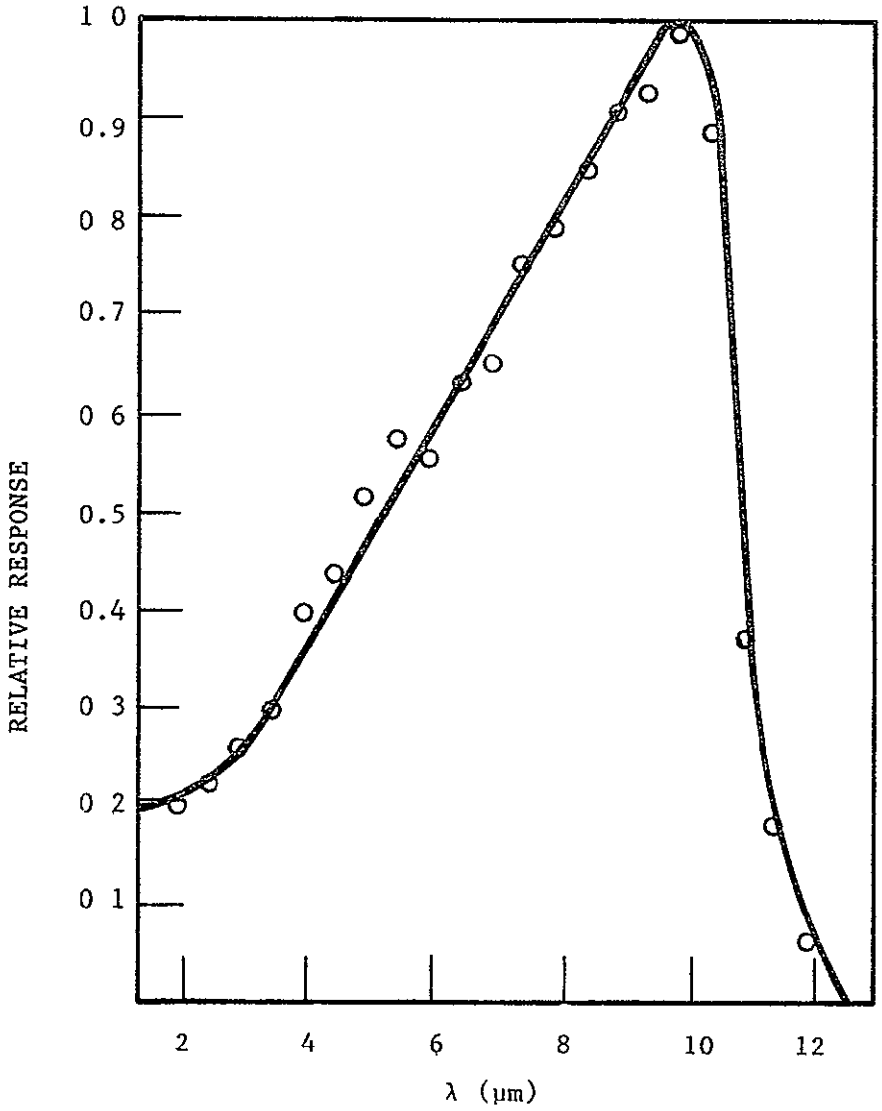

FIGURE 3 RELATIVE SPECTRAL RESPONSE FOR 20474 S-129 Ba, ELEMENT #7 DETECTOR TEMPERATURE = 77K

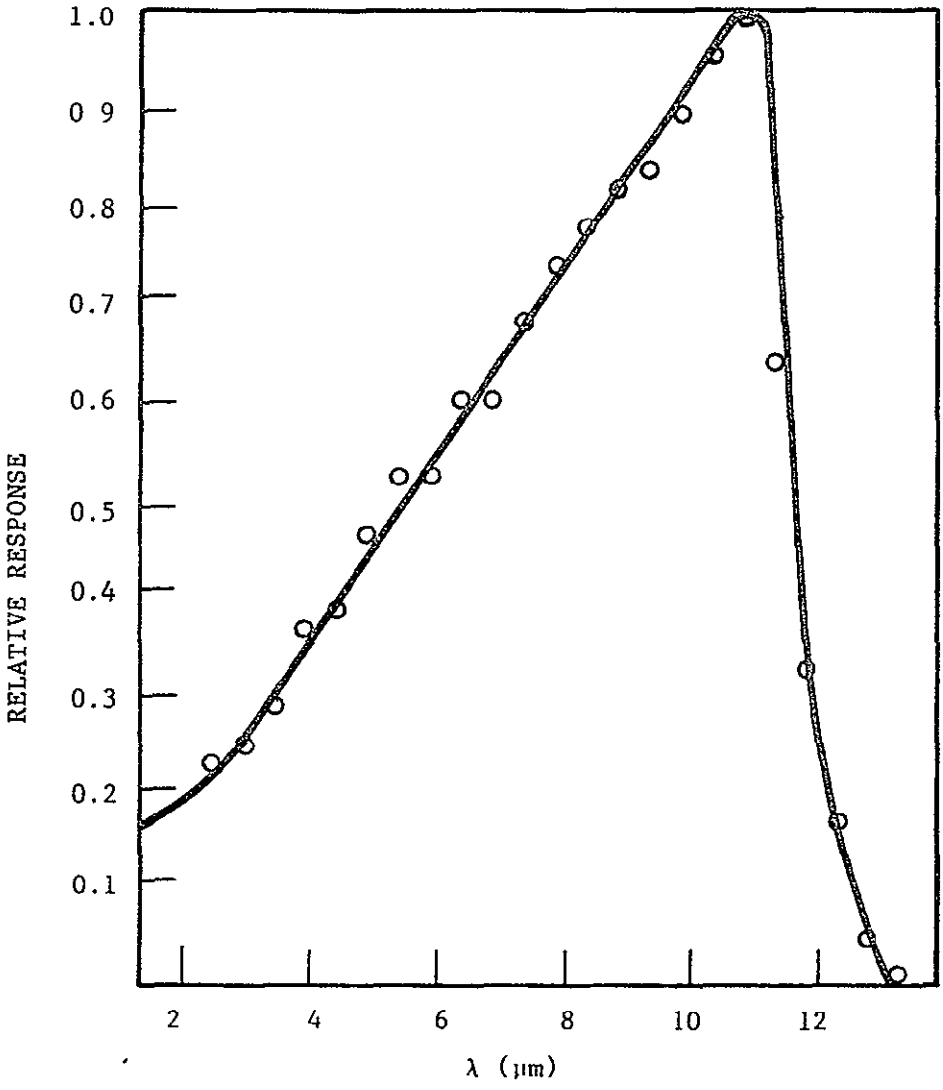

FIGURE 4 RELATIVE SPECTRAL RESPONSE FOR 20474 S-129 Ba, ELEMENT #9 DETECTOR TEMPERATURE = 77K

4 2 Spot Scan

Contained in this section are spot scans of elements 20474 S-129 Ba - 3, 7

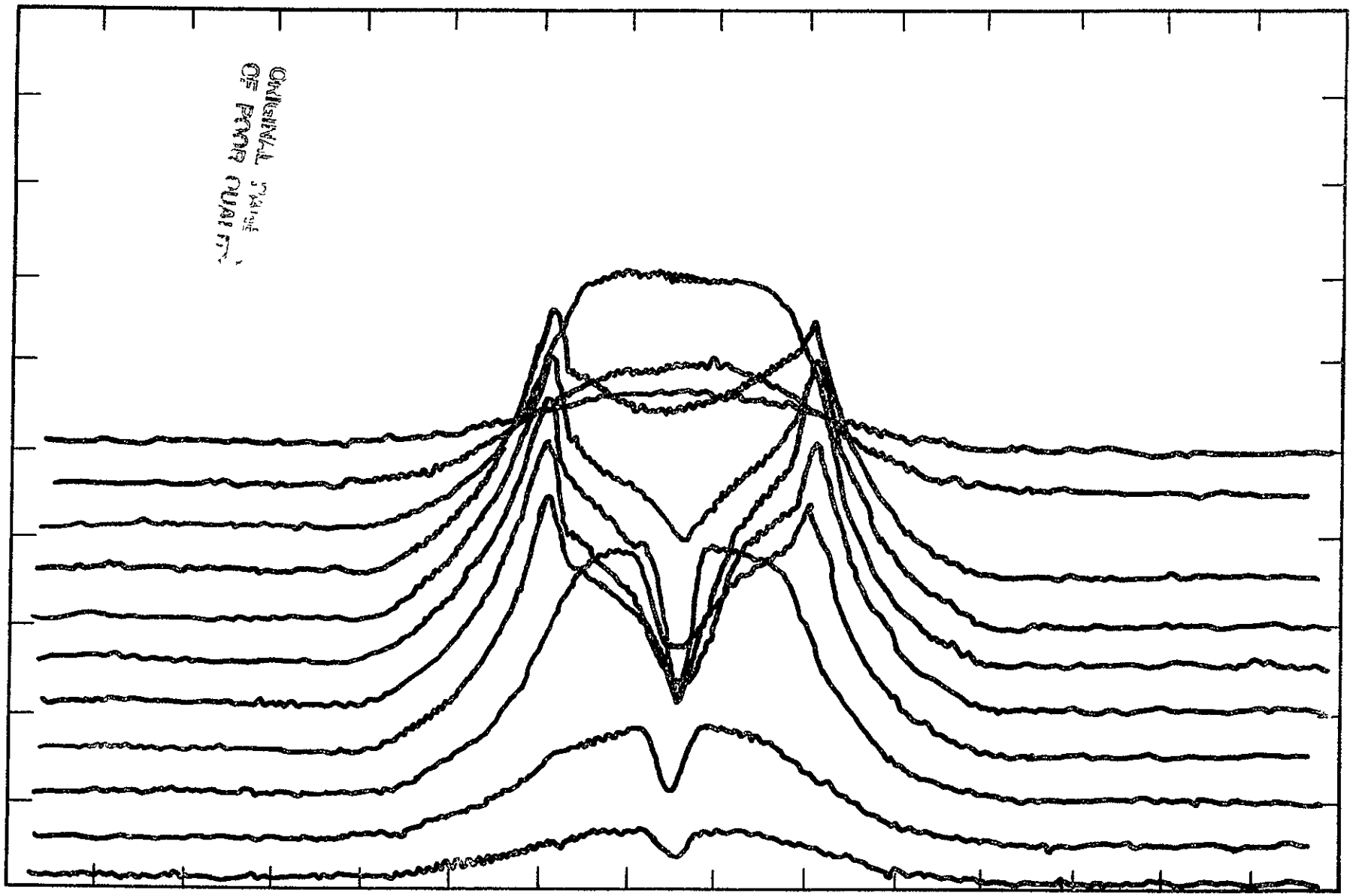

FIGURE 5 SPOT SCAN OF 20474 S-129 Ba, ELEMENT #3
DETECTOR TEMPERATURE = 77K

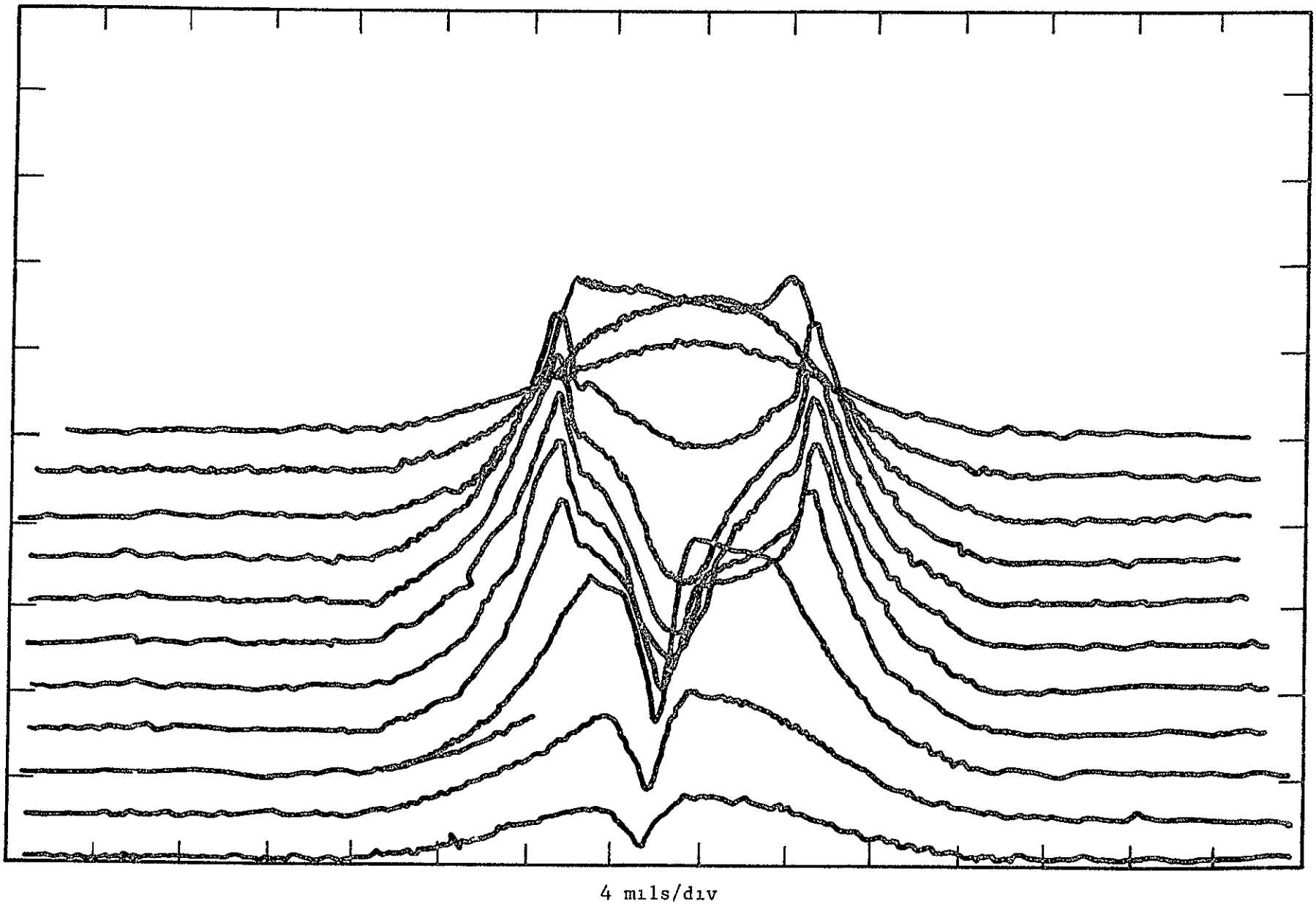

FIGURE 6 SPOT SCAN OF 20474 S-129 Ba, ELEMENT #7
DETECTOR TEMPERATURE = 77K

4 3 Detector Performance

Contained in this section are the detailed data concerning the elements contained on 20474 S-129 Ba. These data were taken at a detector temperature T_d = 77K. In obtaining these data, a distance from the germanium window of the dewar to the surface of the detector of approximately 1 7 cm was used

Test Performance (77K)

Element #	20474 S-129 Ba-1
Area (cm^2)	$1.76X10^{-3}$
R_o (Ω)	$1.02X10^{3}$
Spectral Cutoff (λ_c) (um)	11.9
g factor	2.174
Responsivity ($R\lambda$) (amp/watt)	7.04
Noise (i_n) (amp/$\sqrt{Hz}$)	$1.58X10^{-11}$
D*λ (λ_c, 3 KHz, 1 Hz)	$1.9X10^{10}$

ORIGINAL PAGE IS
OF POOR QUALITY

FIGURE 7 I-V CHARACTERISTICS OF 20474 S-129 Ba, ELEMENT #1, AT T = 77K

Test Performance (77K)

Element #	20474 S-129 Ba-2
Area (cm^2)	1.87×10^{-3}
R_o (Ω)	1.72×10^{3}
Spectral Cutoff (λc) (μm)	11.8
g factor	2.241
Responsivity ($R\lambda$) (amp/watt)	7.06
Noise (i_n) (amp/$\sqrt{Hz}$)	1.58×10^{-11}
$D^*\lambda$ (λc, 3 KHz, 1 Hz)	1.9×10^{10}

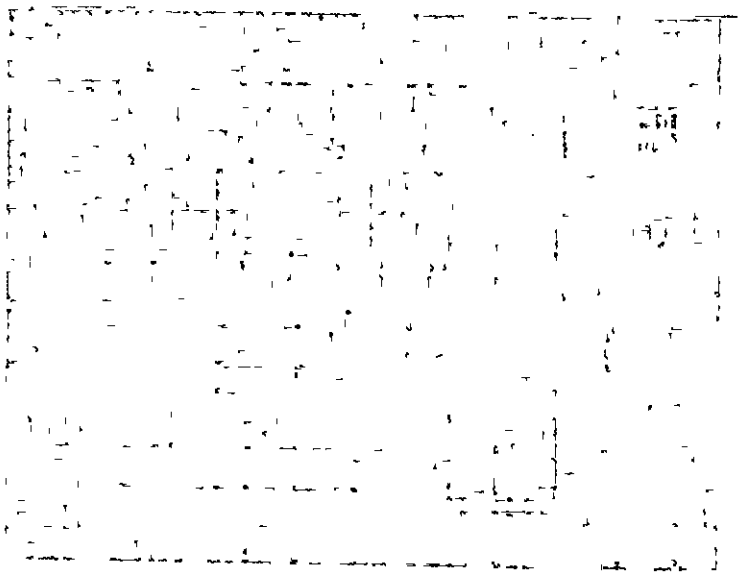

FIGURE 8 I-V CHARACTERISTICS OF 20474 S-129 Ba, ELEMENT #2, AT T = 77K

Test Performance (77K)

Element #	20474 S-129 Ba-3
Area (cm^2)	$1.87X10^{-3}$
R_o (Ω)	$1.92X10^{3}$
Spectral Cutoff (λc) (μm)	11 8
g factor	2 192
Responsivity ($R\lambda$) (amp/watt)	7 1
Noise (i_n) (amp/$\sqrt{Hz}$)	$1.58X10^{-11}$
D*λ (λc, 3 KHz, 1 Hz)	$2\ 0X10^{10}$

ORIGINAL PAGE IS
OF POOR QUALITY

FIGURE 9 I-V CHARACTERISTICS OF 20474 S-129 Ba, ELEMENT #3, AT T = 77K

C-2

Test Performance (77K)

Element #	20474 S-129 Ba-4
Area (cm^2)	$1\ 93X10^{-3}$
R_o (Ω)	$1\ 85X10^{3}$
Spectral Cutoff (λc) (μm)	11 6
g factor	2 182
Responsivity ($R\lambda$) (amp/watt)	7.1
Noise (i_n) (amp/ $\sqrt{Hz}$)	$1\ 58X10^{-11}$
$D^*\lambda$ (λc, 3 KHz, 1 Hz)	$2X10^{10}$

FIGURE 10 I-V CHARACTERISTICS OF 20474 S-129 Ba, ELEMENT #4, AT T = 77K

Test Performance (77K)

Element #	20474 S-129 Ba-5
Area (cm^2)	$2X10^{-3}$
R_o (Ω)	$2X10^{3}$
Spectral Cutoff (λc) (μm)	11.5
g factor	2 145
Responsivity ($R\lambda$) (amp/watt)	7 1
Noise (i_n) (amp/ $\sqrt{Hz}$)	$1\ 58X10^{-11}$
D*λ (λc, 3 KHz, 1 Hz)	$2X10^{10}$

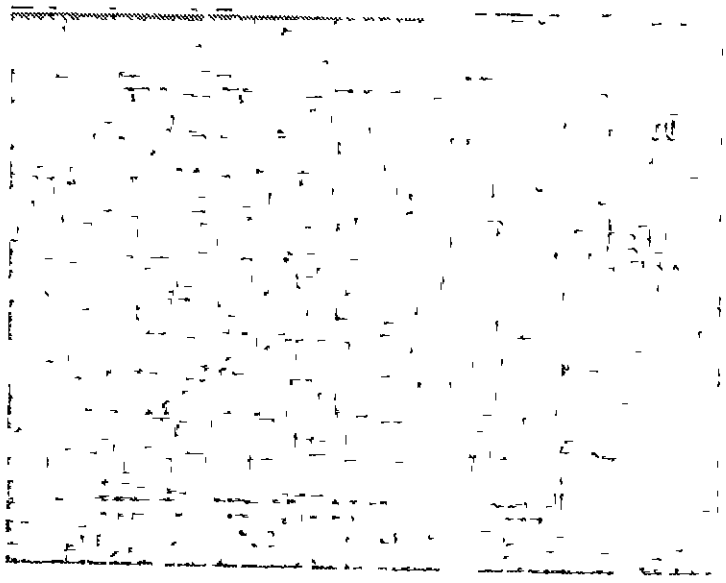

FIGURE 11 I-V CHARACTERISTICS OF 20474 S-129 Ba, ELEMENT #5, AT T = 77K

Test Performance (77K)

Element #	20474 S-129 Ba-6
Area (cm^2)	$2X10^{-3}$
R_o (Ω)	$2\ 3X10^{3}$
Spectral Cutoff (λc) (μm)	11.3
g factor	2.268
Responsivity (Rλ) (amp/watt)	6.8
Noise (i_n) (amp/ $\sqrt{Hz}$)	$1\ 58X10^{-11}$
D*λ (λc, 3 KHz, 1 Hz)	$2X10^{10}$

ORIGINAL PAGE IS
OF POOR QUALITY

FIGURE 12 I-V CHARACTERISTICS OF 20474 S-129 Ba, ELEMENT #6, AT T = 77K

Test Performance (77K)

Element #	20474 S-129 Ba-7
Area (cm^2)	$1.8X10^{-3}$
R_o (Ω)	$1.7X10^{3}$
Spectral Cutoff (λc) (μm)	10.9
g factor	2 173
Responsivity ($R\lambda$) (amp/watt)	6.4
Noise (i_n) (amp/ $\sqrt{Hz}$)	$1.58X10^{-11}$
$D^*\lambda$ (λc, 3 KHz, 1 Hz)	$1.7X10^{10}$

FIGURE 13 I-V CHARACTERISTICS OF 20474 S-129 Ba, ELEMENT #7, AT T = 77K

Test Performance (77K)

Element #	20474 S-129 Ba-8
Area (cm^2)	$1.88X10^{-3}$
R_o (Ω)	$2.1X10^{3}$
Spectral Cutoff (λc) (μm)	11 3
g factor	2.15
Responsivity ($R\lambda$) (amp/watt)	7 56
Noise (i_n) (amp/ $\sqrt{Hz}$)	$1\ 58X10^{-11}$
D*λ (λ_c, 3 KHz, 1 Hz)	$2\ 1X10^{10}$

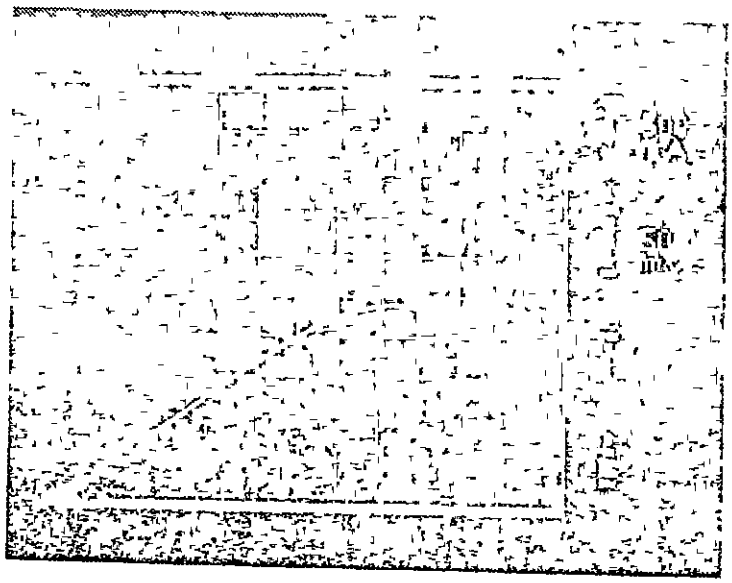

FIGURE 14 I-V CHARACTERISTICS OF 20474 S-129 Ba, ELEMENT #8, AT T = 77K

Test Performance (77K)

Element #	20474 S-129 Ba-9
Area (cm^2)	$1\ 9X10^{-3}$
R_o (Ω)	$1.9X10^{3}$
Spectral Cutoff (λc) (μm)	11 7
g factor	2 173
Responsivity ($R\lambda$) (amp/watt)	7 1
Noise ($\imath_n$) (amp/ $\sqrt{Hz}$)	$1\ 58X10^{-11}$
D*λ (λe, 3 KHz, 1 Hz)	$1\ 9X10^{10}$

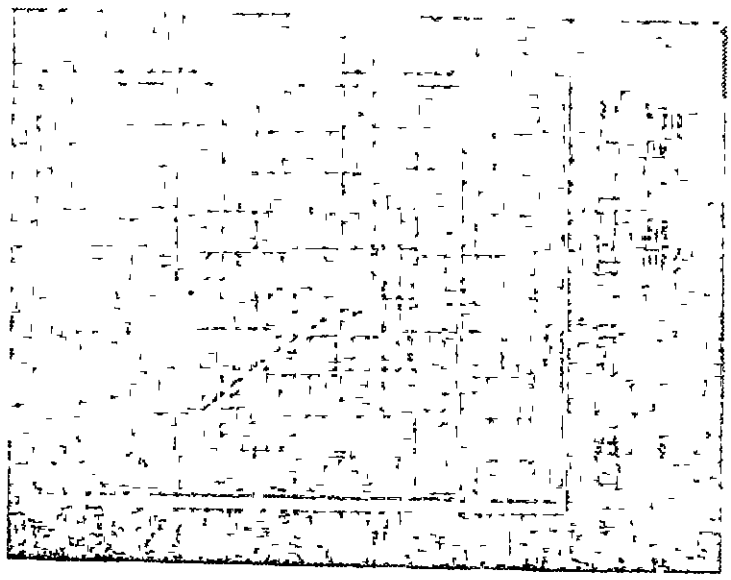

RIGINAL PAGE IS
OF POOR QUALITY

FIGURE 15 I-V CHARACTERISTICS OF 20474 S-129 Ba, ELEMENT #9, AT T = 77K

Test Performance (77K)

Element #	20474 S-129 Ba-10
Area (cm^2)	1.9×10^{-3}
R_o (Ω)	1.3×10^{3}
Spectral Cutoff (λc) (μm)	11.9
g factor	2.166
Responsivity ($R\lambda$) (amp/watt)	7.1
Noise (i_n) (amp/$\sqrt{Hz}$)	1.58×10^{-11}
$D^*\lambda$ (λc, 3 KHz, 1 Hz)	1.9×10^{10}

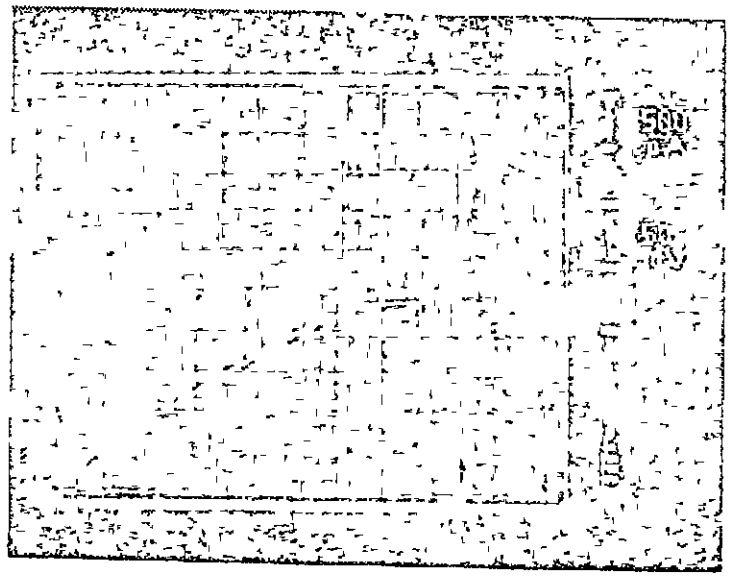

FIGURE 16 I-V CHARACTERISTICS OF 20474 S-129 Ba, ELEMENT #10, AT T = 77K

Test Performance (77K)

Element #	20474 S-129 Ba-11
Area (cm^2)	$1.8X10^{-3}$
R_o (Ω)	962
Spectral Cutoff (λc) - (μm)	12
g factor	2.14
Responsivity ($R\lambda$) (amp/watt)	7.1
Noise (i_n) (amp/ $\sqrt{Hz}$)	$1.58X10^{-11}$
D*λ (λc, 3 KHz, 1 Hz)	$1.9X10^{10}$

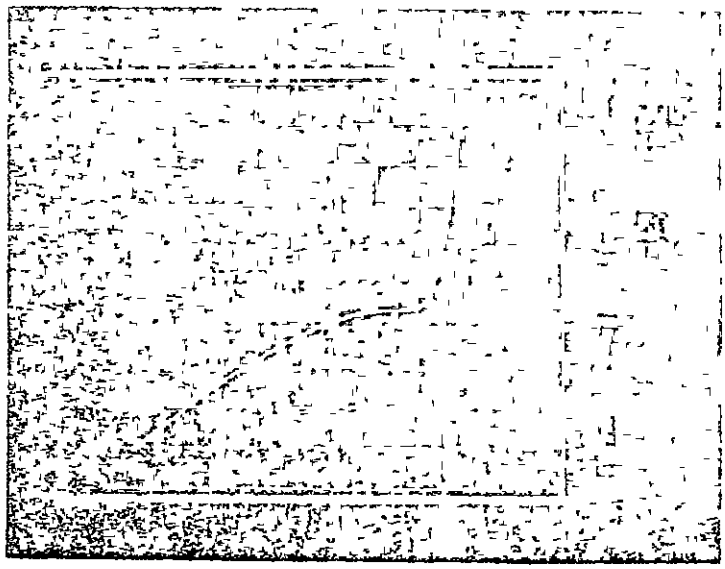

FIGURE 17 I-V CHARACTERISTICS OF 20474 Ba, ELEMENT #11, AT T = 77K

4 4 R_oA Vs T

Contained in this section are the data of R_oA versus Temperature of Elements 20474 S-129 Ba-6, 7, 11.

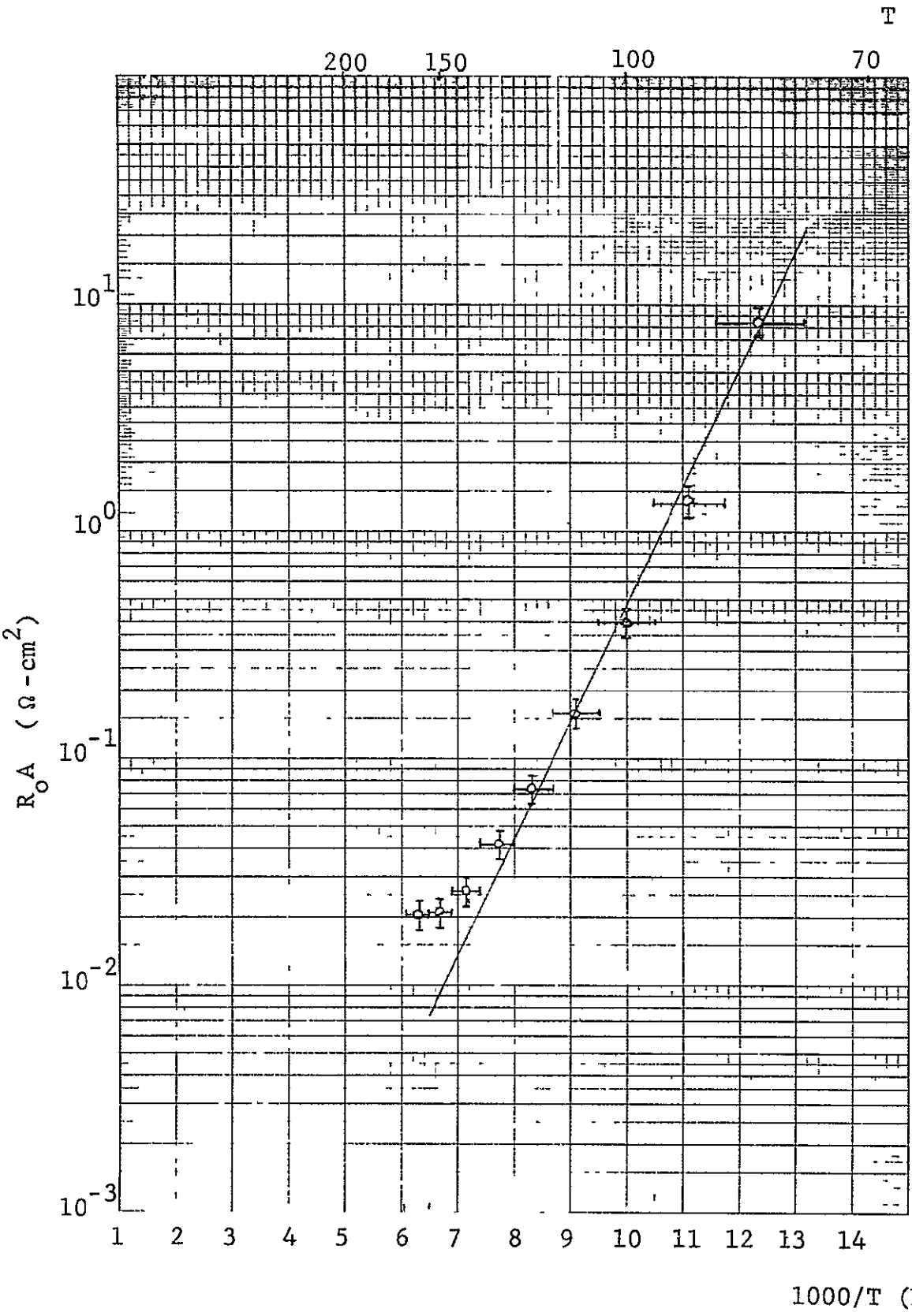

FIGURE 18 R_oA Versus Temperature for 20474 S-129 Ba, Element #6

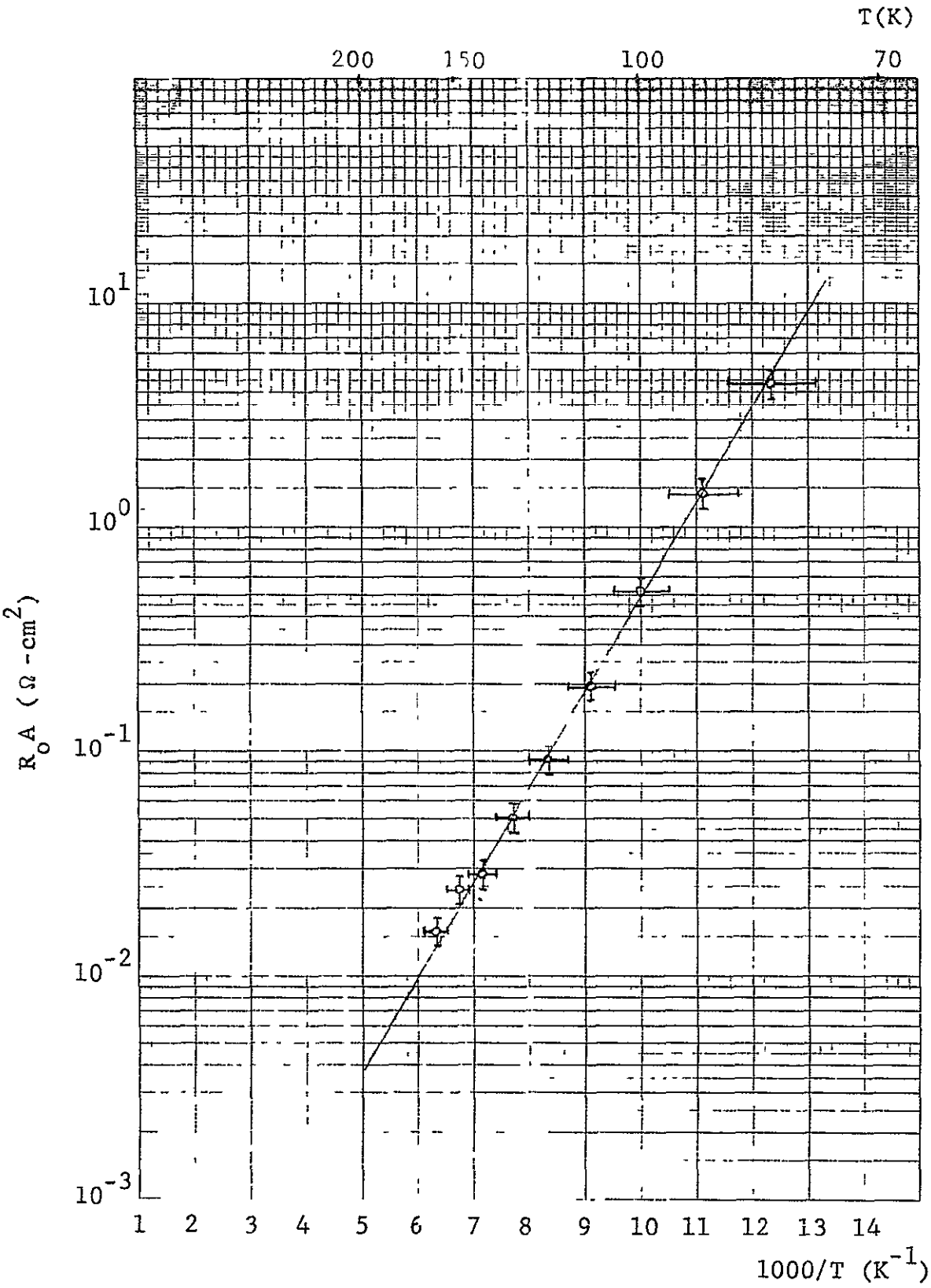

FIGURE 19 R_oA Versus Temperature for 20474 S-129 Ba, Element #7

ORIGINAL PAGE IS
OF POOR QUALITY

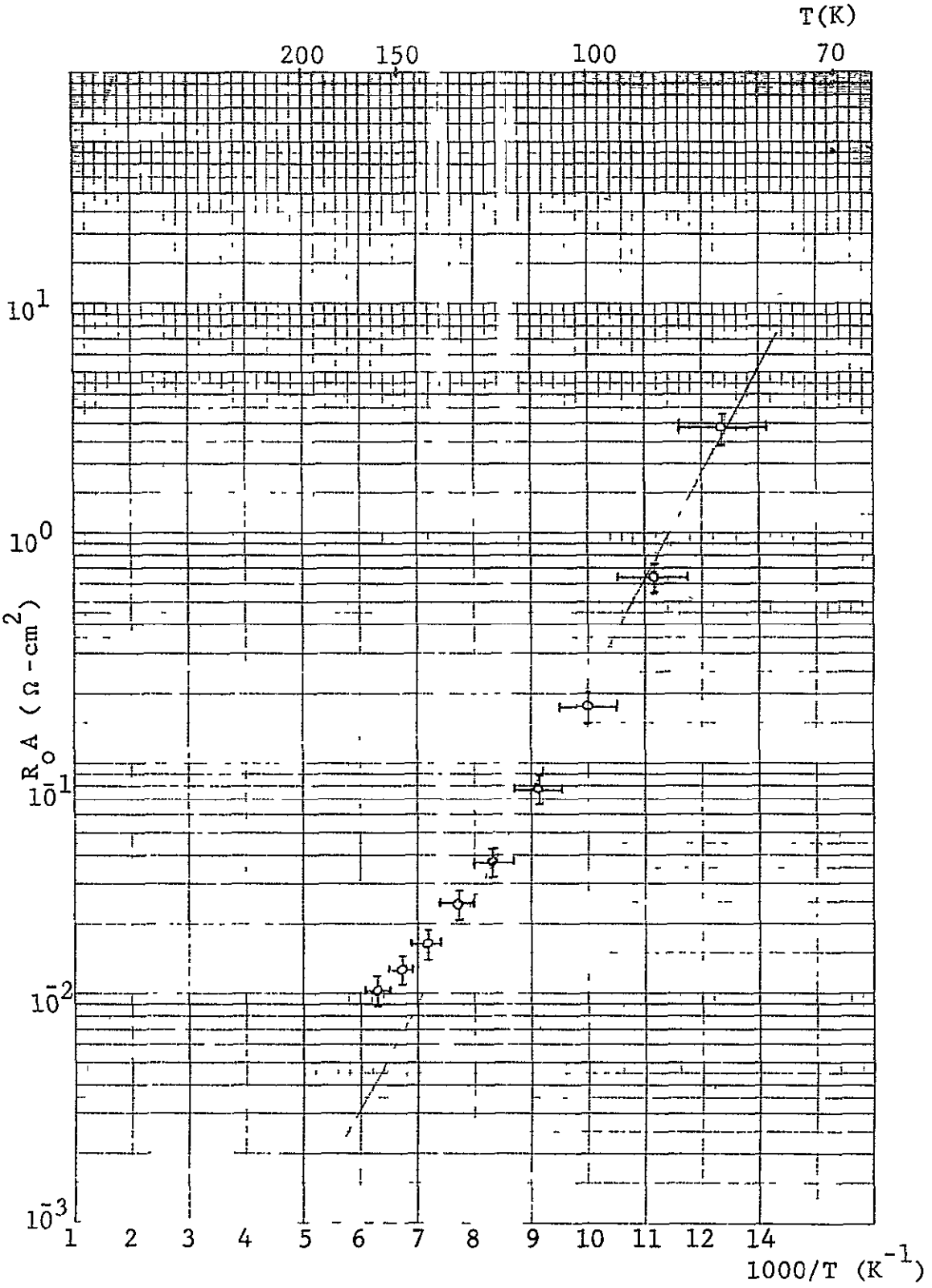

FIGURE 20 $R_o A$ Versus Temperature for 20474 S-129 Ba, Element #11

5 0 APPENDIX

The implant area for the devices is 6 45X10^{-4} cm^2 (10 X 10 mil^2) This, however, is not the active area of the device Collection of photo-generated charge can occur from a diffusion length of the minority carriers around the device This causes an active area greater than the implanted area This effect can be seen very easily on the spot scans. The active area boundaries are taken to be the 50% intensity points, and show diode areas greater than 10 X 10 mil^2 (Figures 5 and 6).

Even when using this larger area, an interesting effect is occurring, the quantum efficiency (η) is greater than unity The quantum efficiency is given by

$$\eta = R_{\lambda c} \quad \frac{hc}{q\lambda c}$$

where

h = 6.624 X 10^{-34} J-sec
c = 3 X 10^{10} cm/sec
q = 1 6 X 10^{-19} coul
$\lambda c \equiv$ diode cutoff wavelength (μm)

$$R_{\lambda c} = \frac{i_{sig}}{d_{BB} A_d} \cdot g \text{ (amp/watt)}$$

i_{sig} = measured signal current (amp)
d_{BB} = blackbody flux density (watt/cm^2)
A_d = detector area (cm^2)
g = blackbody spectral conversion factor

Since h, c, and q are physical constants and λp, i_{sig}, d_{BB}, and g can be easily measured or calculated, the device area would most likely account for the large quantum efficiencies However, even when the spot scan areas are used to compute the device efficiency, the value of η is greater than unity This problem arose after mounting the device in the deliverable dewar Previous data taken in October 1977 indicated values of $\eta \approx 0$ 8, with the diode area corrected for diffusion length effects These data were taken while the device was mounted in a test vehicle

The present data were taken while the device was mounted in the deliverable dewar (Cryogenic Associates IR-14) The cold finger pedestal area of this dewar is covered with crinkled metal foil It is quite possible that this foil is reflecting the incident radiation in such a way as to increase the amount of radiation incident on the surface of the detector. This would then give an apparent increase in the device efficiency

The device areas in this report were arrived at by taking the measured signal and computing the device area assuming the previously obtained value of $\eta = 0.8$ (10/77, test vehicle)

Only partial data was taken for 20474 S-129 Ba, Element #8 Therefore, to compute a value for $D^*_{\lambda c}$, a cutoff wavelength $\lambda c = 11.5\mu m$, spectral conversion factor g = 2 15 and device area $A = 1.9X10^{-3}$ cm^2 were assumed

The $D^*_{\lambda c}$ data for T = 120K and 145K recorded in Tables II and III were calculated from R_o values measured at those temperatures The values of λc were computed from the material's x-value (in $Hg_{1-x}Cd_xTe$). This x-value was obtained from the measured λc (T = 77K). The formula used for these x-value calculations is.

$$Eg = 1.59_x - 0.25 + 5.233\ (10^{-4})\ T\ (1-2.08\ x) + 0.327\ x^3$$

Here

Eg = energy gap in electron volts
T = temperature in Kelvins

The wavelength in microns can then be determined by using the relations

$$\lambda c = Eg/1\ 24$$

A quantum efficiency $\eta = 0\ 6$ was used in calculating the D* values for T = 120K and 145K This was chosen because one would expect the quantum efficiency to decrease as the temperature is raised from the liquid nitrogen temperature.

jes

APPENDIX B
TEST RESULTS FOR ARRAY DELIVERED UNDER – PHASE III

1.0 INTRODUCTION

The performance of the detector array delivered to NASA/JSC on completion of phase III of this program is summarized in this appendix. This array was fabricated in the n^+–p–p^+ interface was obtained by ion-implantation of phosphorus in p–$hg_{0.8}Cd_{0.2}Te$. This array was characterized in detail for R_oA, spot scan, spectral response, quantum efficiency and D* at 80 and 145 K. Performance obtained in this array was found to be a factor of three below the design goal of phase III at 145 K.

2.0 MEASUREMENT CONDITIONS

2.1 Physical Parameters

Blackbody Temperature (T_{BB})	500 K
Blackbody Aperture (d_A)	0.127 cm
Background Temperature (T_A)	300 K
Stefan-Boltzmann Constant (σ)	5.67×10^{-12} W/cm^2 °K^4
Detector to Orifice Distance (d)	15 cm
Chopping Frequency	1000 Hz
Sine to RMS Conversion Factor (C)	0.415
Noise Bandwidth (Δf)	1.0 Hz
Emissivity, ε: Blackbody, Chopper	1.0

2.2 Flux Density (H_{BB}) at Detector

$$H_{BB} = \varepsilon \sigma (T_{BB}^4 - T_A^4) \frac{d_A^2}{4d^2} \cdot C \ (W/cm^2)$$

$$H_{BB} = (2.3 \times 10^{-6}) \ W/cm^2$$

2.3 Blackbody Responsivity (R_{BB})

$$R_{BB} = \frac{i_{sig}}{H_{BB} A_d} \ (amp/watt)$$

2.4 Spectral Responsivity ($R\lambda_c$)

$$R\lambda_c = g \cdot R_{BB} \ (amp/watt)$$

λc = cutoff wavelength

g = spectral conversion factor

2.5 Quantum Efficiency at λ_o Cutoff

$$\eta\ (\lambda_c) = R_{\lambda_c} \cdot \left(\frac{hc}{q\lambda_c}\right)$$

2.6 Detectivity ($D^*_{\lambda_c}$)

$$D^*_{\lambda_c} = \frac{R_{\lambda_c}\sqrt{A_d}}{\sqrt{\overline{i_n^2}}}$$

2.7 Input Circuit Configuration

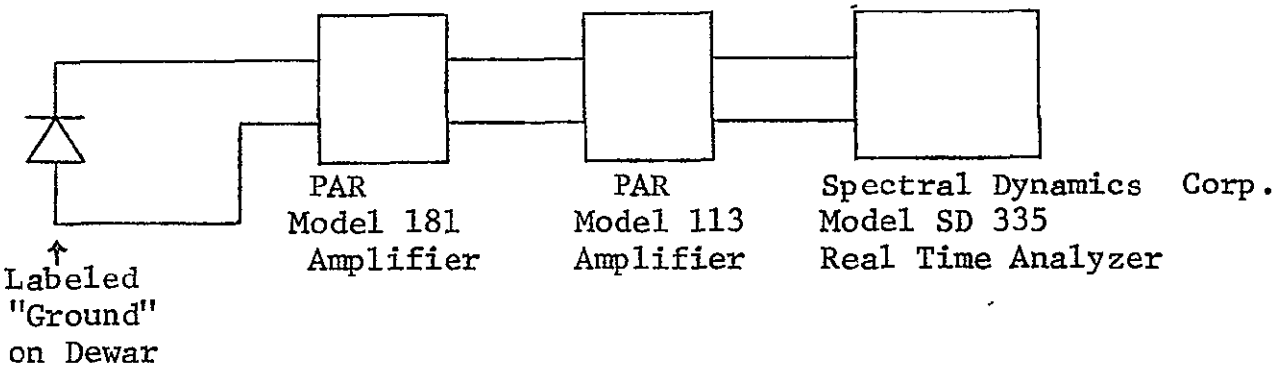

All measurements carried out at zero bias.

3.0 Summary of Detectors' Performance (T=80K)

Array 30578 SO-27 P4 #2 $\lambda_c(77K) \cong 11.4\mu m$

Noise measured at 1 KHz, 1Hz bandwidth

$A_j = 9.7 \times 10^{-5} cm^2$, $A_{opt} = 5.8 \times 10^{-5} cm^2$

Element Number	R_oA_j (Ω-cm^2)	Quantum Efficiency (η)	$D^*_{\lambda c}$ (cm$\sqrt{}$/Hz/w) Measured (80K)	$D^*_{\lambda c}$ (cm$\sqrt{}$/Hz/w) Calculated from R_oA_{opt}(80K)
1	0.64	0.44	1.6×10^{10}	3.8×10^{10}
2	0.70	0.44	1.8×10^{10}	3.9×10^{10}
3	0.29	0.51	1.3×10^{10}	3.0×10^{10}
4	0.76	0.42	1.8×10^{10}	3.9×10^{10}
5	0.74	0.44	1.8×10^{10}	4.0×10^{10}

Table I: Summary of Detectors' Performance at T = 80K. Differences in measured and calculated D* values due to additional noise in experimental apparatus above theoretical noise (i.e. $i_n = \sqrt{4KT/R_o}$).

Summary of Detectors' Performance (T = 145K)

Array 30578 SO-27 P4 #2 λ_c(145K) $\cong$ 9.7μm
$A_j = 9.7 \times 10^{-5} cm^2$, $A_{opt} = 5.8 \times 10^{-5} cm^2$

Element Number	R_oA_j (Ω-cm2)	$D^*_{\lambda c}$ (cm/Hz/w) Calculated from R_oA_{opt} +
1	4.6×10^{-3}	2.4×10^{9}
2	5.1×10^{-3}	2.5×10^{9}
3	5.0×10^{-3}	2.8×10^{9}
4	5.5×10^{-3}	2.5×10^{9}
5	5.1×10^{-3}	2.5×10^{9}

Table II

+ Calculated values using signal (80K), R_oA_{opt} (145K).

4.0 DETECTOR TEST RESULTS

4.1 Detailed Test Data, T = 80K

Test Performance (80K)

Element #	30578 SO-27 P4 #2 el#1
Area (cm^2)	5.8×10^{-5}
R_o (Ω)	6.6×10^{3}
Spectral Cutoff (λ_c) (μm)	11.4
g factor	1.7
Responsivity (R_i) (amp/watt)	4.0
Noise (i_n) (amp/$\sqrt{Hz}$)	1.9×10^{-12}
$D^*_{\lambda_c}$ (λ_c, 1 KHz, 1 Hz)	1.6×10^{10}

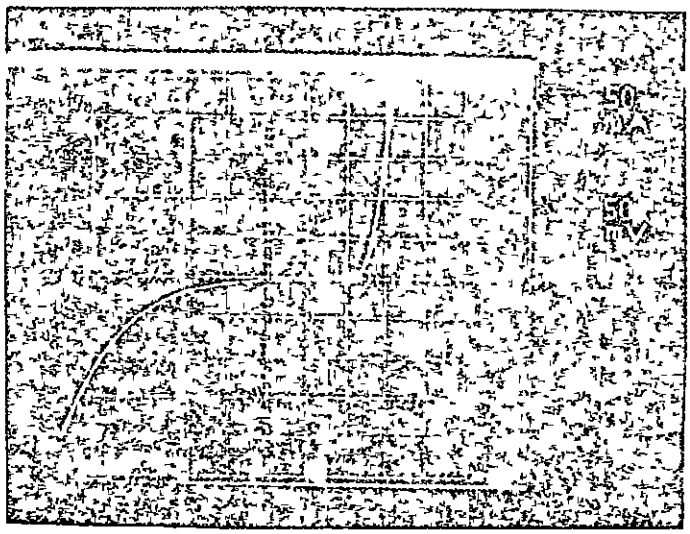

Figure 2: IV Characteristics of 30578 SO-27 P4 #2 element #1 at T = 80K

ORIGINAL PAGE IS OF POOR QUALITY

Test Performance (80K)

Element #	30578 SO-27 P4 #2el#2
Area (cm^2)	5.8×10^{-5}
R_o (Ω)	7.1×10^{3}
Spectral Cutoff (λ_c) (μm)	11.4
g factor	1.7
Responsivity (R_λ) (amp/watt)	4.0
Noise (i_n) (amp/$\sqrt{Hz}$)	1.7×10^{-12}
$D^*_{\lambda_c}$ (λ_c, 1 KHz, 1 Hz)	1.8×10^{10}

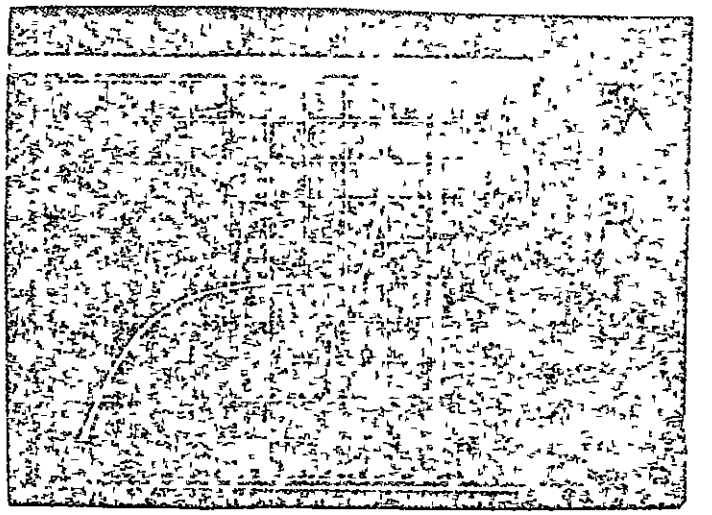

Figure 3: IV Characteristics of 30578 SO-27 P4 #2 element #2 at T = 80K

ORIGINAL PAGE IS
OF POOR QUALITY

Test Performance (80K)

Element #	30578 SO-27 P4 #2 el#3
Area (cm^2)	5.8×10^{-5}
R_o (Ω)	3.0×10^{3}
Spectral Cutoff (λ_c) (μm)	11.4
g factor	1.7
Responsivity (R_λ) (amp/watt)	4.7
Noise (j_n) ($amp/\sqrt{Hz}$)	2.8×10^{-12}
$D^*_{\lambda_c}$ (λ_c, 1 KHz, 1 Hz)	1.3×10^{10}

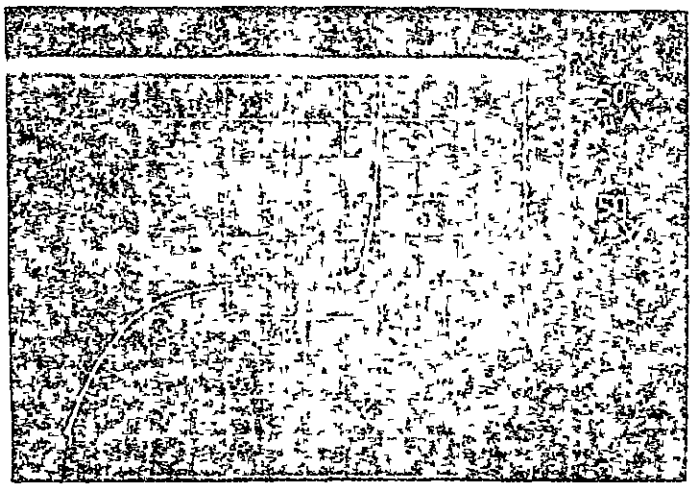

Figure 4: IV Characteristics of 30578 SO-27 P4 #2 element #3 at T = 80K

Test Performance (80K)

Element	30578 SO-27 P4 #2 el#4
Area (cm^2)	5.8×10^{-5}
R_O (Ω)	7.8×10^{3}
Spectral Cutoff (λ_c) (μm)	11.4
g factor	1.7
Responsivity ($R\lambda$) (amp/watt)	3.8
Noise (i_n) (amp/$\sqrt{Hz}$)	1.6×10^{-12}
$D^*\lambda_c$ (λ_c, 1 KHz, 1 Hz)	1.8×10^{10}

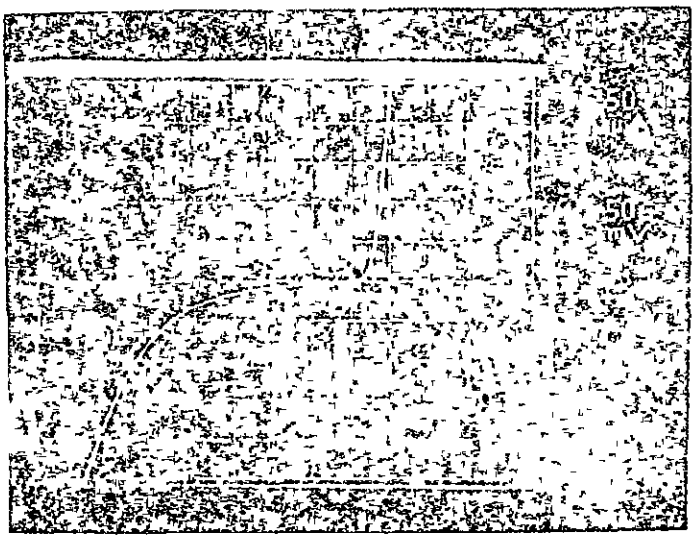

Figure 5: IV Characteristics of 30578 SO-27 P4 #2 element #4 at T = 80K

Test Performance (80K)

Element	30578 SO-27 P4 #2 el#5
Area (cm^2)	5.8×10^{-5}
R_o (Ω)	7.6×10^{3}
Spectral Cutoff (λ_c) (μm)	11.4
g factor	1.7
Responsivity (R_λ) (amp/watt)	4.0
Noise (i_n) (amp/$\sqrt{Hz}$)	1.7×10^{-12}
$D^*_{\lambda_c}$ (λ_c, 1 KHz, 1 Hz)	1.8×10^{10}

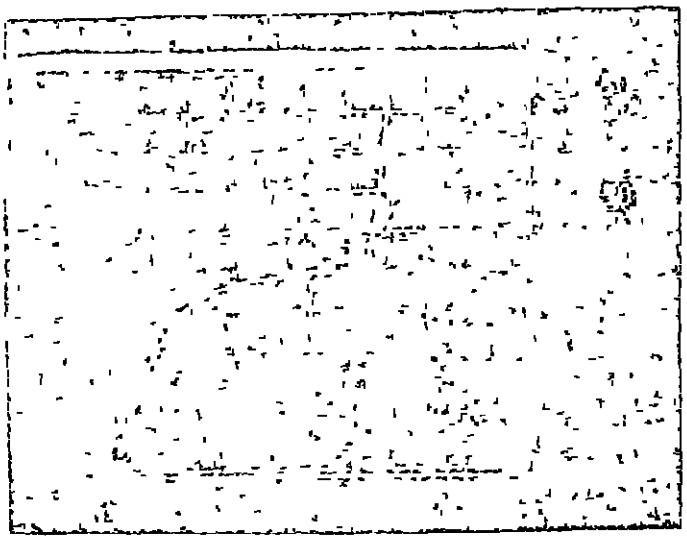

Figure 6: IV Characteristics of 30578 SO-27 P4 #2 element #5 at T = 80K

4.2 Detailed Test Data, T = 145K

Test Performance (145K)

Element	30578 SO-27 P4 #2 el#1
Area (cm^2)	5.8×10^{-5}
R_o (Ω)	47
Spectral Cutoff (λ_c) (μm)	9.6
g factor*	1.7
Responsivity (R_λ) (amp/watt)*	4.0
Noise (i_n) (amp/$\sqrt{Hz}$)+	1.3×10^{-11}
$D^*_{\lambda_c}$ (λ_c, 1 KHz, 1 Hz)	2.3×10^{9}

*Assumed
+Calculated

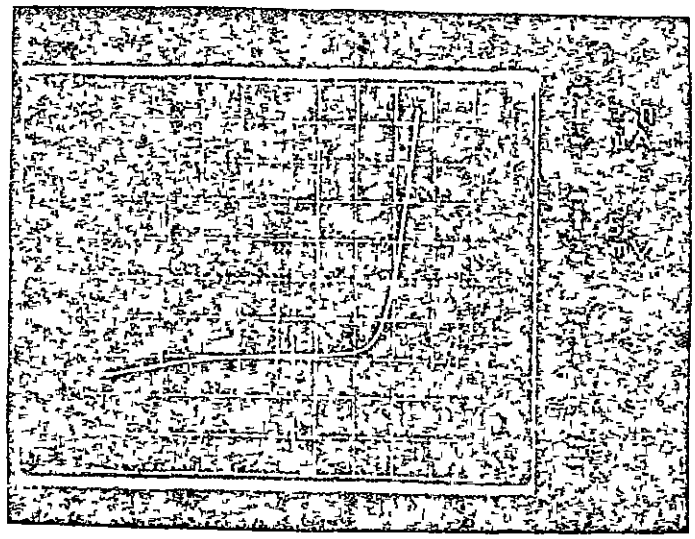

Figure 7. IV Characteristics of 30578 SO-27 P4 #2 element #1 at T = 145K

Test Performance (145K)

Element	30578 SO-27 P4 #2 el#2
Area (cm^2)	5.8×10^{-5}
R_O (Ω)	53
Spectral Cutoff (λ_c) (μm)	9.6
g factor*	1.7
Responsivity (R_γ) (amp/watt)*	4.0
Noise (i_n) ($amp/\sqrt{Hz}$)+	1.2×10^{-11}
$D^*_{\gamma_c}$ (λ_c, 1 KHz, 1 Hz)	2.5×10^{9}

*Assumed
+Calculated

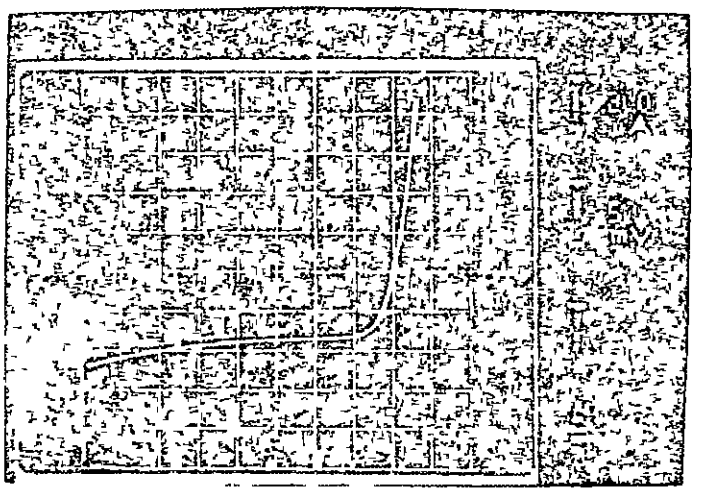

Figure 8: IV Characteristics of 30578 SO-27 P4 #2 element #2 at T = 145K

Test Performance (145K)

Element #	30578 SO-27 P4#2 el#3
Area (cm^2)	5.8×10^{-5}
R_o (Ω)	51
Spectral Cutoff (λ_c) (μm)	9.6
g factor*	1.7
Responsivity (R_λ) (amp/watt)*	4.7
Noise (i_n) (amp/$\sqrt{Hz}$)+	1.3×10^{-11}
$D^*_{\lambda_c}$ (λ_c, 1 KHz, 1 Hz)	2.8×10^{9}

*Assumed

+Calculated

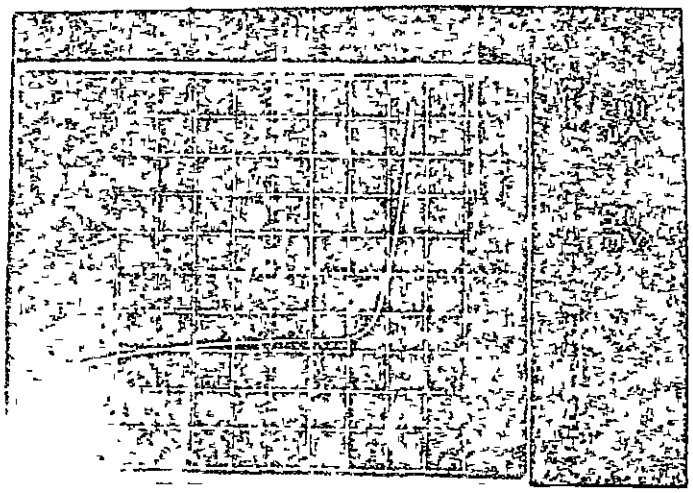

Figure 9: IV Characteristics of 30578 SO-27 P4 #2 element #3 at T = 145K

Test Performance (145K)

Element	30578 SO-27 P4 #2 el#4
Area (cm^2)	5.8×10^{-5}
R_o (Ω)	57
Spectral Cutoff (λ_c) (μm)	9.6
g factor*	1.7
Responsivity (R_λ) (amp/watt)*	3.8
Noise (i_n) (amp/$\sqrt{Hz}$)+	1.2×10^{-11}
$D^*_{\lambda_c}$ (λ_c, 1 KHz, 1 Hz)	2.4×10^{9}

*Assumed

+Calculated

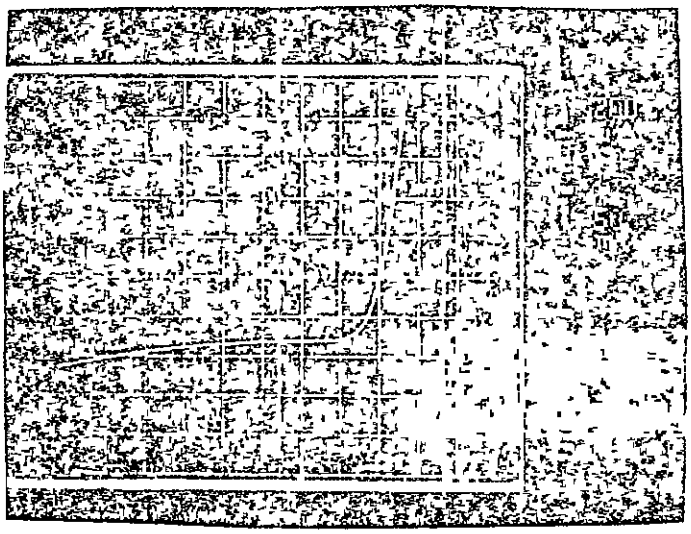

Figure 10: IV Characteristics of 30578 SO-27 P4 #2 element #4 at T = 145K

ORIGINAL PAGE IS
OF POOR QUALITY

Test Performance (145K)

Element #	30578 SO-27 P4 #2 el#5
Area (cm^2)	5.8×10^{-5}
R_o (Ω)	53
Spectral Cutoff (λ_c) (μm)	9.6
g factor*	1.7
Responsivity (R_λ) (amp/watt)*	4.0
Noise (i_n) (amp/$\sqrt{Hz}$)+	1.2×10^{-11}
$D^*_{\lambda_c}$ (λ_c, 1 KHz, 1 Hz)	2.5×10^{9}

*Assumed
+Calculated

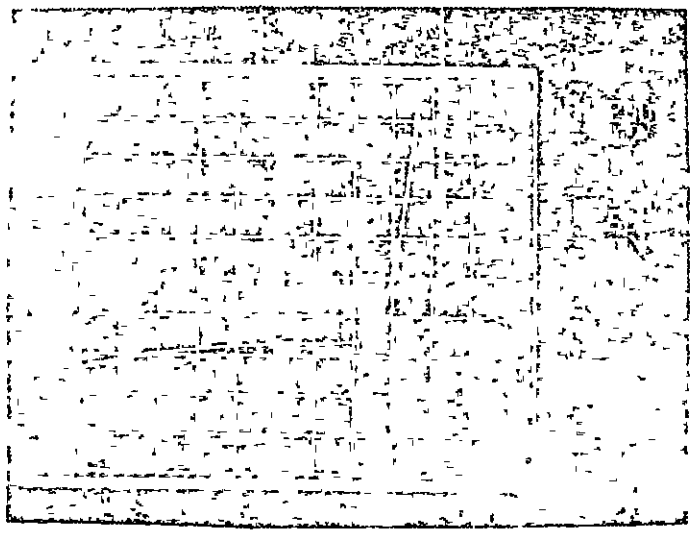

Figure 11: IV Characteristics of 30578 SO-27 P4 #2 element #5 at T = 145K

4.3 R_oA vs. Temperature Data

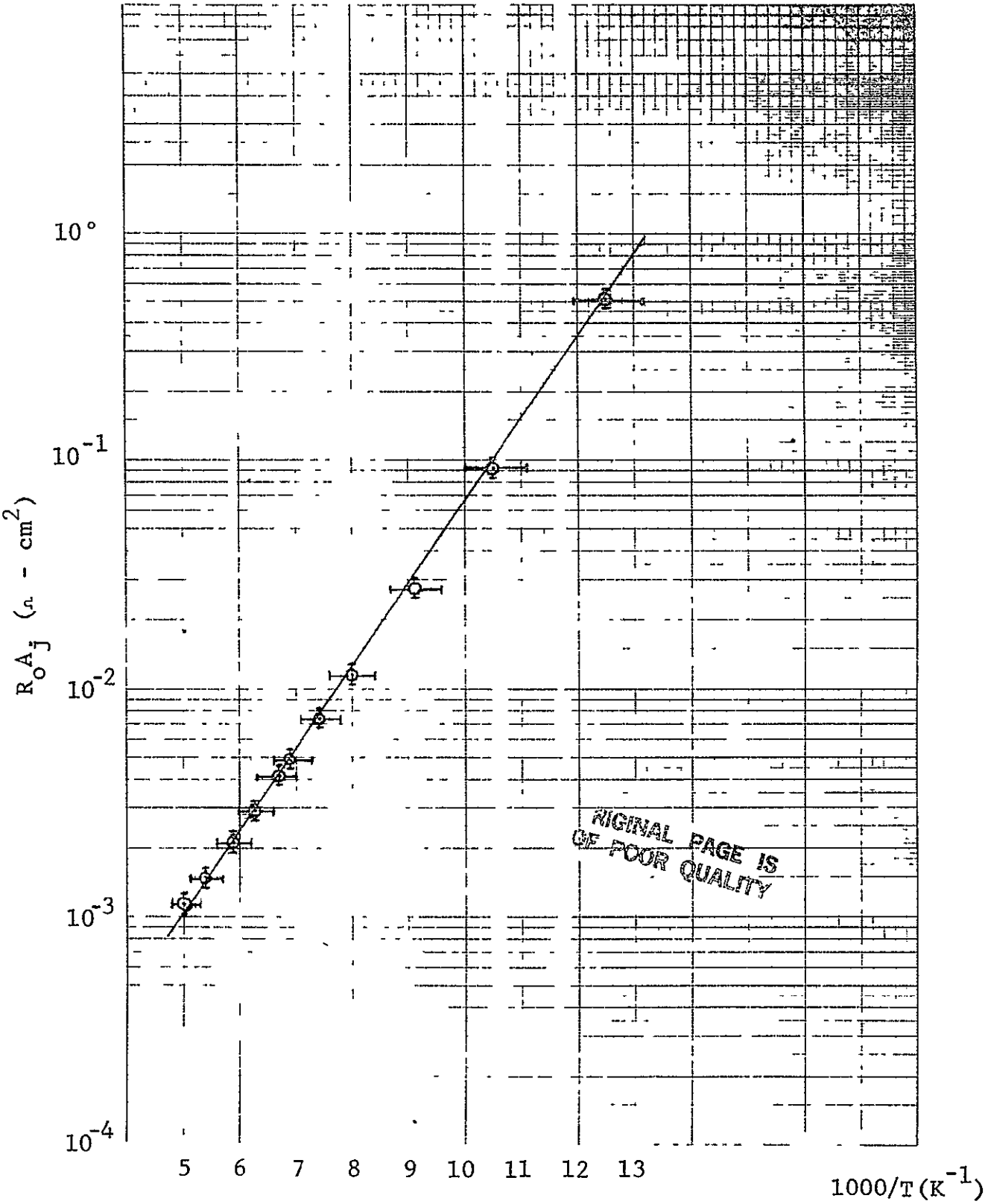

Figure 12: $R_o A$ vs. Temperature for 30578 SO-27 P4 #2, element #1.

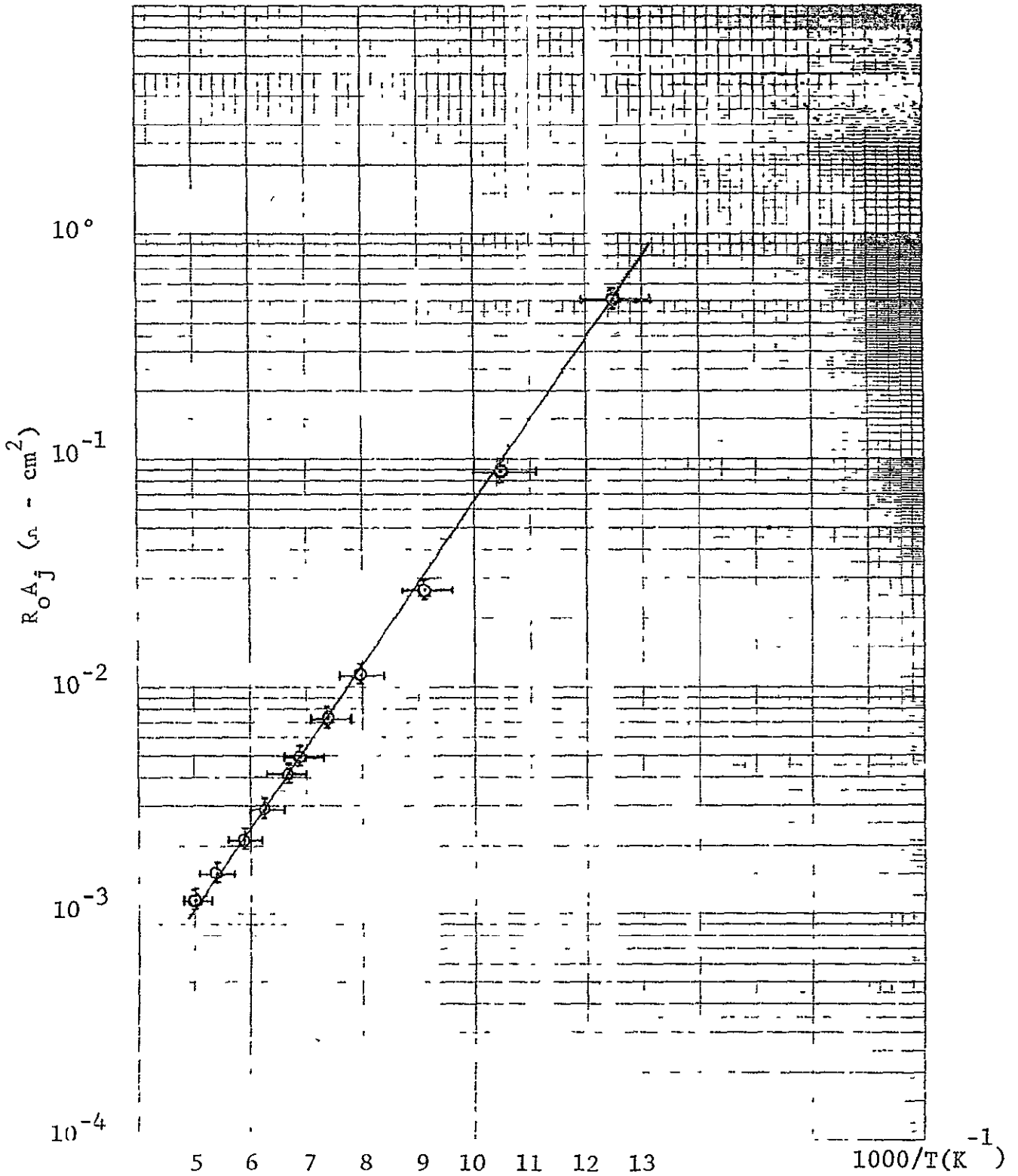

Figure 13: R_oA vs. Temperature for 30578 SO-27 P4 #2, element #2.

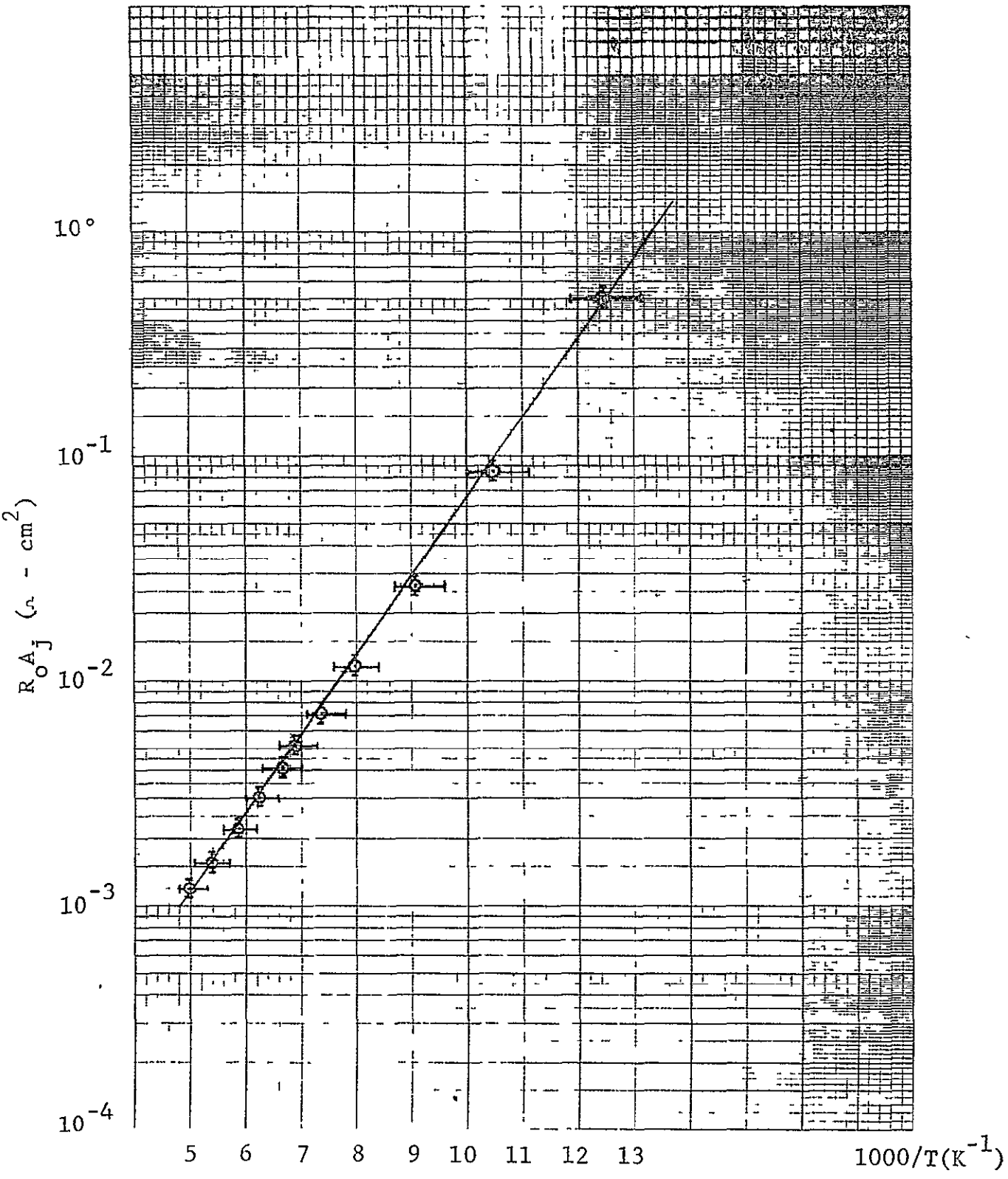

Figure 14: R_oA vs. Temperature for 30578 SO-27 P4 #2, element #3.

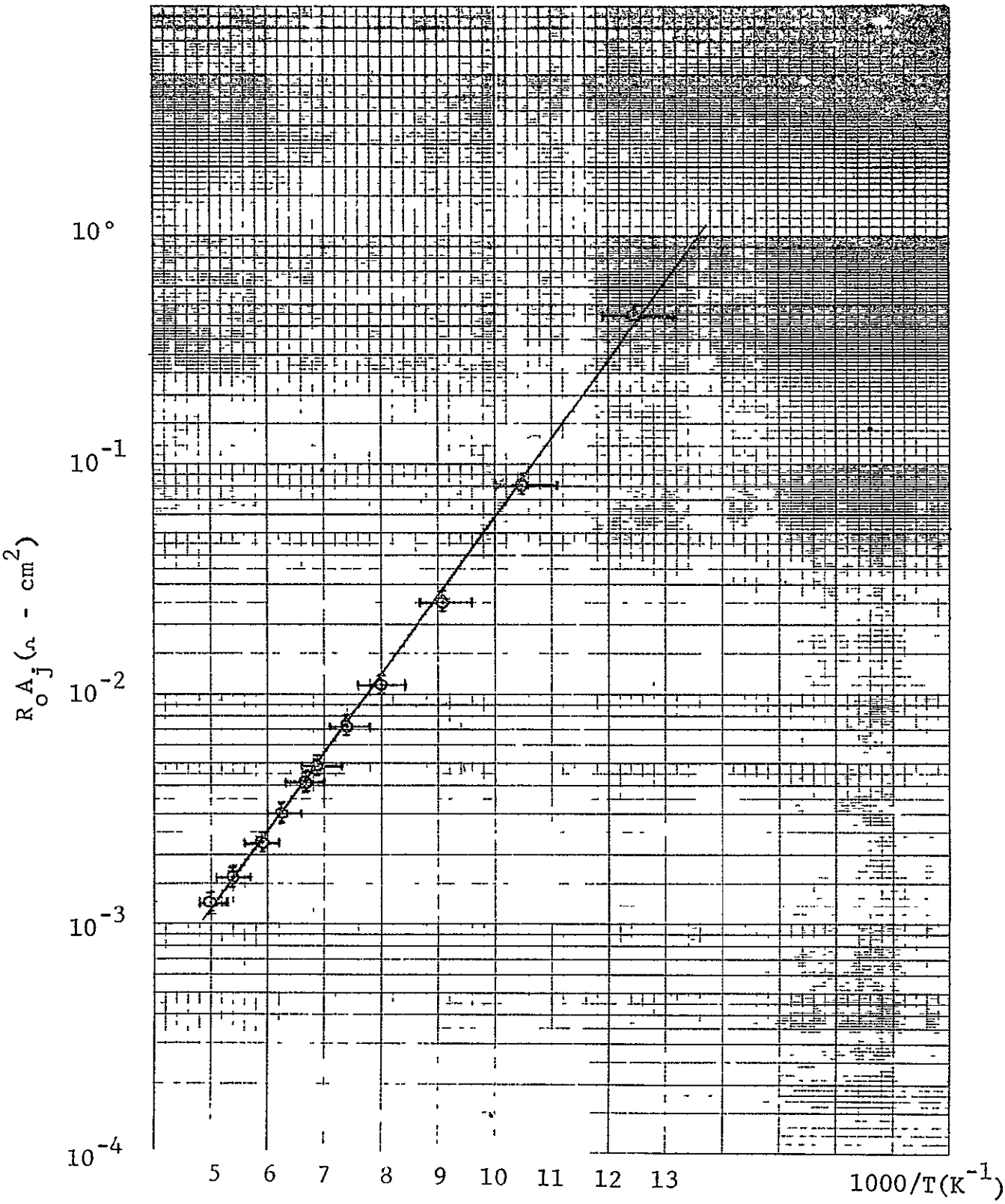

Figure 15: R_oA vs. Temperature for 30578 SO-27 P4 #2, element #4.

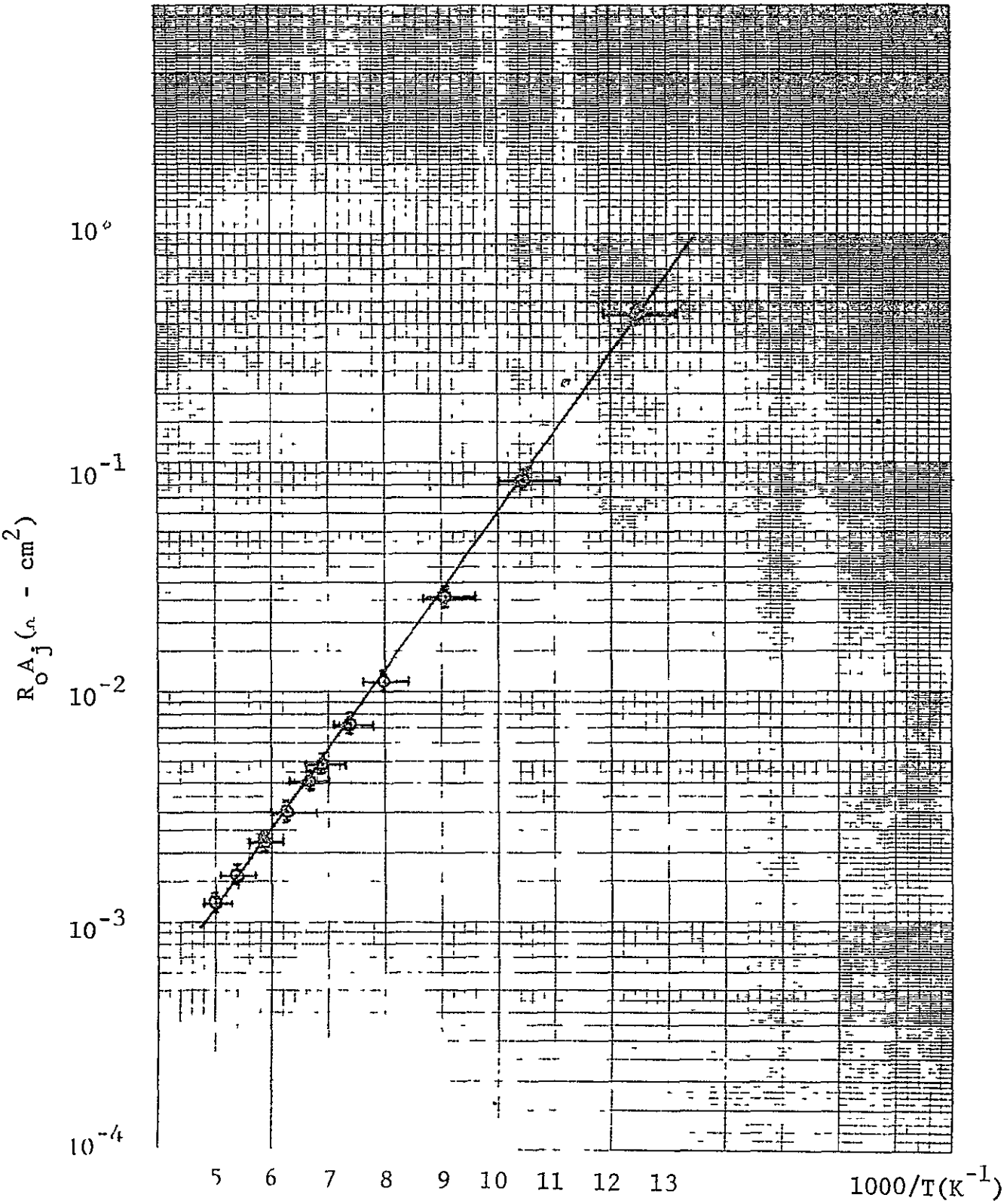

Figure 16: R_oA vs. Temperature for 30578 SO-27 P4 #2, element #5.

ORIGINAL PAGE IS
OF POOR QUALITY

4.4 Spot Scan Data

Although not for every element delivered, this data gives representative performance for all elements.

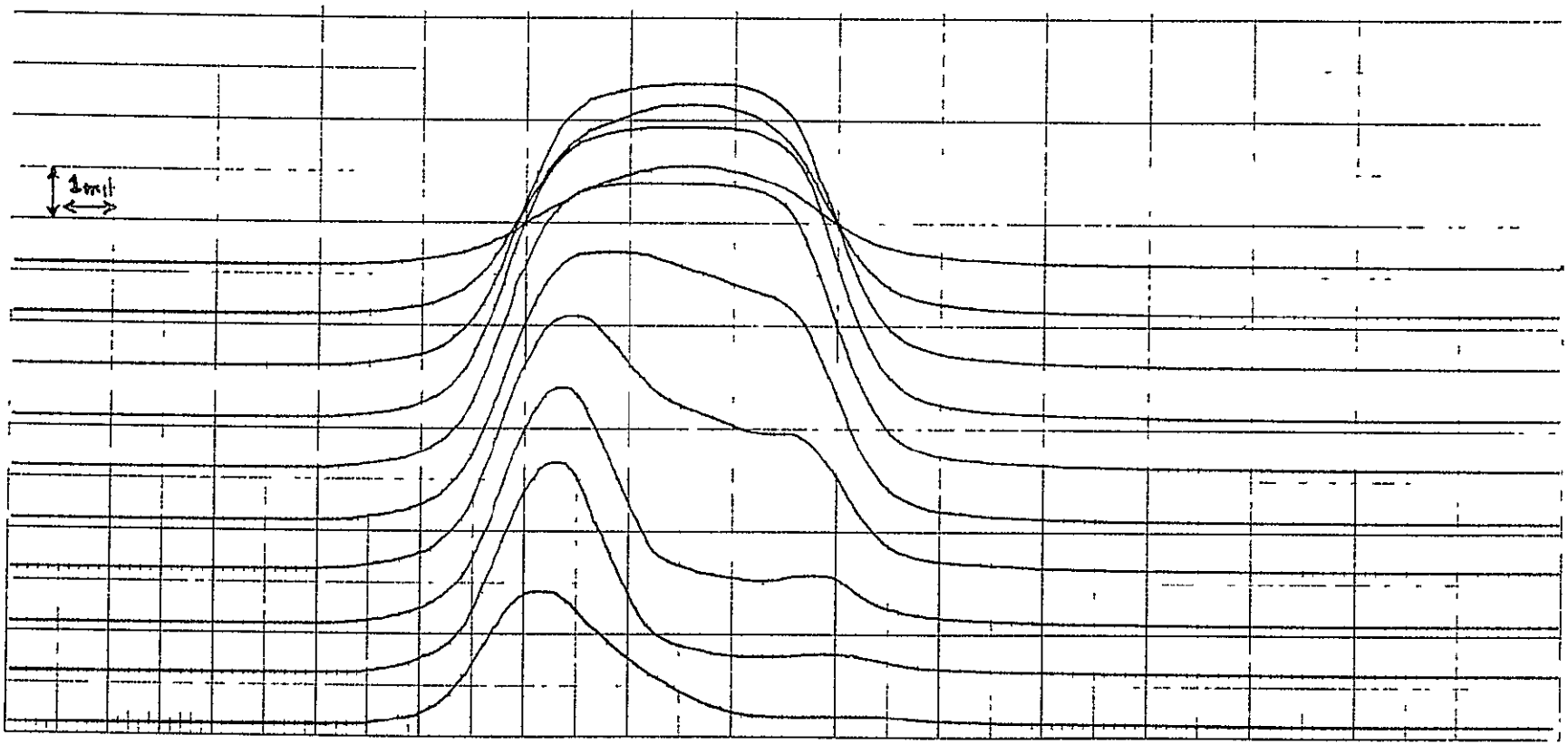

Figure 17: Spot Scan for 30578 SO-27 P4 #2, element #2a, T = 77K.

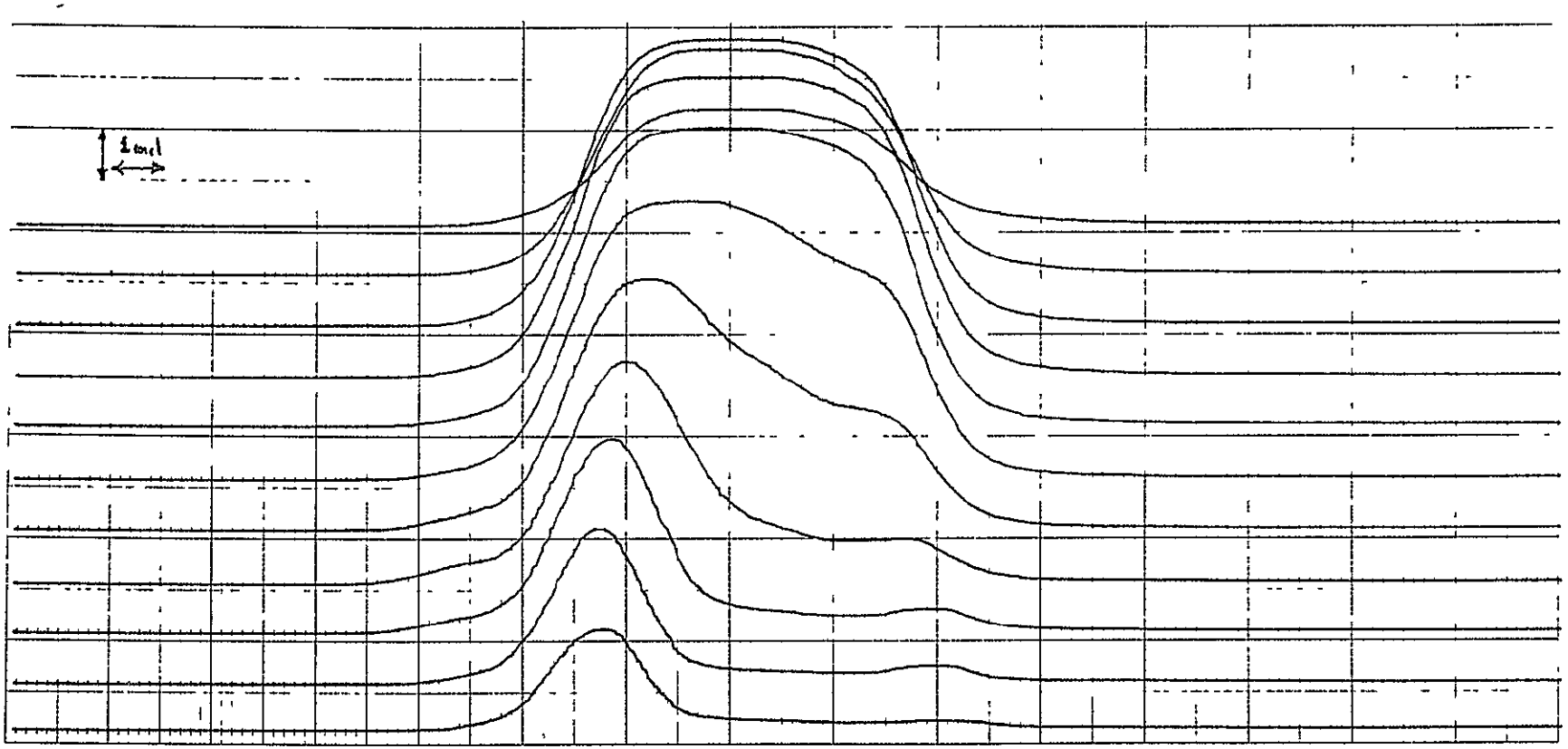

Figure 18: Spot Scan for 30578 SO-27 P4 #2, element #3, T = 77K.

ORIGINAL PAGE IS
OF POOR QUALITY

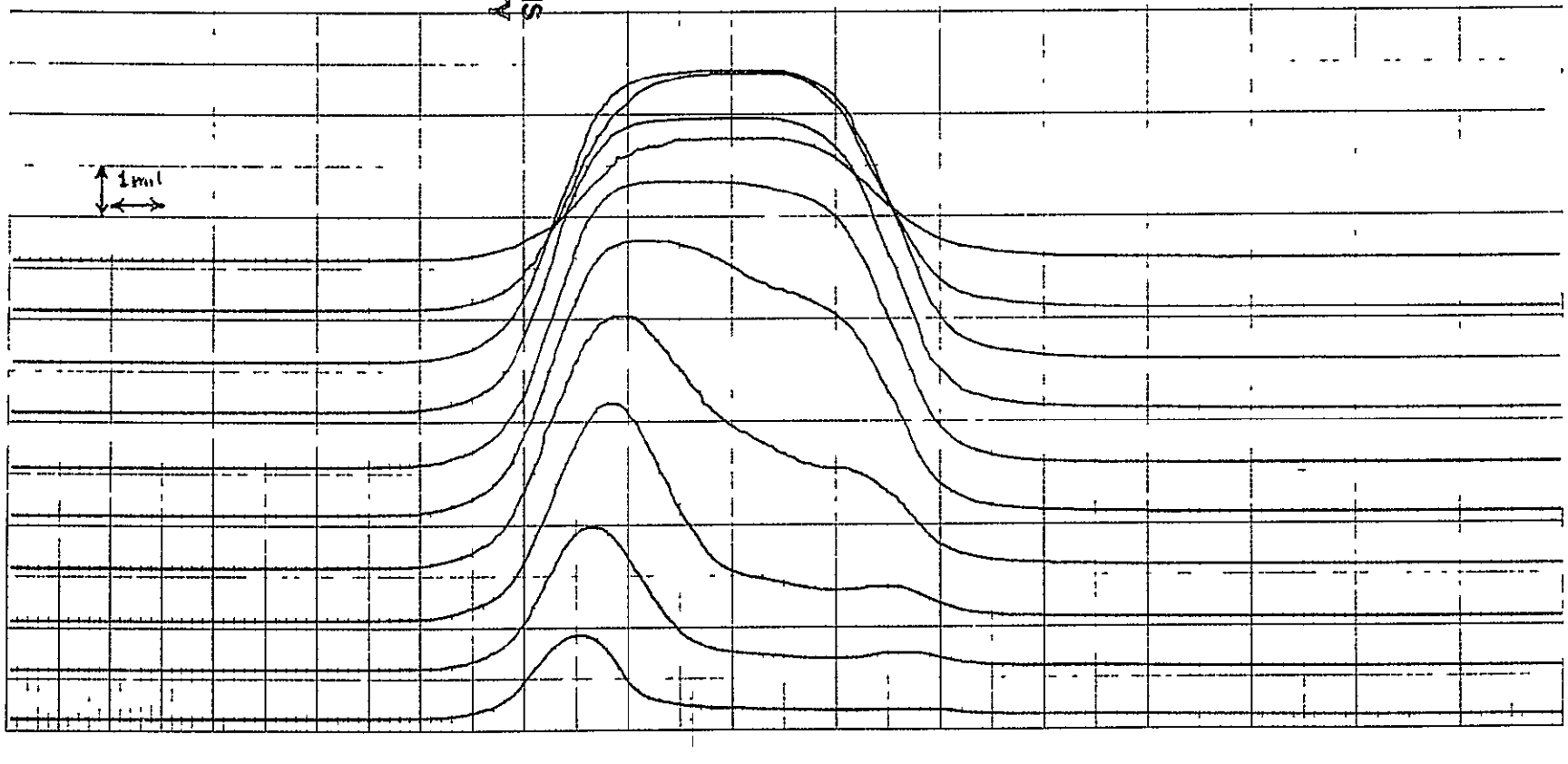

Figure 19: Spot Scan for 30578 SO-27 P4 #2, element #4a, T = 77K.

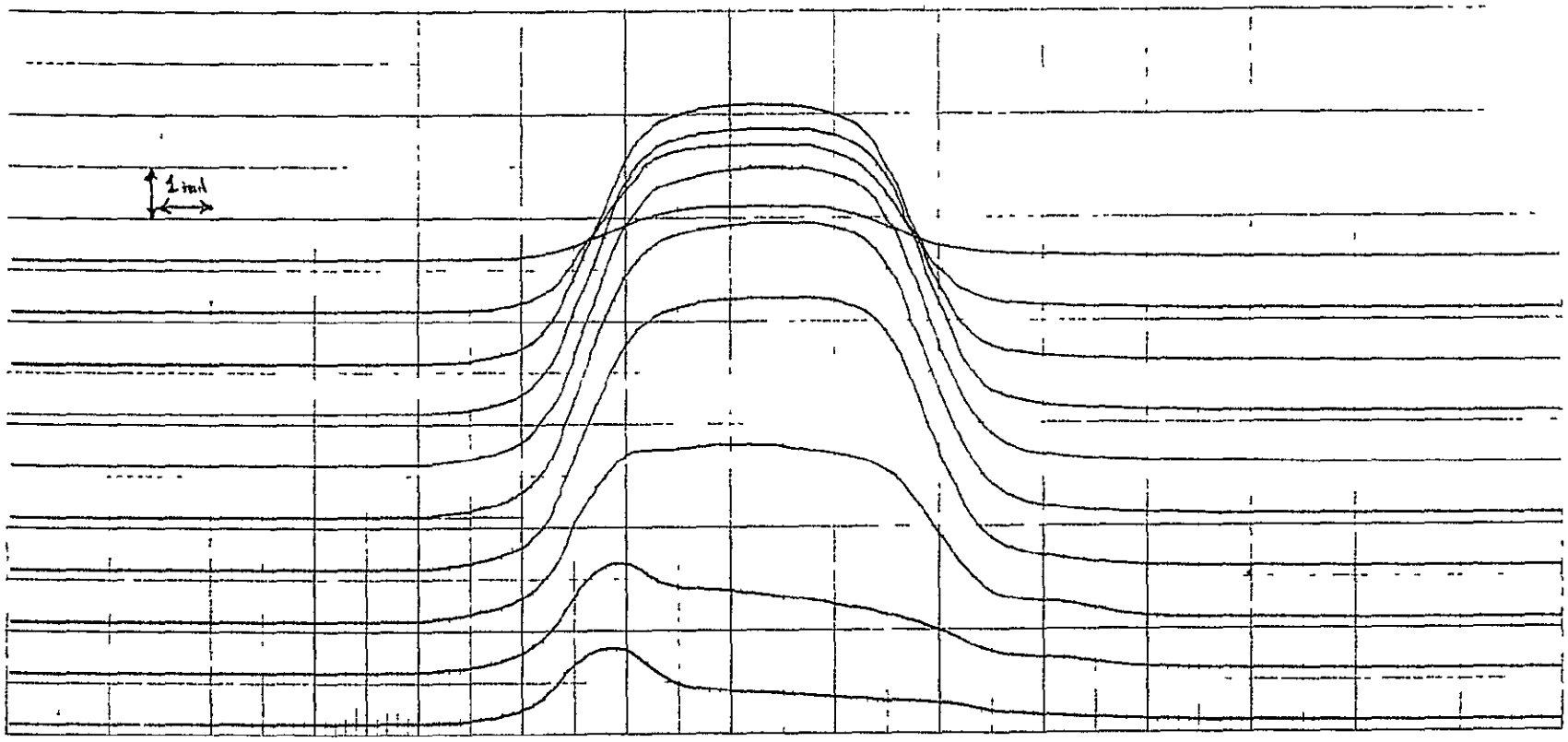

Figure 20: Spot Scan for 30578 SO-27 P4 #2, element #9, T = 77K.

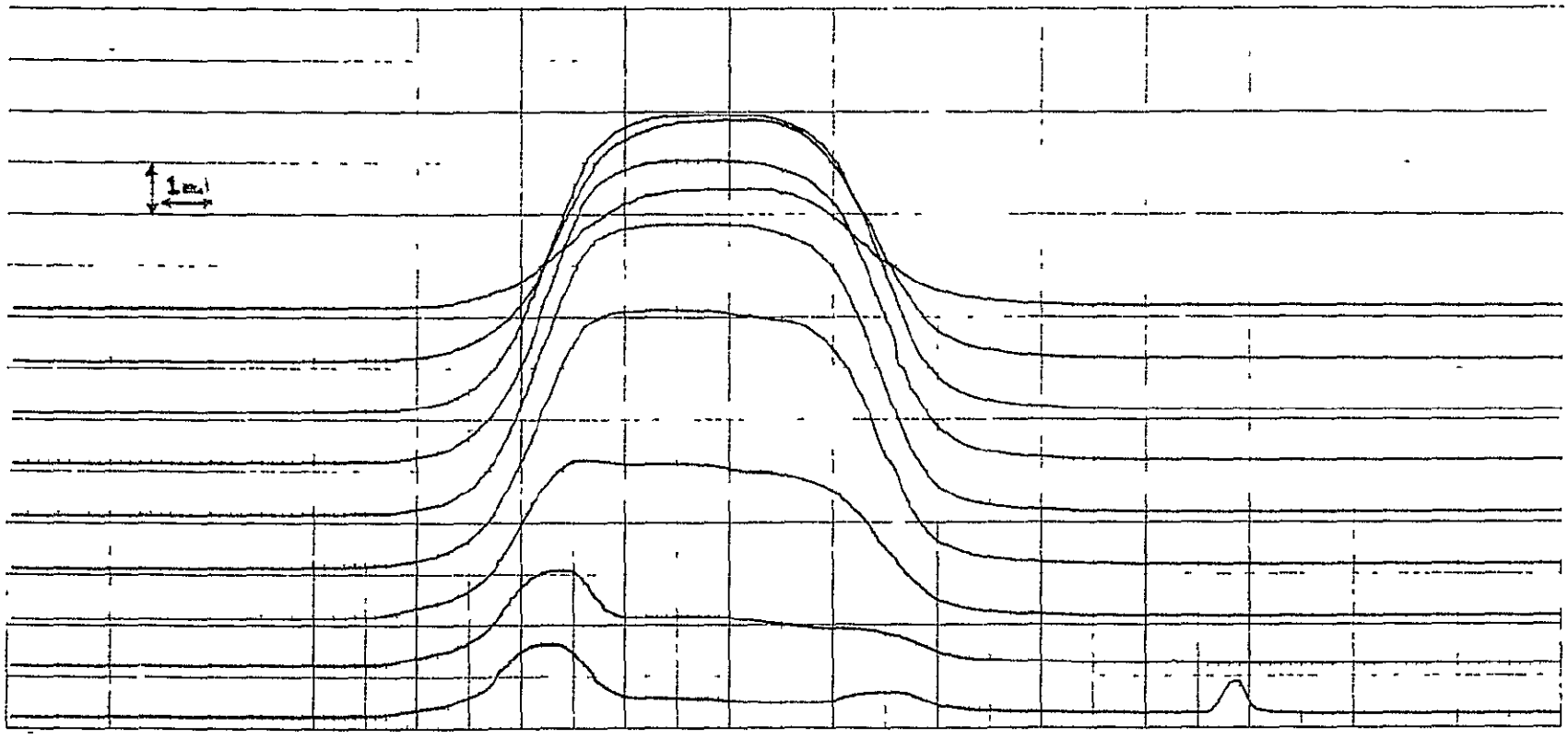

Figure 21: Spot Scan for 30578 SO-27 P4 #2, element #14, T = 77K.

5.0 APPENDIX: Testing Notes for T = 145K

In reporting the results for T = 145K, tne following procedure was used. The value of signal (145K) was taken to be equal to signal (80K). This presents no problem as the series resistance of the diode is not significant at T = 145K (see Figures 12-16). There should, therefore, be no attenuation of the signal due to a "voltage divider" effect between the junction resistance and series resistance, since the junction resistance dominates. There could be some change in quantum efficiency due to variations in the bandgap with temperature. The experimental conversion factor, accounting for the overlap between the detector spectral response and blackbody spectral output, should correct for this. The noise for the devices was calculated from the measured zero bias resistance, R_o, via the equation

$$i_n = \sqrt{4kT/R_o} \quad .$$